AN ABSTRACT OF THE THESIS OF

Robert Schickler for the degree of Master of Science in Nuclear Engineering presented on October 01, 2012.

Title: Comparison of HEU and LEU Neutron Spectra in Irradiation Facilities at the Oregon State TRIGA® Reactor

Abstract approved:

_____

Wade R. Marcum

In 2008, the Oregon State TRIGA® Reactor (OSTR) was converted from highly-enriched uranium (HEU) fuel lifetime improvement plan (FLIP) fuel to low-enriched uranium (LEU) fuel. This effort was driven and supported by the Department of Energy's (DoE's) Reduced Enrichment for Research and Test Reactors (RERTR) program. The basis behind the RERTR program's ongoing conversion effort is to reduce the nuclear proliferation risk of civilian research and test reactors. The original intent of the HEU FLIP fuel was to provide fuel to research reactors that could be utilized for many years before a necessary refueling cycle.

As a research reactor, the OSTR provides irradiation facilities for a variety of applications, such as: activation analysis, fission-track dating, commercial isotope production, neutron radiography, prompt gamma characterization, and many others. In order to accurately perform these research functions, several studies have been conducted on the HEU FLIP fuel core to characterize the neutron spectra in various experimental facilities of the OSTR. As useful as these analyses were, they are no longer valid due to the change in fuel composition and the resulting alteration of core performance characteristics. The purpose of this study is to characterize the neutron spectra in various experimental facilities within the new LEU core so as to provide data that is representative of the OSTR's current state.

Comparison of HEU and LEU Neutron Spectra in Irradiation Facilities at the Oregon State TRIGA® Reactor

by

Robert Schickler

A THESIS

submitted to

Oregon State University

in partial fulfillment of
the requirements for the
degree of

Master of Science

Presented October 01, 2012
Commencement June 2013

Master of Science thesis of Robert Schickler presented on October 01, 2012.

APPROVED:

_____

Major Professor, representing Nuclear Engineering

_____

Head of the Department of Nuclear Engineering and Radiation Health Physics

_____

Dean of the Graduate School

I understand that my thesis will become part of the permanent collection of Oregon State University libraries. My signature below authorizes release of my thesis to any reader upon request.

_____

Robert Schickler, Author

ACKNOWLEDGEMENTS

There are so many people I would like to thank for the completion of this project. To begin, I would like to thank Dr. Wade Marcum for being an excellent advisor on this project. His tenacity and boundless energy kept me on target throughout this study. His extremely high standards enabled me to produce the thesis you are now reading.

I would like to thank everyone involved with guiding me through my MCNP studies. Thanks to Dr. Todd Palmer, who first taught me how to use MCNP. Thanks to Madicken Munk, who helped me work out some kinks in my input decks. Thanks to Chris Thompson, who helped me work through various network issues to get the program to run. And of course, thanks to Kanokrat Tiyapun for writing the initial OSTR MCNP deck in 1997. It was quite the undertaking and I am truly in awe of your work.

I would like to thank everyone involved with my experimental irradiations. Thanks to Dr. Scott Menn and Jim Darrough for assisting me with the multitude of in-core irradiations and I apologize for the radiation dose! Thanks to my fellow operations staff (Gary Wachs, Todd Keller, Steve Smith) for assisting me with the experiments and operating the reactor for me while I analyzed all of the flux foils. Thanks to Dr. Leah Minc for counting my central thimble wire irradiations (next time I will be sure to give you more than 24 hours' notice!).

I would especially like to thank Dr. Larry Greenwood of PNNL for his assistance with the STAY'SL program. His expertise was invaluable and essential to the completion of my study.

I would also like to thank Eric Ashbaker for laying the groundwork on the initial OSTR characterization.

I would like to thank my committee (Dr. Kenneth Krane, Dr. William Warnes, Dr. Andrew Klein and Dr. Wade Marcum) for their help.

And lastly I would like to thank my wife Lizz for being supportive of this very stressful endeavor. I could not have finished this without you.

TABLE OF CONTENTS

TABLE OF CONTENTS (continued)

TABLE OF CONTENTS (continued)

LIST OF FIGURES

LIST OF FIGURES (continued)

LIST OF TABLES

Comparison of HEU and LEU Neutron Spectra in Irradiation Facilities at the Oregon State TRIGA® Reactor

1. INTRODUCTION

In 2008, the Oregon State TRIGA® Reactor (OSTR) was converted from highly-enriched uranium (HEU) fuel lifetime improvement plan (FLIP) fuel to low-enriched uranium (LEU) fuel [1]. This effort was driven and supported by the Department of Energy's (DoE's) Reduced Enrichment for Research and Test Reactors (RERTR) program. The basis behind the RERTR program's ongoing conversion effort is to reduce the nuclear proliferation risk of civilian research and test reactors [2]. This reduction in risk is being addressed by decreasing the enrichment of uranium-235 (U-235) within the fuel matrix. The OSTR's HEU FLIP fuel contained approximately 8.5 weight percent (wt-%) of uranium enriched to 70% U-235, whereas the current LEU fuel that occupies the OSTR core contains approximately 30 wt-% of uranium enriched to approximately 19.75% U-235. The original intent of the HEU FLIP fuel was to provide fuel to research reactors that could be utilized for many years before refueling would be necessary. The weight percentage of uranium in the new LEU fuel was increased to compensate for the reduction in enrichment, thus the actual amount of U-235 in the LEU fuel is approximately the same as the HEU FLIP fuel, however the enrichment is far lower.

1.1 Purpose

As a research reactor, the OSTR provides irradiation facilities for a variety of applications, such as: activation analysis, fission-track dating, commercial isotope production, neutron radiography, prompt gamma characterization, and many others. In order to accurately perform these research functions, several studies have been conducted on the HEU FLIP fuel core to characterize the neutron spectra in various experimental facilities of the OSTR [3,4]. As useful as these analyses were, they are no longer valid due to the change in fuel type and the resulting alteration of core performance characteristics. The purpose of this study is to characterize the neutron spectra in various experimental facilities within the new LEU core so as to provide data that is representative of the OSTR's current state.

1.2 Objectives

The objectives of this study are to characterize the neutron spectra for the current LEU core in the following experimental facilities: (a) the Rotating Rack, more commonly referred to as the 'Lazy Susan' (LS), (2) the in-core irradiation tube (ICIT), (3) the cadmium-lined ICIT (CLICIT), (4) the G-ring ICIT (GRICIT), (5) the pneumatic transfer facility (Rabbit), and (6) the thermal column (TC). In addition to these facilities, the central thimble will also be examined to determine thermal and epithermal axial flux distributions using bare and cadmium-covered aluminum-gold wires. Once each facility's neutron spectrum has been identified, a quantitative comparison between the current LEU core and the previous HEU FLIP core spectra will be made, along with a discussion including their respective differences. This study will proceed with the following tasks:

- Compare the new LEU core Monte Carlo N-particle (MCNP) model to the previous HEU FLIP core MCNP model. There are two pre-existing MCNP models of the previous HEU FLIP core (one written in 2005 for the initial characterization, and one written in 2007 for the core conversion). After verifying interchangeability of the two HEU FLIP models, the 2007 HEU FLIP model will be repurposed for the LEU core and then compared to the 2005 model.

- Experimental data will be taken in each of the following facilities: the LS, the ICIT, the CLICIT, the Rabbit, and the TC. In addition to these facilities, the GRICIT will be analyzed (this facility did not exist during the previous analyses). The central thimble will also be analyzed but only with one material (aluminum-gold wire).

- Use the MCNP5 code to model the neutron interactions in the LEU core, and use the STAY'SL code along with the experimental data collected to best-fit the neutron spectra. Compare the adjusted LEU spectra with the adjusted HEU FLIP spectra.

In summary, this work will re-characterize the neutron spectra in the aforementioned experimental facilities of the OSTR using theoretical methods (via MCNP) and provide corrected neutron spectra through use of the STAY'SL code and experimental data collection.

1.3 Document Overview

This document is organized as follows:

Chapter 1: **Introduction –** Introduction and motivation of the topic under discussion along with a general logic to the study methodology.

Chapter 2: **Literature Review –** A review of available literature on the subject and its relevance to the study.

Chapter 3: **Theory –** An explanation of the theories behind neutron spectra characterization.

Chapter 4: **Reactor Description –** A description of the OSTR and its irradiation facilities.

Chapter 5: **Methods and Materials –** A description of the methods used to characterize the OSTR neutron spectra.

Chapter 6: **Results and Discussion –** A discussion of the results obtained from the study, with a comparison between the current LEU core and the previous HEU core.

Chapter 7: **Conclusions –** Concluding remarks about this study and future recommendations for improvement.

This document concludes with a list of referenced works, nomenclature and symbols, and appendices containing additional details.

2. LITERATURE REVIEW

This chapter provides a comprehensive survey of existing, publicly available literature with regard to neutron spectra characterization, use of MCNP, foil activation techniques, and neutron spectral response due to core conversions from HEU to LEU fuel.

2.1 MCNP and the OSTR

In 1997, a MCNP deck was written to characterize the epithermal flux of the neutron beam entering the Neutron Radiography Facility (NRF) produced by the OSTR core [3]. The MCNP model, or 'deck', was a very detailed representation of the reactor and its outlying facilities. This version of the OSTR deck solely focused on flux levels, tabulated through 'tallies' within MCNP, in the NRF in order to characterize the neutron beam in relation to boron neutron capture therapy (BNCT). Tallies are MCNP cards that tabulate an item of interest (such as particles or energy) entering/depositing in a specific region of interest (a surface, cell or point detector). This '1997' deck utilized MCNP's F4 tally feature which averages the flux over a given cell; this feature is useful when one is interested in tabulating the amount of flux a body of matter will absorb in a given region of the modeled region (in this case, flux in the NRF).

In 2005, the 1997 deck was modified so as to provide the capacity for neutron spectra characterization; this model was the first full field computational attempt at quantifying neutron spectra in the OSTR irradiation facilities [4]. The results of the 2005 deck and the neutron spectra characterization efforts were presented by E. Ashbaker [4]. One of the significant advances made within the 2005 deck was through reworking of the 1997 deck in order to determine flux tallies in the B1 position (ICIT/CLICIT), the Lazy Susan, the Rabbit, and the TC.

The 2005 model utilized several variance reduction techniques such as energy splitting and weight cutoffs, but was unable to produce low-error theoretical data in the thermal column. Few, if any, epithermal neutrons were tallied by the 2005 MCNP model in the thermal column, leading to poor statistical significance and high error in the few energy bins that received neutrons (Figure 2–1).

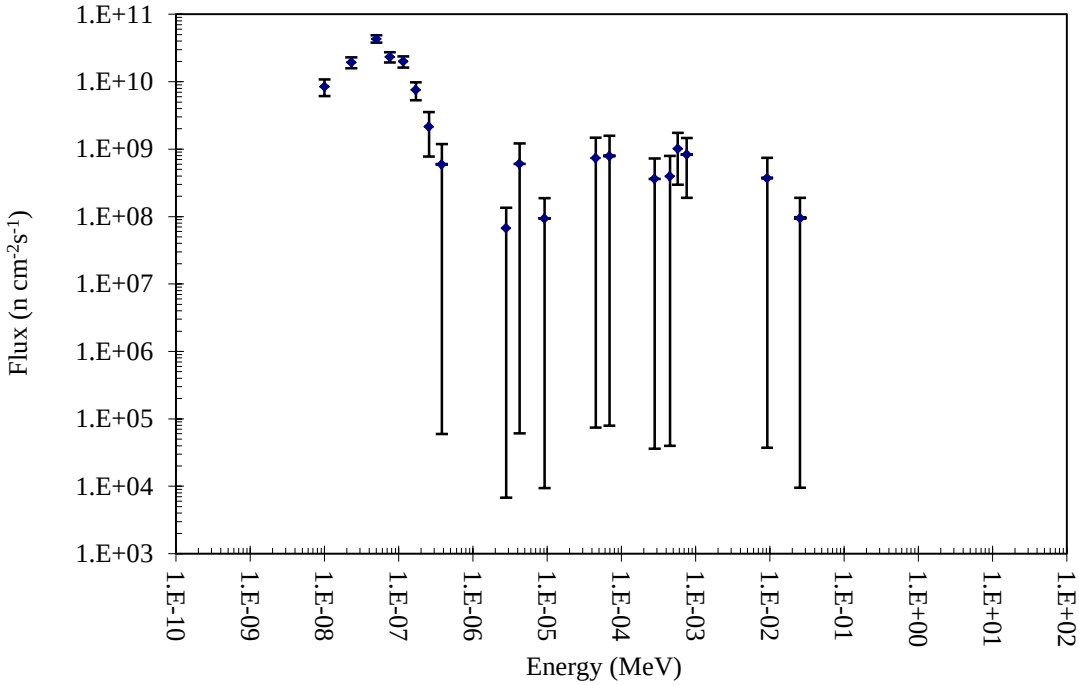

Figure 2–1: 2005 MCNP modeled flux distribution in thermal column

In 2007, the 2005 MCNP deck previously examined by Ashbaker was updated and modified in support of the core conversion from HEU to LEU [1]. Numerous cases within the updated 2007 deck were considered during the HEU to LEU conversion study in order to account for different core configurations (ICIT, CLICIT and NORMAL cores) and periods over the core life (i.e. beginning of life (BOL), middle of life (MOL), end of life (EOL)).

Table 2-1 summarizes the significant modifications and further advancements of the 2007 model relative to the 2005 model, focusing on the BOL ICIT core configuration.

Table 2-1: Differences between 2005 and 2007 OSTR MCNP decks

Core Components	2005 Model	2007 Model
Cell Material Composition Outside Core Region	Some cells outside of reactor modeled as voids	Modeled as water
Central Thimble	Modeled as pure aluminum	Modeled as a water/aluminum mixture
Fuel Composition	All fuel modeled with one material card	Fuel cell cards generated by a spreadsheet
Neutron Source	Model uses graphite reflector in place of neutron source	Model uses aluminum air-filled tube in place of neutron source
Fuel Elements	One radial zone in each fuel element	Three radial zones in each fuel element (more resolved)
Control Rod	Control rod radii equal to fuel rod radius	Control rod radii smaller than fuel rod radius (more accurate)
GRICIT	G14 is modeled as a water hole	G14 is modeled with the GRICIT in place
Thermal Column	Modeled at 60.96 cm above center of model	Modeled at 80 cm above center of model

The variations in model design (Table 2-1) along with other contributing factors such as MCNP version and cross sectional libraries utilized, yield a relatively large difference in the calculated critical rod heights between the two models; these corresponding critical rod heights (obtained from the respective models' MCNP output files) are presented in Table 2-2.

Table 2-2: Differences in critical rod heights (percent withdrawn from core)

Control Rod	2005 MCNP Model	2007 MCNP Model
Transient	48.40	39.76
Safety	51.20	31.50
Shim	50.80	41.10
Regulating	54.20	41.44

As shown in Table 2-2 the 2007 model yields a core with a qualitatively smaller shutdown margin, which inductively leads to a larger core excess reactivity.

Due to the relatively thick diffuse region and large distance from the core, the thermal column has proven to be one of the most difficult experimental facilities to numerically

characterize in TRIGA® reactors. There have, however, been improved techniques when modeling the thermal column within MCNP by other organizations that utilize TRIGA® Reactors. In 2010, Rustam Khan modeled the TRIGA® Mark II reactor at the Vienna University of Technology using the FMESH card, within MCNP [5]. The FMESH card allows the user to define a mesh tally superimposed over the problem geometry. In this case, the mesh tally was applied to an 11-by-11 matrix. The maximum flux was determined to be 8.31E7 neutrons per cm^2 and the minimum flux was determined to be 2.07E7 neutrons per cm^2. The ratio of calculated MCNP flux to experimental flux was measured and the maximum ratio value was 1.926. Only one experimental point was found to yield a smaller flux than that output by the MCNP model, indicating that the MCNP model, in general, over-estimated fluxes for the study. Furthermore, the FMESH card enabled a larger abundance of neutrons to occupy the tally region than would have otherwise been tabulated, resulting in a more statistically sound solution [5].

The 1997 OSTR MCNP model utilized DXTRAN particles to guide neutrons down the epithermal beam port in order to more accurately calculate flux in the OSTR NRF. This MCNP feature may be employed as an alternative method to improve the statistical results within the model regions that are located relatively far away from any neutron source. DXTRAN particles are another form of variance reduction. They “force” neutrons to move to a region of interest [3].

2.2 Activation Foil Selection and Subsequent Spectrum Unfolding

In order to computationally characterize reactor kinetics, a quantitative method for identifying particles’ probability of interacting with matter (denoted as ‘cross section’) must be organized and utilized. This organizational system is most often referred to as a cross sectional library. The Lawrence Livermore Evaluated Nuclear Data Library (ENDL) was first developed in 1958. This cross sectional library started out as a series of memos containing tabulations of cross sections and angular distributions used in neutronics calculations [6]. As more neutronic analyses were undertaken, a need arose to make this data available in a computerized format. The ENDL was formed and data was initially made available on punch cards; eventually this information was transferred to

magnetic tape. Presently there are many different nuclear data libraries to choose from, the most prominent being the Evaluated Nuclear Data File ENDF/B-VII [7].

The ENDF data was particularly useful to the research community in many areas including the field of spectra characterization. In 1965, William N. McElroy wrote a generalized foil activation method for determining neutron flux-spectra [8]. His dissertation utilized 32 different foil detectors, with cross sections determined from various data libraries available at the time. The activation data produced from irradiation were used in conjunction with a variety of methods (iterative methods, non-iterative methods, and single iterative method) to determine neutron spectra in the IITRI Research Reactor. One of the primary conclusions of McElroy's study centered on the importance of selecting the most appropriate activation foil material and having a high cross section (or probability of interaction) for the spectral energy region of interest as this minimizes errors during the spectrum unfolding process. If there is a large amount of uncertainty in the foil's cross section, it will yield a large chi-squared value, which in turn demonstrates a poor spectral adjustment result. Chi-squared is further explained in Chapter 3.

In October 1977, a technical committee organized by the International Atomic Energy Agency (IAEA) met to discuss the current status of neutron spectrum unfolding [9]. The process of spectrum unfolding is described in detail in Chapter 3. Various topics were discussed during the technical committee meeting, such as spectrum unfolding computer codes, cross section libraries, shielding effects of foil covers, and many other related topics. One presentation in particular [10] reviewed all of the publically available unfolding methods used for reactor dosimetry in the United States up to that point. This presentation recommended that an ASTM standard be developed in order to yield a more consistent and congruent set of benchmark problems and codes. The unfolding codes were divided up into different classifications: category, class, and type. The different categories were parametric representation, derivative, quadrature and Monte Carlo. The various classes of codes included linear estimation, iterative adjustment and mathematical programming. Lastly, each type of code was broken down into statistical, non-statistical,

correction matrix iteration, semi-empirical, linear programming and quadratic programming subcategories.

ASTM standard E944 was written to compare all of the various unfolding programs currently available to the research community [11]. Thirteen different codes were compared by examining their respective solution methods. All of the solution methods were statistical except for the SAND-II program [12], which is semi-iterative. All of the codes are presently available through the Radiation Safety Information Computational Center (RSICC) [13] with the exception of the Neutron Metrology File-90 (NMF-90) code [14], which may be acquired through the IAEA Nuclear Data Services. The NMF-90 code is used outside of the United States in conjunction with the STAY'NL program (a modified version of the STAY'SL unfolding code) for spectral adjustments [15].

The STAY'SL code was initially developed at the Oak Ridge National Laboratory by F.G. Perey [16]. This code solves the spectrum unfolding problem by the method of least squares in order to minimize the chi-squared. The 2005 OSTR study, which characterized the spectrum of the OSTR, utilized the STAY'SL unfolding code. This code divided the full energy spectrum considered within the model (from 1E-10 MeV up to 20 MeV) into 100 energy bins. The STAY'SL code allows up to 20 experimental activation reactions to be included within a given input file, enabling the ability to adjust the computationally produced spectra to most suitably reflect the physical system. In addition to the spectrum unfolding calculation for ideal geometry, STAY'SL accounts for self-shielding in the experimental activation foils themselves, as well as the cadmium covers used to shield out thermal neutron interactions around the experimental activation foils.

2.3 HEU to LEU Core Conversion

Since the conception of the nuclear reactor, countless cores (of both research and power reactors) have been redesigned, reconfigured, and additionally converted. One most recently stressed method for conversion of research reactors is the removal of HEU fuel and replacement with a suitably designed substitute LEU fuel. One example of this HEU to LEU conversion is the Pakistan Research Reactor-1 (PARR-1), which was converted in 1995. As a part of the PARR-1's conversion, a study was performed to characterize the

change in flux and spectrum between the HEU and LEU core in the reactor's thermal column irradiation facility. This was accomplished by irradiating seven different activation foils in the thermal column in both core configurations. The activation data and neutronic calculations were unfolded using the SANDBP code [17]; two sets of spectra were produced. The thermal flux appeared to reduce in the LEU core, whereas the epithermal flux seemed to increase slightly. The study attributed this observation to the change in water channel gap between the HEU and LEU fuel plates (the LEU core was speculated to be slightly under moderated) [18].

Another core conversion study was performed at the Pakistan Institute of Engineering and Applied Sciences (PIEAS) to determine various LEU fuel alternatives for the Pakistan Research Reactor-2 (PARR-2). Three types of LEU fuel (UO_2 with zircaloy cladding, UO_2 with aluminum cladding, and U_9Mo fuel) were examined using the WIMS-D4 and CITATION computer codes. It was determined that all three fuels would exhibit similar characteristics as the standard HEU fuel, however the lower energy spectra appeared to be slightly higher with LEU fuel than the HEU. The spectrum was found to be the hardest in the U_9Mo fuel of the three LEU fuel alternatives considered. This was attributed to relatively larger abundance of absorption interactions taking place within the molybdenum matrix, thereby limiting the U_9Mo fuel's usefulness in the research reactor community, as it would adversely affect irradiations that are sensitive to thermal flux [19].

A study was performed at The University of Missouri Research Reactor (MURR) using MCNP to predict key parameters in the case of fuel conversion [20]. Two fuel configurations of HEU and LEU were tabulated and a normalized flux per unit lethargy was determined for both configurations in order to theoretically demonstrate that a change in fuel type would allow researchers to obtain acceptably similar flux levels in the reactor's irradiation facilities after conversion to LEU fuel. Both configurations had a similar spectral shape; however, the LEU core configuration was found to have a slightly lower flux per unit lethargy in the thermal and epithermal regions. Due to the similarity in

spectral shape and flux magnitudes between both fuel compositions, it was determined that conversion to an LEU fuel would be feasible based on reactor performance criteria.

3. THEORY

This chapter describes the theory utilized within this study to perform the spectral analysis of the OSTR irradiation facilities. The neutron energy spectra will be discussed, as well as the theory behind MCNP, neutron activation analysis (NAA), and STAY'SL.

3.1 Neutron Energy Spectra

As neutrons are born from fission, they begin their "life", generally at a relatively high energy. A neutron's birth is followed by a series of scattering interactions, until it either leaks from the system or is absorbed by a target nucleus through capture or fission. The end of a neutron's life is often referred to as its "death". The probability of a prescribed interaction for a given particle is referred to as the cross section. The total cross section (σ_T) refers to the probability of said particle interacting with its surrounding medium through any means. Generally, there are two broad interaction mechanisms that are referred to often in particle transport, these are scattering or absorption. The total cross section is the sum of the scattering (σ_s) and absorption (σ_a) cross section as seen in (1).

$$\sigma_{\mathrm{T}} = \sigma_{\mathrm{s}} + \sigma_{\mathrm{a}} \tag{1}$$

Both scattering and absorbing interactions may be further divided into differing reactions. Particles, often containing very high energies (or traveling at very high velocities relative to their surroundings) may undergo inelastic scattering $(\sigma_{n'})$, while lower energy (or slower traveling) particles more often undergo elastic scattering (σ_n) events summing to the total scattering cross section shown in (2).

$$\sigma_{\mathrm{s}} = \sigma_{\mathrm{n}} + \sigma_{\mathrm{n'}} \tag{2}$$

Elastic scattering conserves both momentum and kinetic energy; this interaction event may be thought of as a billiard ball collision between a neutron and a nucleus. In an inelastic scattering collision the neutron gives up some of its energy to the nucleus,

leaving it in an excited state. Thus while momentum is conserved in an inelastic collision, kinetic energy is not; the nucleus gives up its excitation energy by emitting one or more gamma rays along with the neutron [21].

Absorption interactions may be divided into fission events characterized by the fission cross section (σ_f) and capture events driven by the capture cross section (σ_γ) as seen in (3).

$$\sigma_{\mathrm{a}} = \sigma_{\mathrm{f}} + \sigma_{\gamma} \tag{3}$$

In an absorption event, the neutron is taken in by an atom, forming a compound nucleus. The resulting compound nucleus may then either undergo a fission event, where the nucleus is split into multiple fission products, or a capture event. In the event of capture, the compound nucleus will generally become unstable and undergo radioactive decay due to the additional energy acquired from the neutron, leaving the nucleus in an excited state. This is the primary reaction desired for NAA studies, as NAA examines the gamma rays that emanate from irradiated materials. For the purposes of this study, two types of capture events are examined: capture events that result in gamma decay, referred to as (n,g) reactions, and threshold events that result in the ejection of a particle and subsequent gamma decay. The threshold event reactions observed during this study were the (n,p) reaction (absorption of a neutron, rejection of a proton) and (n,a) reaction (absorption of a neutron, rejection of an alpha particle) specifically.

Neutron energy spectra are typically divided into three separate energy regions: thermal, epithermal, and fast. Neutrons are generally born in the fast energy spectrum. As they begin to interact with their surrounding medium they rapidly lose energy. The neutron may downscatter to epithermal energy level and possibly loses enough energy to reach a thermal energy level. The energy ranges separating the fast, epithermal, and thermal regions are somewhat arbitrary and not always explicitly defined, however they are often determined by reactions of interest.

3.1.1 Fast Energy Spectrum

Neutrons are born from fission at a general energy of 2 MeV with the most likely energy being 0.75 MeV [21]. When focusing on thermal fission reactors, the abundance of neutrons that exist at energies over 20 MeV is considered negligible as very few particles ever exist at this energy level and those that do exist tend to rapidly lose energy. The upper bound of the fast energy spectrum is therefore typically taken to be at 20 MeV. The fission neutron energy distribution is most commonly approximated by the Watt fission spectrum equation [22] seen in(4).

$$\chi(\mathrm{E}) = 0.453\exp(-1.036\mathrm{E})\sinh(2.29\mathrm{E})^{\frac{1}{2}} \tag{4}$$

$\chi(\mathrm{E})$ is the fractional number of neutrons within the given spectral distribution function. Figure 3–1 illustrates how fast energy neutrons are most likely to exist in the fast spectrum at approximately 0.75 MeV.

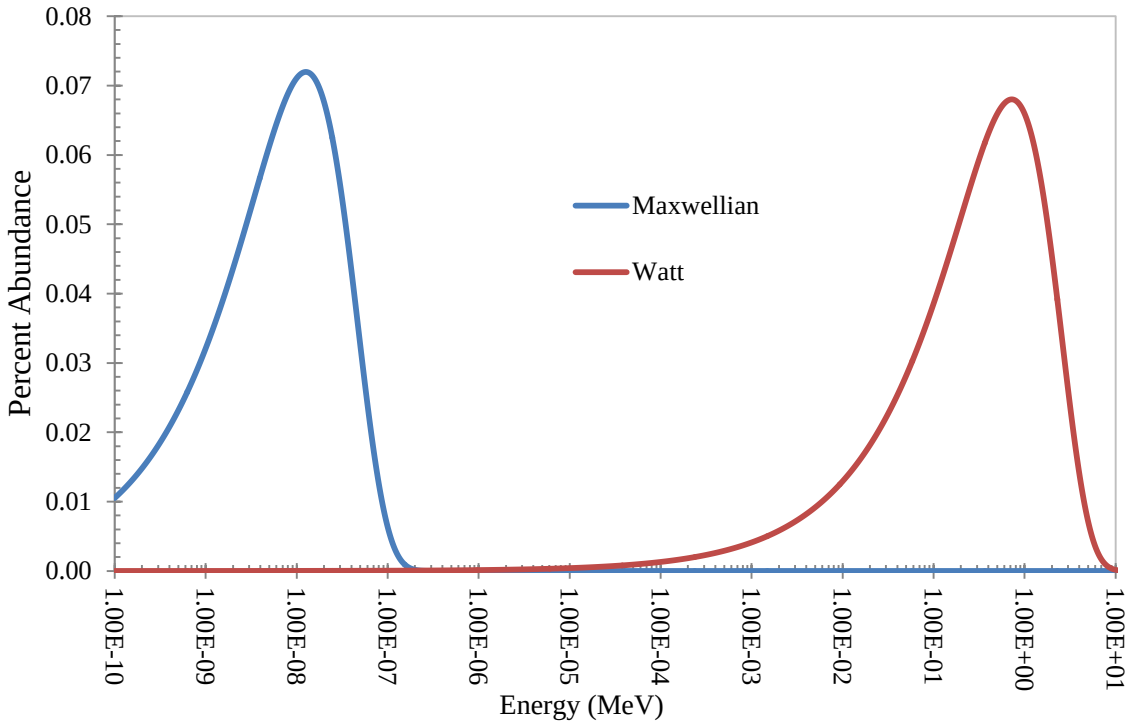

Figure 3–1: Fission and thermal neutron energy spectra

From Figure 3–1 it appears that the fast energy spectrum becomes negligible below approximately 1E-5 MeV (10 eV). In order to determine the fast energy spectra, irradiations are performed with various materials that have an affinity for threshold reactions. Threshold reactions are endothermic neutron interactions that result in the emission of a particle after a certain amount of threshold energy has been overcome [23]. The two types of threshold reactions observed during the course of this study are the (n,p) reaction and the (n,a) reaction. The threshold reactions produced from the materials used in this study take place at energies higher than 1 MeV, thus the lower bound of this study's fast energy spectrum is taken to be at 1 MeV.

As a core ages, the ^{235}U content of the fuel begins to deplete. However, the ^{238}U in the fuel begins to absorb neutrons, which converts it into ^{239}U, which then decays into the fissile ^{239}Pu. As ^{239}Pu content increases and ^{235}U content decreases, the fast spectrum tends to harden as the fission cross section of ^{239}Pu is higher than ^{235}U in the fast spectrum (Figure 3–2), which leads to higher fast flux.

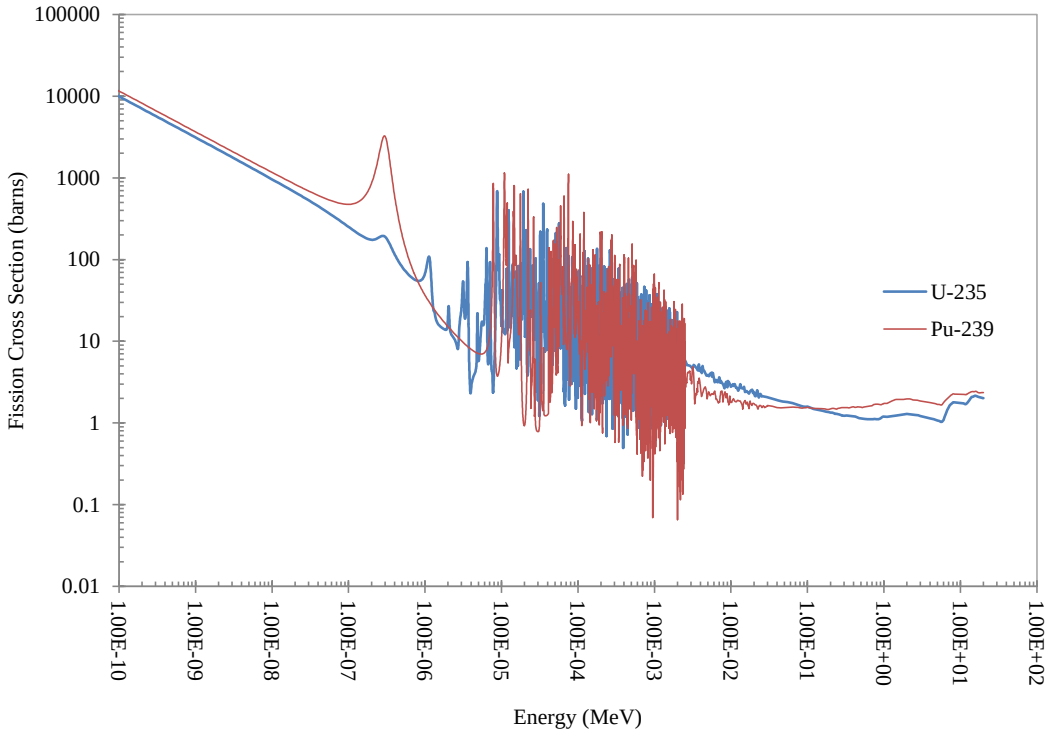

Figure 3–2: Fission cross sections of ^{235}U and ^{239}Pu [7]

3.1.2 Epithermal Energy Spectrum

After a neutron is born, it is most probable that it will interact with its surrounding medium unless its surrounding medium is a vacuum. In the case of this study a neutron's surrounding medium includes, but is not limited to, cladding, fuel, reflector, or coolant. These interactions may include absorption and/or scattering. As neutrons scatter, they lose energy until eventually losing sufficient energy to drop below the fast energy spectrum. The epithermal energy spectrum is directly adjacent to and below the fast energy spectrum. In the epithermal region, neutron absorptions may result due to resonances in the absorbing material. Different materials have different affinities for epithermal energy absorption. For instance, the epithermal cross-sections for ^{238}U and ^{167}Er, two materials that are present in the OSTR fuel and have significant epithermal effects, are shown in Figure 3–3. If neutrons exiting the fast spectrum in the OSTR encounter either of these materials, there is a strong likelihood of interaction as their cross sectional values are much larger than most other materials present in the OSTR core.

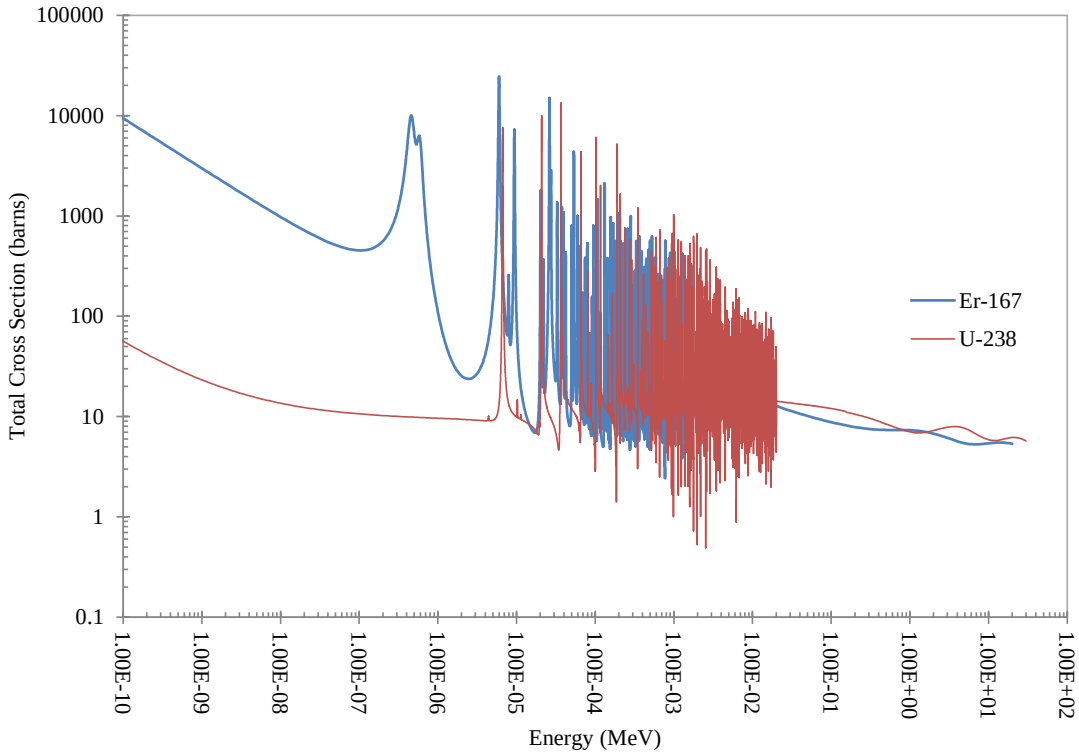

Figure 3–3: Total cross sections of U-238 and Er-167 [7]

Activation foils are used in a similar fashion within the epithermal energy region as that of the fast energy region. Select materials have strong resonance peaks which allow fluxes to be determined at certain resonance energies. This study uses cadmium to separate thermal neutrons from the epithermal/fast neutron. Cadmium has a very high absorption cross section at 0.4 eV (Figure 3–4), most commonly referred to as the cadmium cutoff.

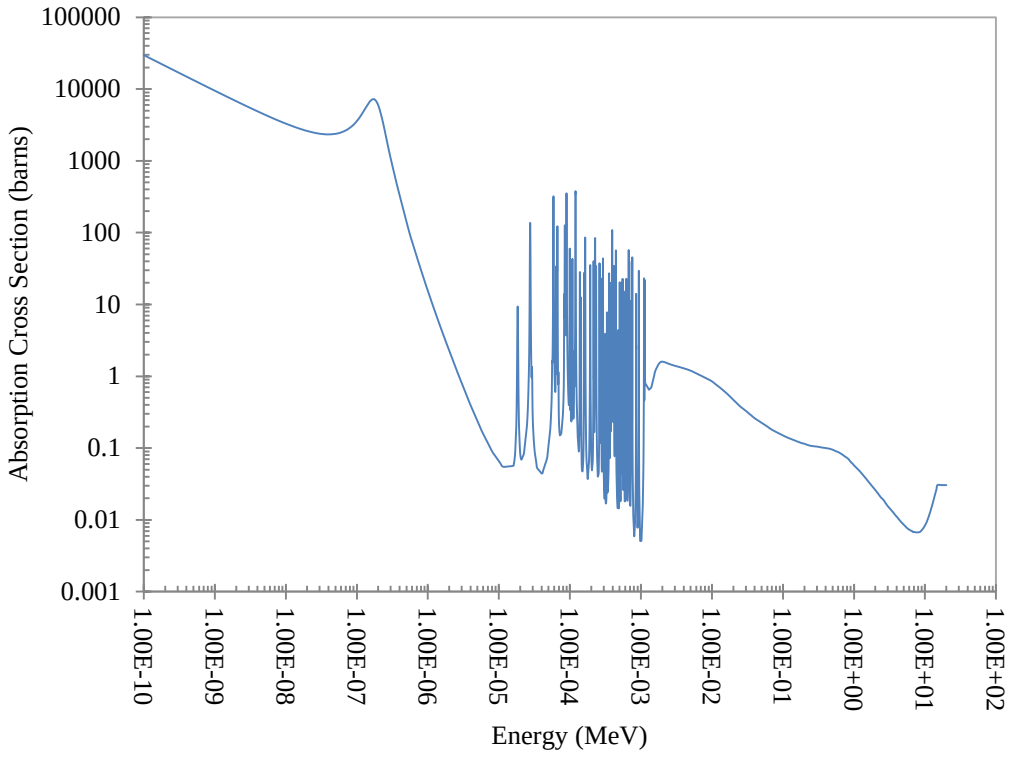

Figure 3–4: Absorption cross section for natural cadmium [7]

Since cadmium has such a high absorption cross section (roughly 10,000 barns or 1E-20 cm^2) at approximately 0.2 eV and a cross section value at 0.5 eV equal to the highest observed resonance at 100 eV, the lower bound of the epithermal region for this study is assumed to reside at 0.5 eV.

3.1.3 Thermal Energy Spectrum

All neutrons below 0.5 eV are considered herein as thermal neutrons due to the necessary continuity between the thermal and epithermal energy regions. Thermal neutrons are defined as neutrons that are in thermal equilibrium with their surroundings. In the case of the OSTR, fuel and moderator material dominate the surrounding medium within the core region. Because the OSTR operates near room temperature (approximately 20ºC) the Maxwellian distribution characterizes the dominant neutron energy to correspond at approximately 0.0253 eV [24]. The Maxwellian distribution is shown in equation (5) as

$$f(E) = \frac{2\pi\sqrt{E}\exp(-E / kT)}{(\pi kT)^{\frac{3}{2}}} \quad (5)$$

where f(E) is the fractional energy spectrum, k is the Boltzmann constant, and T is the medium temperature in units of Kelvin. Figure 3–1 displays the typical Maxwellian distribution at room temperature. As temperature increases, the spectrum hardens and the maximum value of f(E) shifts upward in energy and to the right in Figure 3–1. This effect is considered negligible in the OSTR as experimental sample temperature is not expected to increase substantially above room temperature. For example, a temperature study was performed at the OSTR and it was determined that the sample temperature in the ICIT is approximately 110ºC [25]. Figure 3–5 presents the relative difference in neutron distribution of the Maxwellian distribution at room temperature (20 ºC) and 110 ºC. Note that from Figure 3–5 the most probable energy level in which neutrons reside at 20 ºC is 1.3E-8 MeV while at 110 ºC it is 1.6E-8 MeV.

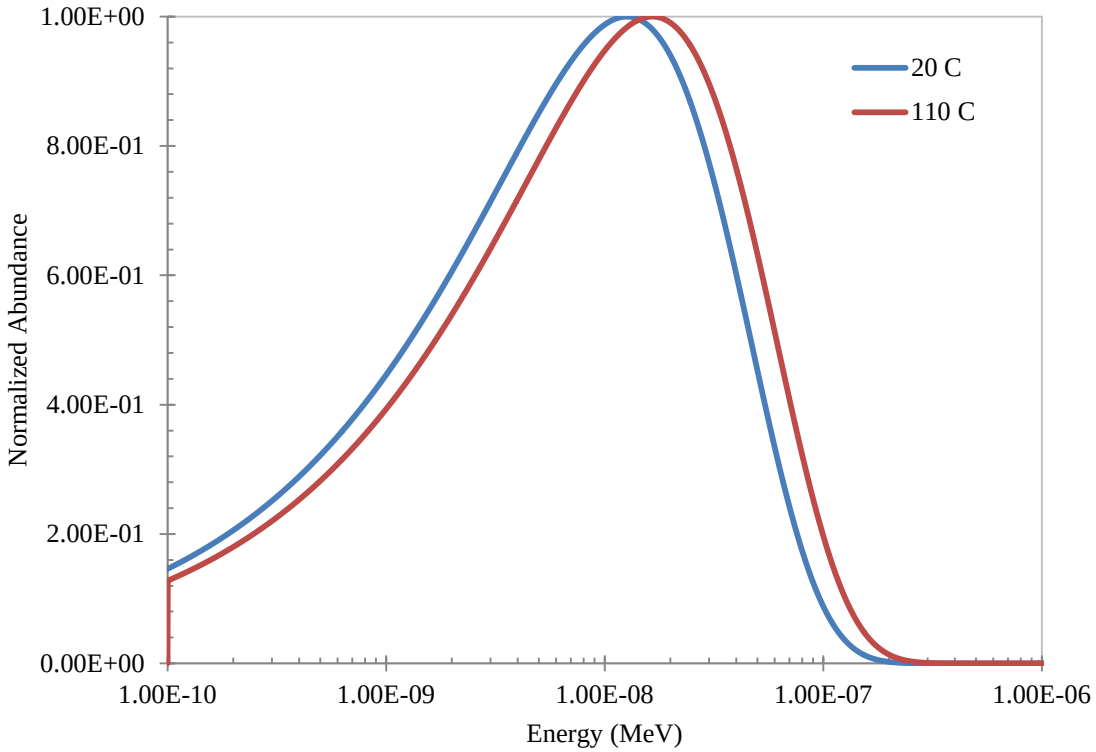

Figure 3–5: Maxwellian distribution at 20ºC and 110ºC

Thermal flux will be increased in graphite-reflected regions of the reactor due to the albedo effect [21]. As thermal neutrons escape the OSTR core periphery, some will bounce off of the graphite reflector and back into the core, increasing the thermal flux at the core periphery.

3.2 Neutronics Calculations (MCNP)

MCNP is a powerful computer tool that uses a stochastic method to determine various quantities pertaining to nuclear reactions in a prescribed region of defined material composition. In order to use MCNP, four input characteristics are required: (1) a geometric description of the modeled structures, (2) material description of said structures, (3) description of a neutron source, and (4) desired output parameters [26].

For the geometric and material description of the structures, the user must develop an input deck that defines a geometric model of the desired system (in this case, a three-dimensional model of the OSTR core and outlying structures as well as irradiation facilities). This involves defining surfaces, materials, and cells. Surfaces may be modeled in a variety of geometric shapes, such as lines, cylinders, cones, etc. The user creates the number of surfaces necessary to properly discretize the modeled structures. The user must also detail specific materials desired for inclusion in the calculation that describe the atomic makeup of every volume composition utilized in the model. Cells are then used in conjunction with the surface and material input information to create desired three-dimensional structures. After all desired three-dimensional structures have been created the user must define an appropriate particle and/or photon source strength and location. Since MCNP's primary purpose is to model nuclear reactor interactions, a neutron source must be input in order to stochastically calculate neutron interactions in the core.

Finally, the user must identify the desired output data from the MCNP calculation. MCNP is used for many different applications, such as criticality calculations, dose measurements, and in the case of this study, flux determination. Fluxes may be tabulated in specific irradiation facilities defined within the MCNP model by using tally cards. There are several different types of tally cards available, such as flux averaging over a

surface (F2 tally) or energy deposition averaging over a cell (F7 tally). Both of these tally cards underscore the versatility of MCNP by enabling users to calculate flux and/or dose, which is useful for multiple disciplines. This study solely uses the F4 tally card, which averages flux within a given cell. Tally cards were set up in each irradiation facility where activation foils were irradiated. These flux outputs were then input into STAY'SL in conjunction with the data from the activation foils in order to adjust the output spectrum most representatively.

The 2005 effort to characterize the HEU core neutron spectra divided the full energy range into 100 discrete energy bins (ranging from 1E-10 MeV to 20 MeV). As was done with the 2005 study, 100 energy bins were chosen to be utilized within the scope of this study in order to properly compare the current LEU core to the previous HEU core. The specific energy bins were initially used to match up to the energy bins used by the STAY'SL code's cross section calculations.

3.3 Neutron Activation Analysis

A series of activation foils are used in conjunction with a neutronics calculation (provided by MCNP) to yield a 'full', discrete energy spectrum characterization. Subjecting an activation foil to a neutron field causes the foil to become radioactive. Subsequently, the radioactive foil will typically emit a series of gamma rays. The activated foil may be placed onto a high purity germanium (HPGe) detector enabling the emitted gamma rays to be counted, yielding a spectrally-defined count rate of the sample. This is how Neutron Activation Analysis (NAA) is performed. Equation (6) displays the build-up of activity during irradiation.

$$A(t) = \sigma_a \phi N_0 (1 - e^{-\lambda t}) \tag{6}$$

A(t) is the activity of the foil as a function of time, N_0 is the number of atoms in the target foil, σ_a is the absorption cross section of the reaction of interest, λ is the decay constant

of the daughter product, and ϕ is the neutron flux. The number of atoms in the target foil is given by equation (7).

$$N_0 = N_A m f_{iso} M^{-1} \tag{7}$$

N_A is Avogadro's number, *m* is the mass of the sample, f_{iso} is the isotopic abundance of the nuclide of interest, and M is the atomic mass of the nuclide. N_0 is calculated, σ_a is obtained from a cross sectional library [7] and thus the flux may be calculated after measuring the activity on an HPGe detector.

The activity of interest is determined by counting the gammas emitted from the daughter product of the neutron bombardment. The number of daughter atoms N(t) is governed by equation (8).

$$\frac{dN(t)}{dt} = \sigma_a \phi N_0 - \lambda N(t) \tag{8}$$

Solving equation (8) with the initial condition of N(0) = 0 yields (9).

$$N(t) = \sigma_a \phi N_0 (1 - \exp(-\lambda t_0)) / \lambda \tag{9}$$

One can calculate the resultant activity $A(t_0)$ of a sample after irradiation time t_0 by multiplying equation (9) by λ to get equation (10).

$$A(t_0) = \lambda N(t_0) = \sigma_a \phi N_0 \left(1 - \exp(-\lambda t_0)\right) \tag{10}$$

After the sample is removed from the flux environment, the activity of the sample at any time t is given by equation (11).

$$A(t) = A(t_0)\exp(-\lambda t) \tag{11}$$

t_o indicates the time in which the sample was removed from the flux environment and t is the time after bombardment of interest. Figure 3–6 illustrates the build-up and decay of activity.

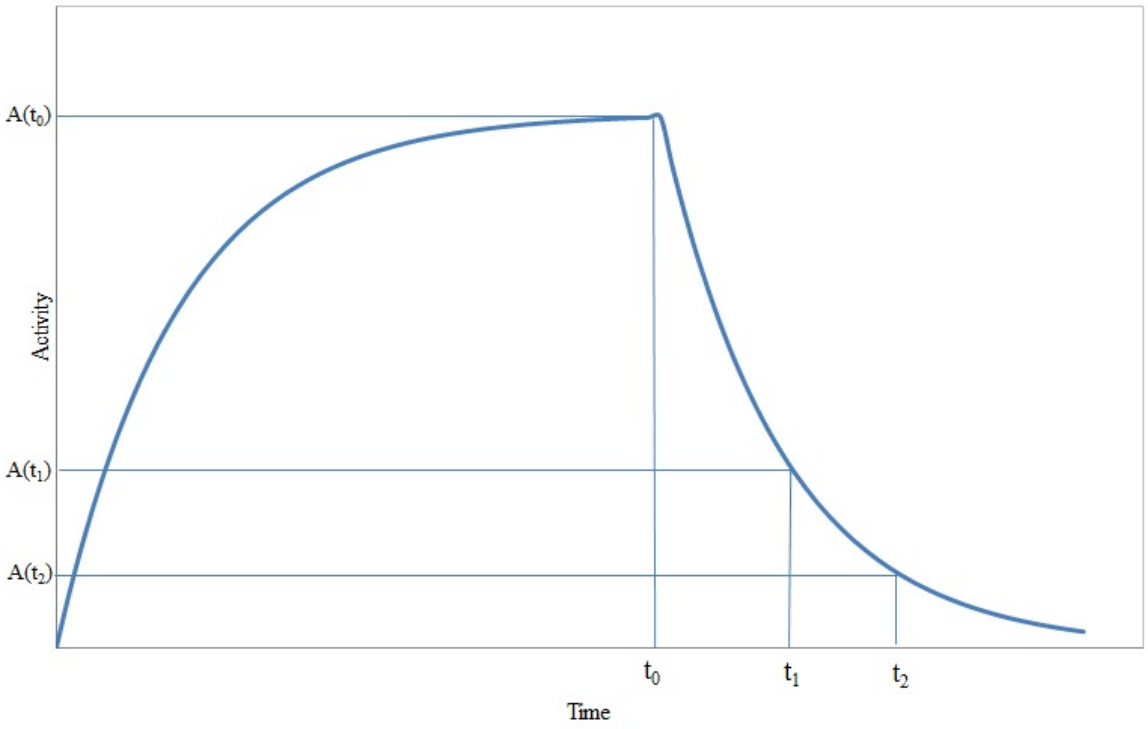

Figure 3–6: Example of activity build-up and decay

If the sample is counted in a detector with an intrinsic efficiency ε and a geometric efficiency Ω, the net number of counts C in a given spectrograph photopeak is given by equation (12).

$$C = f_\gamma \Omega \varepsilon \int_{t_1}^{t_2} A(t)dt \tag{12}$$

f_γ is the branching ratio of the nuclide of interest, t_1 is the beginning of the counting time and t_2 is the end of the counting time. Integrating equation (12) yields equation (13).

$$C = \frac{f_\gamma f_{iso} \Omega \varepsilon N_A m \bar{\sigma} \phi \left(1 - \exp(-\lambda t_0)\right)}{\lambda M} \left(\exp(-\lambda t_1)\right)\left(1 - \exp(-\lambda \left[t_2 - t_1\right])\right) \tag{13}$$

Rewriting equation (13) and solving for flux yields equation (14).

$$\phi = \frac{C \lambda M \exp(\lambda t_1)}{f_\gamma f_{iso} \Omega \varepsilon N_A m \bar{\sigma} \left(1 - \exp(-\lambda t_0)\right)\left(1 - \exp(-\lambda \left[t_2 - t_1\right])\right)} \tag{14}$$

In order to accurately determine the activity of the irradiated foil, a quantification of the detector efficiency (in this case the HPGe) must be taken into account before attempting to calculate activity. The detector efficiency is quantified through the use of NIST standard sources of known quantities (i.e. its activity, emitted isotopes, abundance of isotopes and creation date). A europium source was used for this study's efficiency calibration. The efficiency is calculated by the detector software.

It should be noted that the STAY'SL input decks utilize "sigma-phi" activities. These activities are simply the value calculated in equation (14) with each side multiplied by the cross section (thus the term "sigma-phi"). These values are in units of atoms/atoms-sec; they are reaction rates per target atom.

3.4 Spectrum Unfolding

"Spectrum unfolding" refers to the act of comparing a set of experimental activations (obtained from foil irradiations) with a theoretical input spectrum (obtained from MCNP). The activations are used to adjust the theoretical spectrum to produce a more accurate result. The total amount of neutrons, n'", in a given volume is given by the expression in equation (15).

$$n''' = \int_0^{\infty} n'''(E)dE \tag{15}$$

All of the energy-dependent neutrons n’’’(E) are integrated over the full energy range from 0 to ∞ to yield the total neutrons in the given volume. The full energy range from 0 to ∞ is discretized numerically by the aforementioned 100 energy bins in MCNP, from 1E-10 MeV to 20 MeV, and experimentally by irradiating a wide range of materials which have an affinity for interacting with neutrons over prescribed regions within the entire energy range. The numerical results are augmented by the experimental data using a dosimetry unfolding code. This study employs the STAY’SL least-squares adjustment code, which was the same code used during the previous HEU characterization. STAY’SL allows the user to input a flux distribution, activation data, and cross section information and perform a least-squares fit calculation based on minimizing the chi-squared (χ^2) value [16].

χ^2 is a variable that characterizes the dispersion of the observed frequencies x_i (in this study, the data obtained from the activation foils) from the expected frequencies x_e (the data calculated from MCNP) [27]. χ^2 is defined in equation (16), with R representing the number of activation reactions used in the study.

$$\chi^2 = \frac{1}{\bar{x}_e}\sum_{i=1}^{R}(x_i - \bar{x}_e)^2 \tag{16}$$

STAY’SL calculates a minimized reduced χ_m^2, which is χ^2 divided by R-1. A table of reduced χ_m^2 distributions [27] displays the probability that a distribution is larger than the reduced χ_m^2 value with respect to the number of degrees of freedom. According to Perey [16], values of χ_m^2 between 0.3 and 2.0 indicate that the adjusted spectra are a likely solution.

4. REACTOR DESCRIPTION

The OSTR is a TRIGA® Mark II Reactor. The TRIGA® reactor was designed by General Atomics to be, according to Frederic de Hoffmann, "safe even in the hands of a young student" [28]. The acronym TRIGA® stands for Training, Research, Isotopes, General Atomics. The primary mission of the OSTR is "*...to serve as the campus wide teaching, research, and service facility for programs involving the use of ionizing radiation and radioactive materials.*" [29]

The OSTR is a pool-type reactor. The reactor core is underneath 16 feet of water, centrally located within an aluminum tank surrounded by an 8 foot thick concrete biological shield, or bioshield (Figure 4–1). The OSTR is licensed to operate at a maximum of 1.1 MW of thermal energy. The licensed power level of the OSTR is sufficiently low such that forced cooling is not required; as a result, the reactor is cooled via natural convection [1,45].

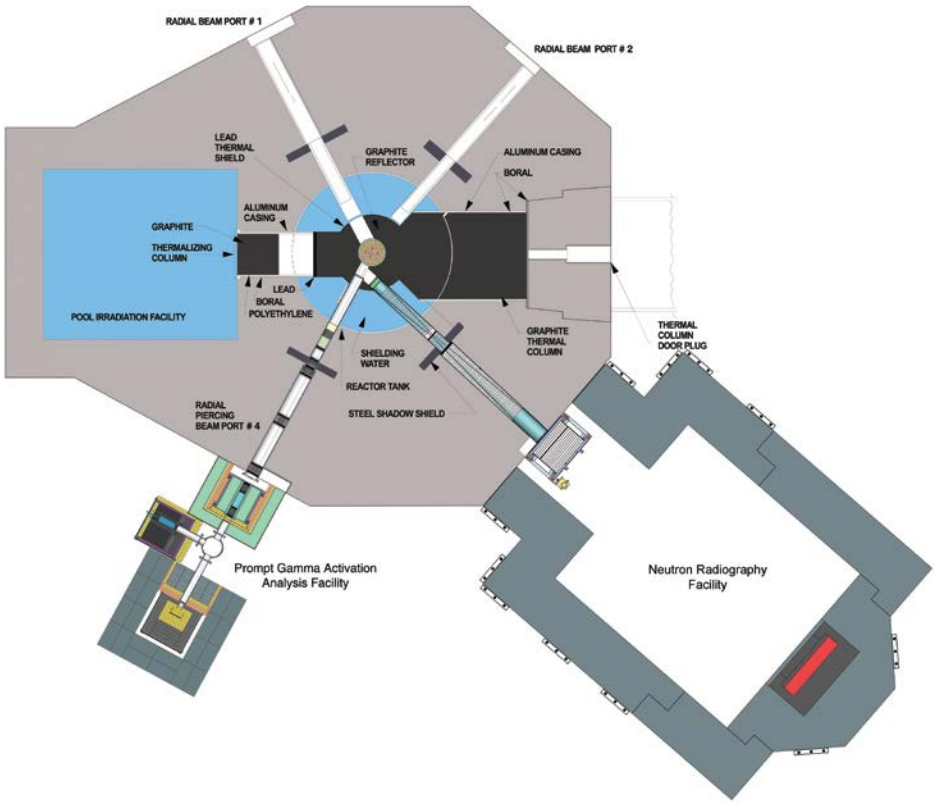

Figure 4–1: Overhead view of OSTR and outlying irradiation facilities

Four beam ports penetrate the reactor's bioshield, two of which are currently utilized by the NRF and the Prompt Gamma Neutron Activation Analysis (PGNAA) facilities. A thermal column irradiation facility (discussed in Section 4.6) and thermalizing column (currently unused at the OSTR) are positioned adjacent to the reactor tank (Figure 4–1).

The OSTR core has seven concentrically aligned circular rings facilitating a total of 127 in-core positions, or lattice locations. The rings are lettered A through G; each lattice position is numbered within a given ring (Figure 4–2).

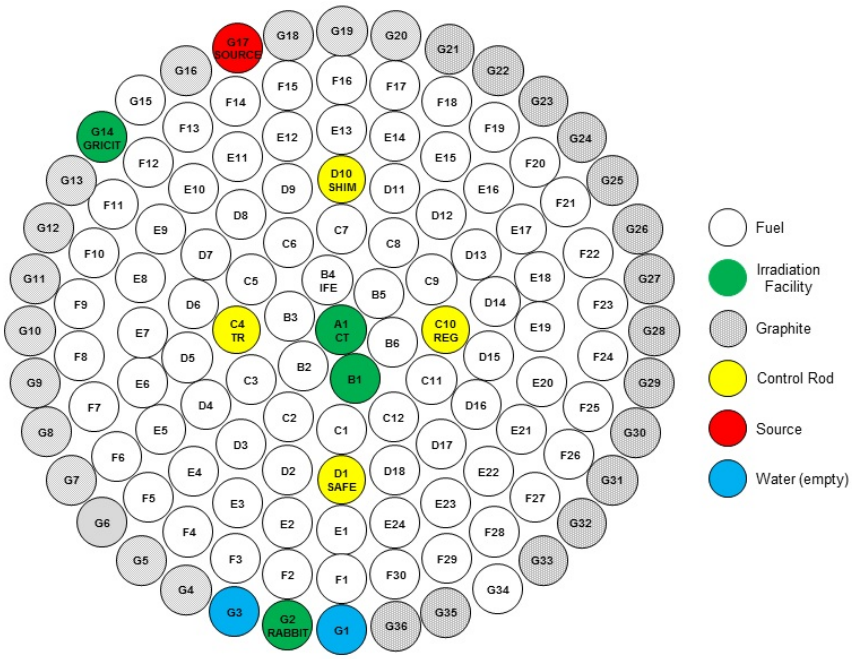

Figure 4–2: LEU core configuration (as of June 1, 2012)

The OSTR utilizes an americium-beryllium neutron source for start-up and low power flux monitoring. The neutron source is contained in an aluminum tube with similar exterior dimensions to a fuel rod and is kept in the G17 location.

The OSTR contains approximately 90 fuel rods. Each fuel rod is 1.47 inches in diameter and has 15 inches of active fuel length (Figure 4–3) surrounded by graphite plugs on the top and bottom of the fueled section. These graphite plugs act as a reflector in their

respective locations, enabling a more efficient neutron population by reflecting neutrons back into the fuel region.

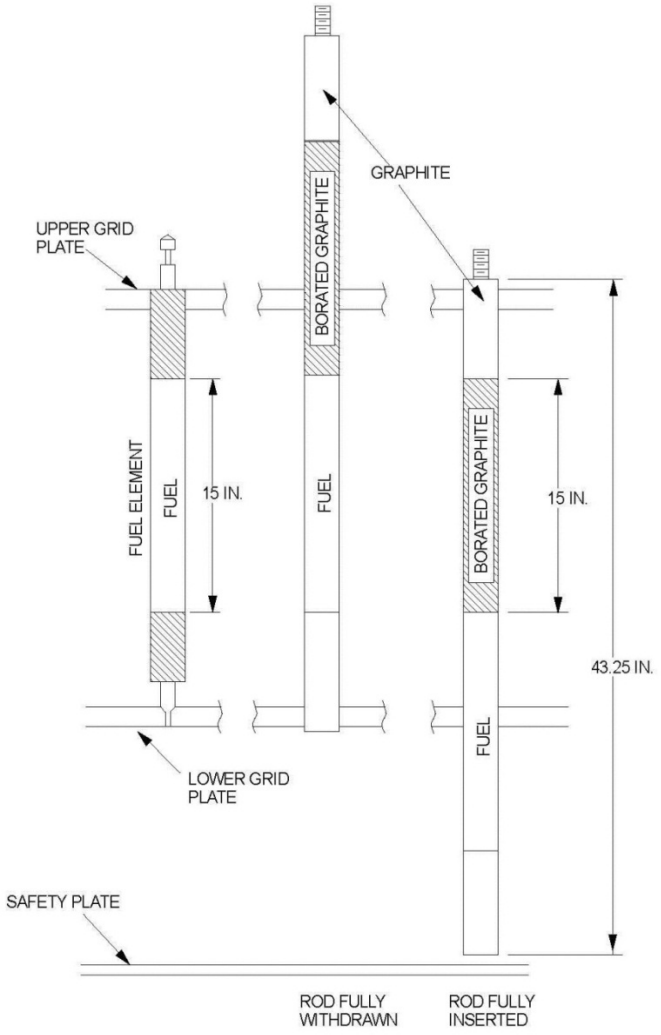

Figure 4–3: Side-view of fuel rods and fuel-followed control rods [30]

The OSTR LEU fuel is 30 weight percent uranium enriched to 19.75% ^{235}U. The remaining weight percent of the fuel is comprised of zirconium hydride and erbium. The zirconium hydride and erbium are mixed homogeneously with the uranium. The zirconium hydride provides neutron moderation and also causes the fuel to have a large negative temperature coefficient. As the fuel begins to heat up, the hydrogen atoms in the hydride begin to oscillate. Thermal neutrons that interact with the oscillating hydrogen atoms will gain energy, hardening the thermal spectrum. Along with the thermal

spectrum hardening, the erbium resonances experience Doppler broadening and absorb a portion of the upscattered neutrons (as well as downscattered neutrons). This effectively decreases the reactivity [30].

The OSTR LEU fuel contains approximately 1.1 weight percent of erbium. Erbium is a burnable poison that is necessary to counteract the large amount of excess reactivity due to the large amount of uranium in the fuel at initial fuel loading. Erbium also increases the prompt negative temperature coefficient due to having large epithermal resonances (Figure 3–3).

In order to safely monitor fuel temperature and prevent possible fuel failures, the OSTR employs an instrumented fuel element (IFE) in the B4 location. This location is near the center of the core and thus sees the highest temperatures in the reactor, as flux (and subsequently temperature) is the highest at the center of a symmetric reactor [31]. The IFE has three redundant thermocouples imbedded within its fueled region to facilitate the safe and reliable monitoring of fuel temperature.

All of the irradiation facilities are axially positioned within the fueled region of the reactor core (Figure 4–4). Each facility has a different axial position within the core; each position is described in fuller detail in the corresponding facility’s subsection in this chapter.

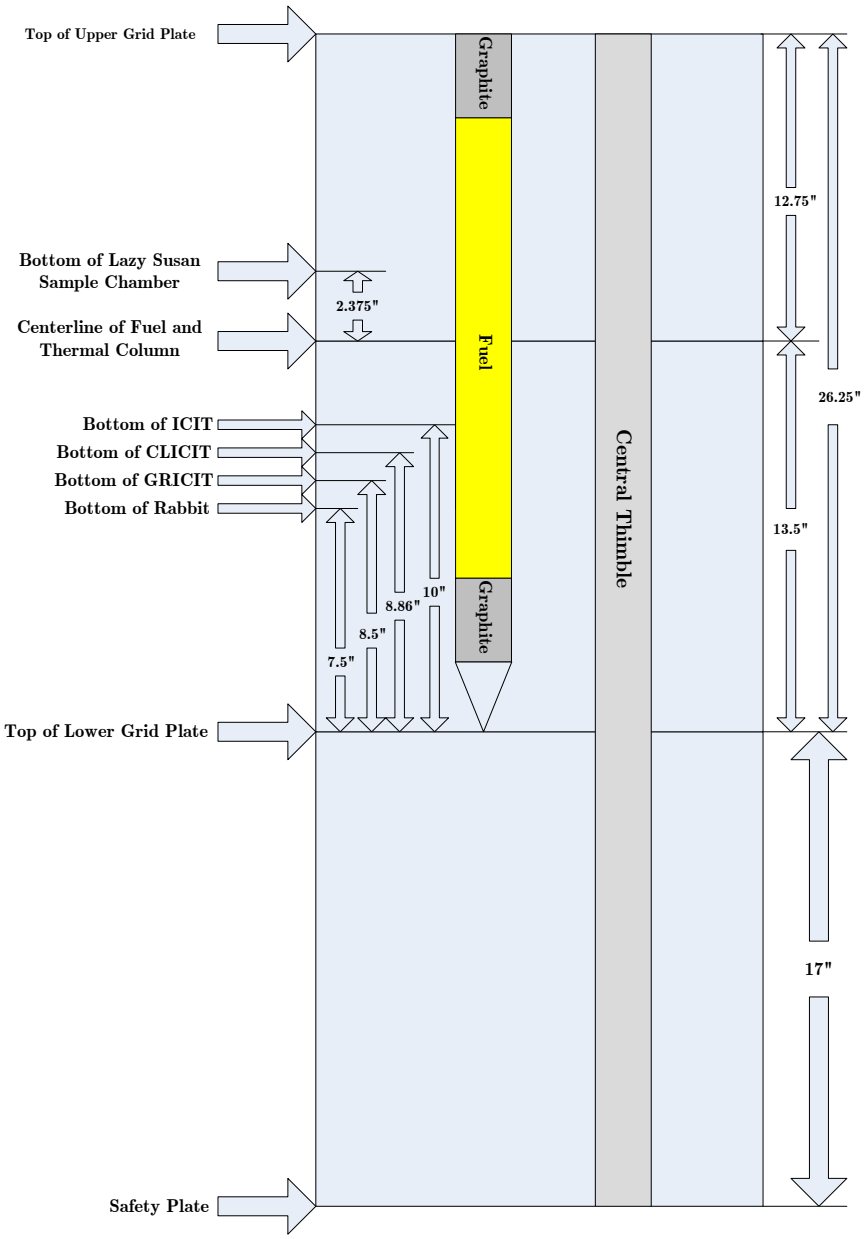

Figure 4–4: Side-view of reactor core with axial locations of irradiation facilities

The OSTR has four borated graphite control rods (referred to as the Transient, Safety, Shim and Regulating rods), two of which are located in the C ring while the other two are located in the D ring opposite one another azimuthally within the core (Figure 4–2). The transient rod is a pneumatic rod that allows operators to “pulse” the reactor. A pulse refers to the rapid insertion of a sufficiently large amount of positive reactivity by pneumatically ejecting the transient rod from the core such that the reactor is put into a

prompt supercritical state. As the neutron-absorbing rod is ejected from the core, the fuel rapidly heats up. As temperature rises, the prompt negative temperature coefficient quickly reduces power. The entire pulse event takes place in less than one second.

The transient rod is an air-followed control rod while the other three rods are fuel-followed. In the fuel-followed control rods, as the absorber section is removed from the core, it is replaced with fuel in order to maintain reactivity and avoid having a flux-peaking water void in the middle of the core.

The OSTR contains three radial plates: the upper grid plate, the lower grid plate and the safety plate. Fuel, irradiation tubes, graphite and other miscellaneous items must pass through the upper grid plate to enter the core region. The lower grid plate is a support plate and has small countersunk holes that allow fuel elements' and graphite elements' lower-end fixtures to be supported. The elements are then held in place by the upper grid plate (Figure 4–3). The safety plate is below the lower grid plate; its purpose is to prevent controls rods from completely falling through the bottom of the core.

The OSTR has three designated core configurations which are all determined by the contents of the B1 grid position. If fuel is in the B1 position, the OSTR is in the NORMAL core configuration. The other two core configurations are the ICIT and the CLICIT core configurations. Both facilities are described later in this chapter.

4.1 Rotating Rack (Lazy Susan)

The Rotating Rack, most commonly referred to as the "Lazy Susan", is an irradiation facility located on the periphery of the OSTR core. It is a welded cylindrical aluminum can that houses a rack of 40 evenly-spaced sample tubes (Figure 4–5) [32]. The samples sit approximately 2.375 inches above the fuel centerline (Figure 4–4). Samples are loaded and retrieved from the reactor top. The rack is rotated via a drive system on the reactor top's center channel. The rotation of the rack provides for an even fluence to all samples in the Lazy Susan. This facility is primarily employed for NAA, which is used in a variety of fields, such as archaeometry [33], biology [34] and radiochemistry [35]. The

rotating rack is ideal for irradiations that have many samples and do not require a high fluence for activation.

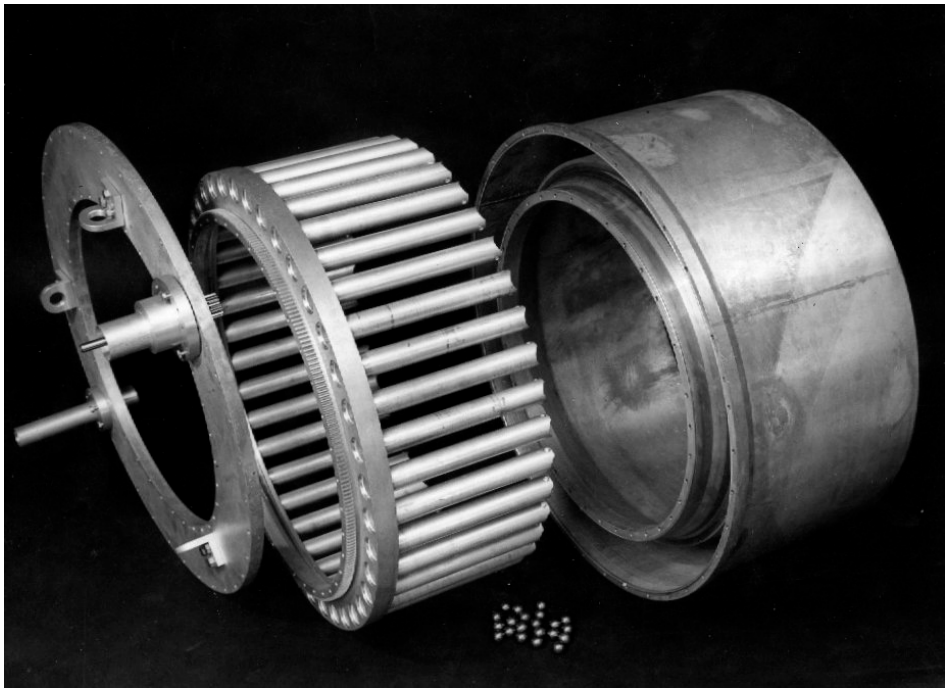

Figure 4–5: Disassembled Rotating Rack [32]

Samples are typically irradiated in a polyethylene "TRIGA® tube" but may be irradiated in aluminum TRIGA® tubes for longer irradiations (Figure 4–6).

Figure 4–6: Polyethylene (upper) and aluminum (lower) TRIGA® tubes

The irradiation sample tubes may accommodate samples having a maximum length of approximately four inches. Lazy Susan samples in polyethylene require double encapsulation; therefore, all samples must be of appropriate size as to fit into its primary encapsulation (typically a maximum size of a 4 dram polyethylene vial).

4.2 In-Core Irradiation Tube (ICIT)

The ICIT is one of two irradiation facilities used in the B1 grid position (its counterpart being the CLICIT). The ICIT consists of two aluminum tubes: the inner tube is a 1.25 inch outer diameter (OD) aluminum tube with a wall thickness of 0.058 inches [30]. It is approximately 19 feet long with a 16 inch offset that prevents highly-collimated beams of radiation from streaming out of the reactor core (Figure 4–7). At the bottom of the inner tube is an outer tube which is 1.5 inches OD with a wall thickness of 0.065 inches turned down to 1.475 inches OD. This outer tube is approximately 3.5 feet long and serves as the facility in-core terminus. A spacer is placed in the bottom of the ICIT in order to raise samples into the peak flux region in the facility. The spacer in the ICIT (Figure 4–7) places samples at 10 inches above the lower grid plate (Figure 4–4).

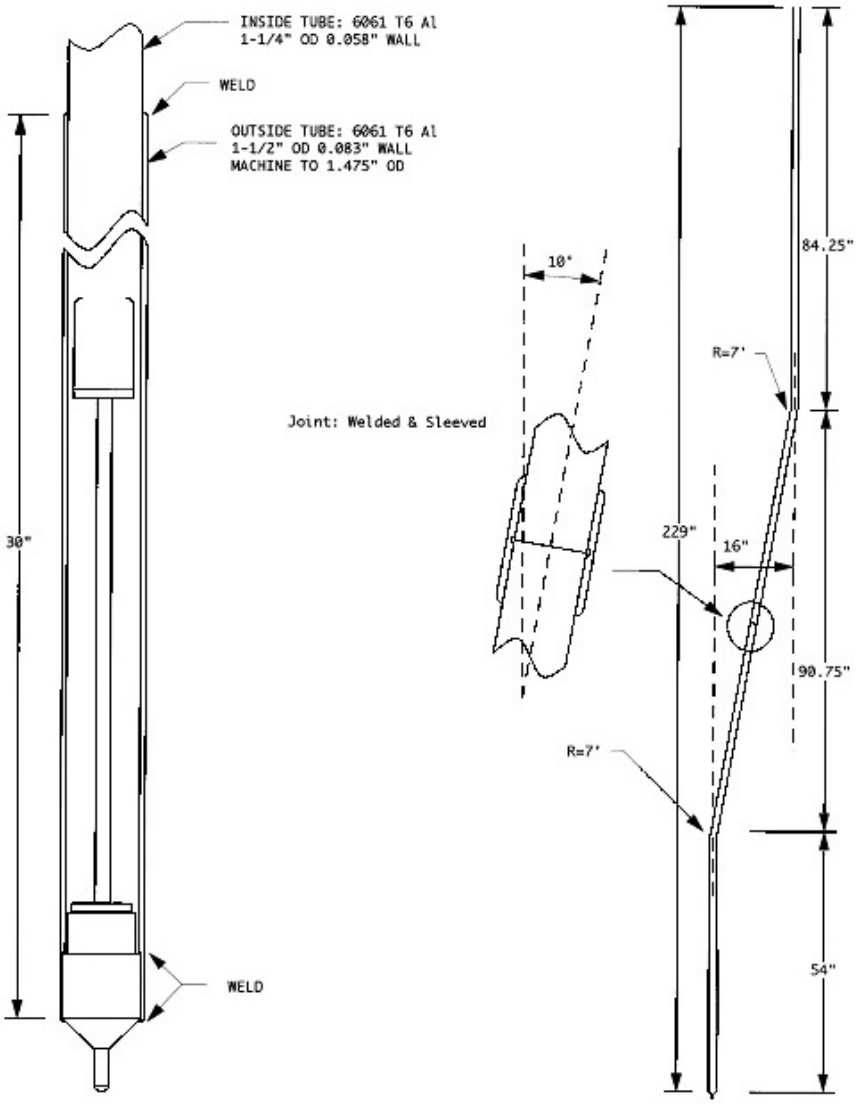

Figure 4–7: Cross-sectional view of ICIT

The ICIT is a water-tight aluminum tube. There is no lining in the ICIT; samples in this facility are exposed to the entire energy spectrum of neutrons. Current uses for the ICIT facility include antimony source production (though antimony is preferentially produced in the GRICIT), $^{40}Ar/^{39}Ar$ age dating [36], and student lab experiments involving axial flux determination.

4.3 Cadmium-Lined In-Core Irradiation Tube (CLICIT)

The CLICIT is identical to the ICIT (Figure 4–7) with the exception of a 0.020 inches thick cadmium sleeve that is wrapped around the inner aluminum tube. A disc of cadmium is also placed at the bottom of the CLICIT, ensuring that the CLICIT terminus is completely shielded with cadmium, minimizing thermal neutron penetration into the irradiation facility. The CLICIT is arguably the most "popular" facility at the OSTR and is primarily used for $^{40}Ar/^{39}Ar$ age dating [37], as the necessary reaction of $^{39}K(n,p)^{39}Ar$ is a threshold reaction that takes place in the fast neutron energy spectrum. Irradiating samples in the CLICIT removes most of the "noise" from thermal neutron reactions.

A spacer is placed in the bottom of the CLICIT in order to raise samples into the peak flux region in the facility. The spacer in the CLICIT (Figure 4–7) places samples at 8.86 inches (22.5 cm) above the lower grid plate (Figure 4–4).

The OSTR has two CLICITs available for users. It is a simple process to change between the two CLICITs and allows the OSTR flexibility in operating schedule and allows the operating staff the ability to accommodate shorter irradiations in the event of a long in-core irradiation. If a user has a 100-hour irradiation and another user requests a one-hour irradiation, the short irradiation can be performed with minimal waiting time and inconvenience to the 100-hour user.

4.4 G-Ring In-Core Irradiation Tube

The GRICIT is identical to the ICIT in all geometric and material characteristics (Figure 4–7), except for its core lattice position. The GRICIT is located in the G14 grid location. A spacer, or 'saddle', is placed in the bottom of the GRICIT in order to raise samples into the peak flux region in the facility. The saddle in the GRICIT places samples at 8.5 inches above the lower grid plate (Figure 4–4).

The only current use of the GRICIT is for antimony production. Antimony production consists of activating small quantities of naturally occurring antimony slugs to desired prescribed activity levels. This function within the OSTR does not require

characterization or utilization of a well quantified neutron spectrum. However, this study intends to quantify the neutron spectrum in the GRICIT such that the irradiation facility may be utilized for experimental purposes other than antimony production in the future.

The GRICIT is analyzed in both the CLICIT and ICIT core configurations to determine the effects of core configuration on GRICIT spectra. Hereafter, GRICIT experiments performed in the CLICIT core will be referred to as GRICIT-C, and likewise GRICIT-I for ICIT core experiments.

4.5 Pneumatic Transfer System (Rabbit)

The Rabbit facility is a pneumatic transfer system that allows samples to be rapidly injected into the periphery of the reactor core (grid position G2). The sample lands on a shock absorber inside of the terminus assembly at the peak axial flux position (Figure 4–8).

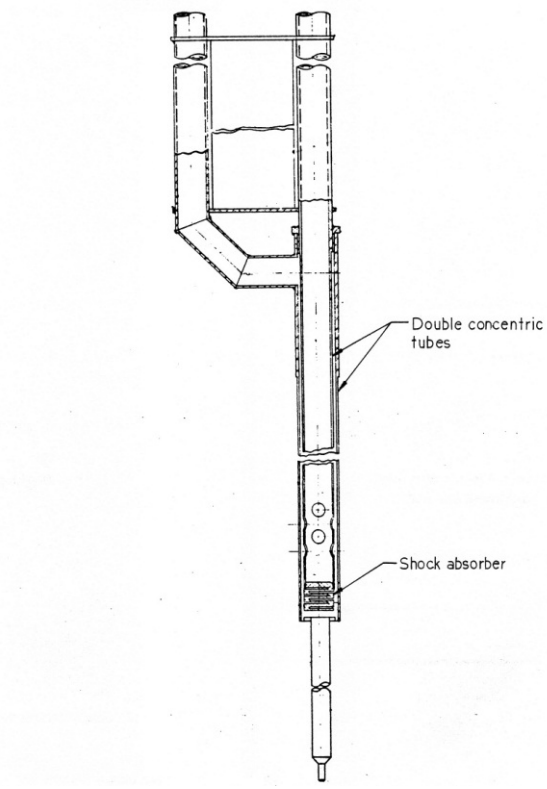

Figure 4–8: Rabbit terminus

The advantage that this facility provides is the ability to examine short-lived isotopes. A newly-installed control system allows fine-tuned sample injection times with accuracy on the order of a tenth of a second (Figure 4–9). Samples are sent to the reactor by pressing the “send” button on the digital console (Figure 4–9). The digital counter starts when the sample passes by an optical sensor near the top of the reactor tank. After the sample has been irradiated for the programmed amount of time, the sample is then returned to the injection point. The ability to rapidly irradiate and examine samples is ideal for short-lived isotope studies [38].

Figure 4–9: Rabbit control panel

4.6 Thermal Column

The thermal column is a facility located outside of the reactor, on the east side of the core. It consists of long “stringers” made out of graphite. Samples are placed in the center of the thermal column where one stringer has been permanently removed (Figure 4–10). Since the facility is located adjacent to the reactor and is surrounded by graphite, the samples primarily experience thermal neutrons, as the mean free path of neutrons in

graphite is much shorter than the distance between the reactor core and the thermal column. This facility is primarily used for fission track dating [39] but has been used for other low-fluence irradiations [46,47].

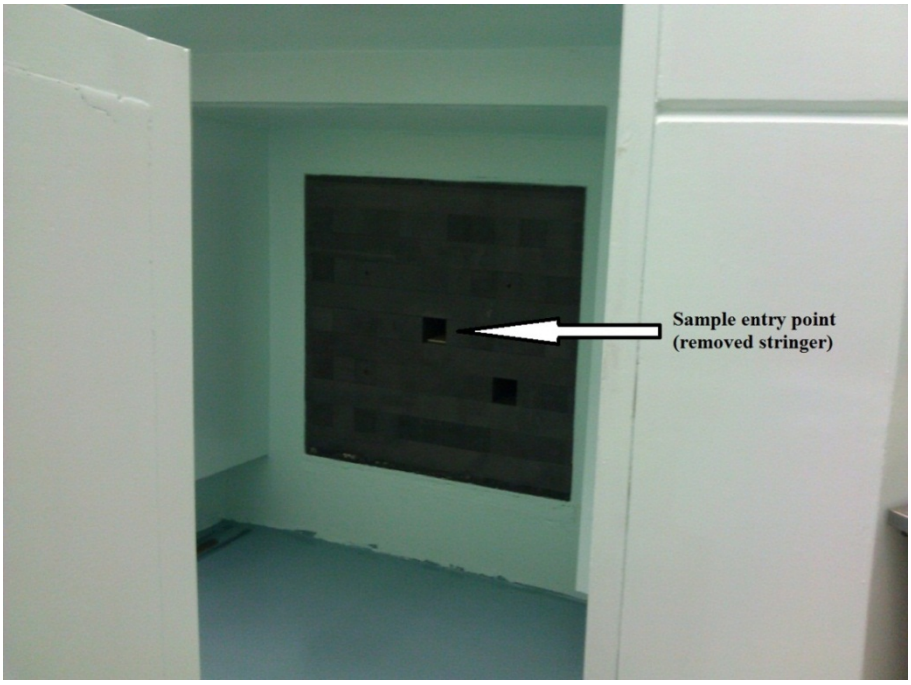

Figure 4–10: Inside of thermal column

4.7 Central Thimble

The central thimble is located at the center of the core in the A1 position. It is a 1.25 inch aluminum tube that extends from the reactor top to the bottom of the reactor core. The central thimble has holes at the bottom of the facility which causes the facility to be flooded during normal operations. The central thimble has the ability to purge the water with air by using a special venting cap; the OSTR does not currently offer this option. Currently the central thimble is filled with an aluminum plug in order to prevent flux peaking in the center of the core due to a water void in the hottest core region, however, other organizations that have similar research reactors to the OSTR have utilized their central thimble [40]. The aluminum plug contains a 0.375 inch hole drilled through its entire axial center, which enabled this study's central thimble axial flux determination.

5. METHODS AND MATERIALS

This section discusses the methods used to calculate the LEU spectra and the materials involved during the experimental irradiations.

5.1 Neutronics Calculations (MCNP)

One of the primary objectives of this study is to characterize the LEU neutron spectra in the largely used irradiation facilities of the OSTR. However, in addition to this characterization, it is also desired to compare the current spectra resulting from LEU fuel to that of the previously utilized core containing HEU fuel. The study performed in 2005 sufficiently characterized the HEU core; the spectra resulting from the 2005 study will ultimately be compared against the spectra from this study. Prior to objectively comparing the spectra in the 2005 and current MCNP models, a bias quantification must be made. This bias tabulation is performed in order to quantitatively observe differences in the 2005 and current models as a result of altered modeling resolution, including those amongst materials and geometry. In order to compare the bias between the 2005 and current MCNP models, the current MCNP model was rewritten to reflect the identical core configuration of the 2005 model (Figure 5–1). The fluxes in the ICIT were then compared; specifically, the tally cell 8023 which represents the peak axial flux position in the ICIT. Figure 5–2 compares the neutron spectral distribution in the ICIT between the two models.

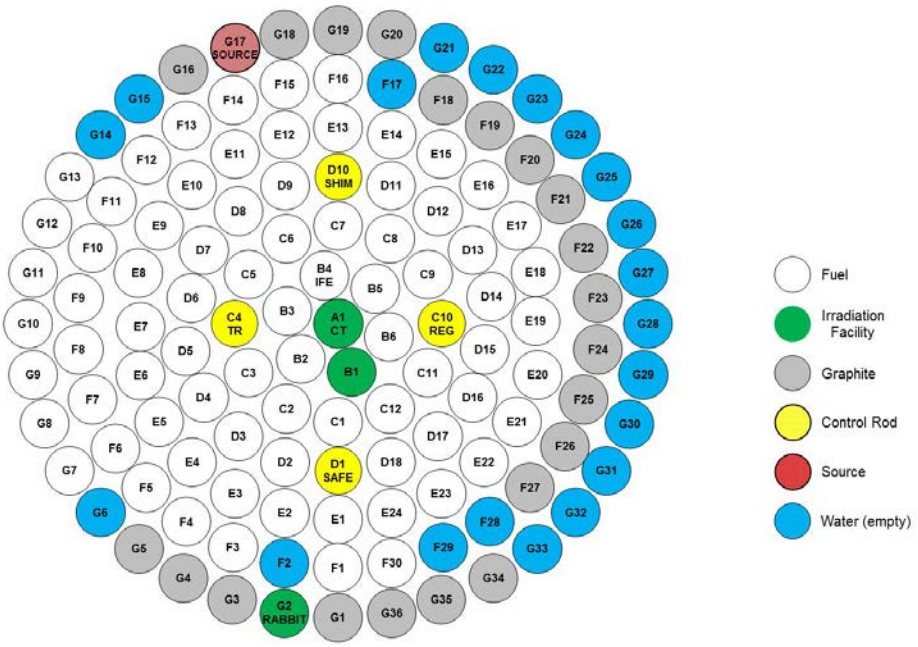

Figure 5–1: Core configuration of 2005 MCNP model (HEU Core)

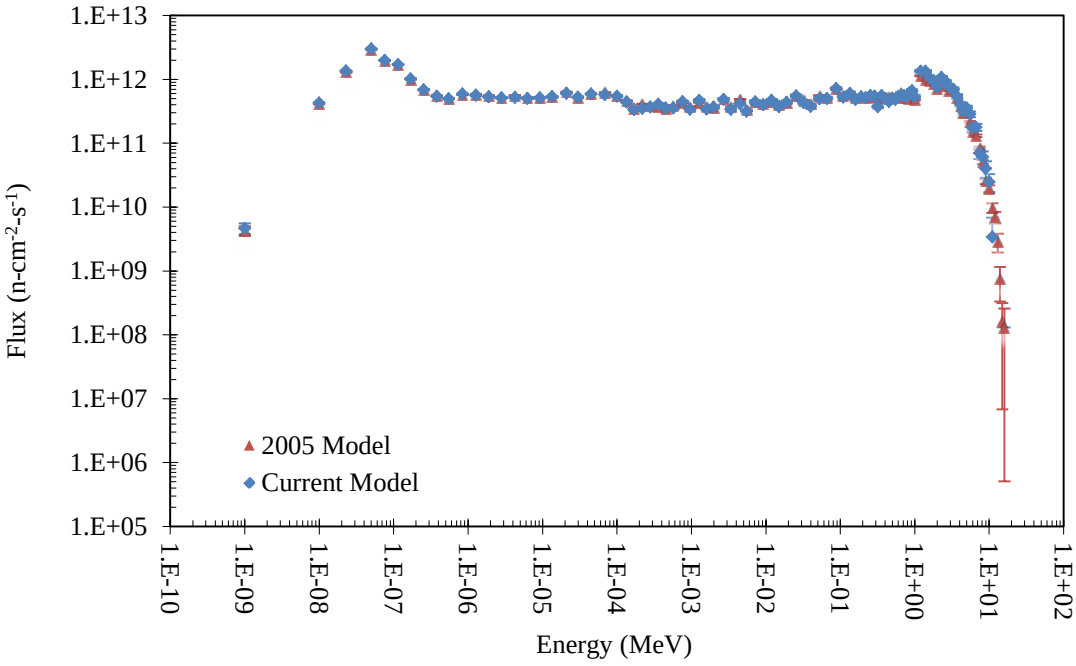

Figure 5–2: Comparison of MCNP-predicted fluxes in peak axial flux position of ICIT

Figure 5–2 demonstrates that minimal differences exist between the two models' ability to predict neutron spectra in the central region of the core, although the current model does not tabulate any neutrons above 11 MeV, whereas the 2005 model measures neutrons in every energy bin (albeit with very high error above 12 MeV). The thermal and epithermal flux spectra are nearly identical between the two models.

The current model was also rewritten to accommodate improvements in the thermal column flux determination using the DXTRAN particle placed at the face of the thermal column (tally cell 16021 in both MCNP decks). Figure 5–3 shows the comparison of the thermal column flux between the two models.

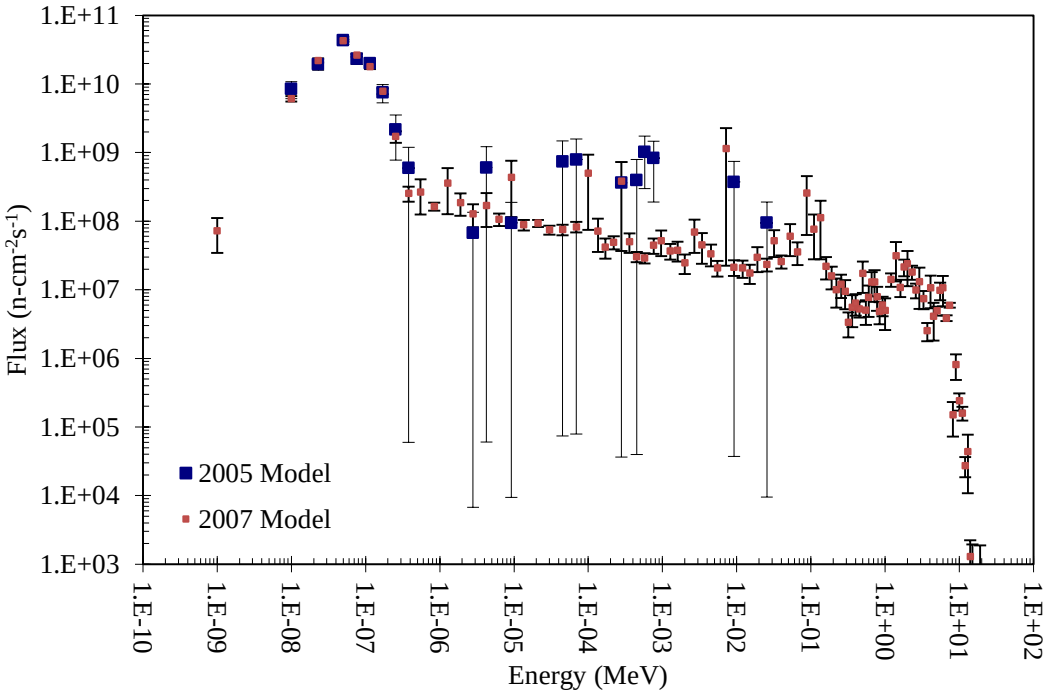

Figure 5–3: Comparison of thermal column flux models (HEU Core)

Both models similarly predict the neutron spectrum below 0.1 eV, however the DXTRAN particle markedly improved upon the flux determination yielding from the 2005 study. The current model has far more accuracy in the epithermal range with minimized error (down from 100% error to approximately 30% error).

Having verified the interchangeability of the 2005 and current models, the current model was rewritten to reflect the LEU core presented in Figure 4–2. Two versions of the MCNP model were written: one for the CLICIT core configuration and one for the ICIT core configuration. Flux tally cards were added for the GRICIT, which was not previously modeled.

5.2 Foil Activation Experiment

There are two types of activation reactions that are examined in this study: (1) threshold reactions and (2) radiative capture reactions. As previously discussed, threshold reactions involve the emission of a particle. These reactions only occur in the fast spectrum. As such, there are a variety of foils that may be utilized to cover a range of fast energies. This study uses three specific fast energy foil materials: (1) nickel, (2) indium, and (3) titanium. Many different foil types were used with regard to radiative capture reactions including: (1) aluminum-gold (0.134% gold), (2) iron, (3) scandium, (4) lutetium-aluminum (5.2% lutetium), (5) tungsten, (6) sodium chloride, and (7) molybdenum.

Table 5-1 summarizes all of the foils used, the neutron interactions of interest, and the useful energy ranges of each interaction. All foil ranges are estimates based off of the ENDF/B-VII.0 cross section plots for the respective reactions [41]. The thermal/epithermal cutoff was estimated to take place at the energy level which resonances began, and the upper bound of the epithermal region was estimated to take place at the energy level at which resonances become unresolved for a given material.

Table 5-1: Summary of all neutron reactions to be examined

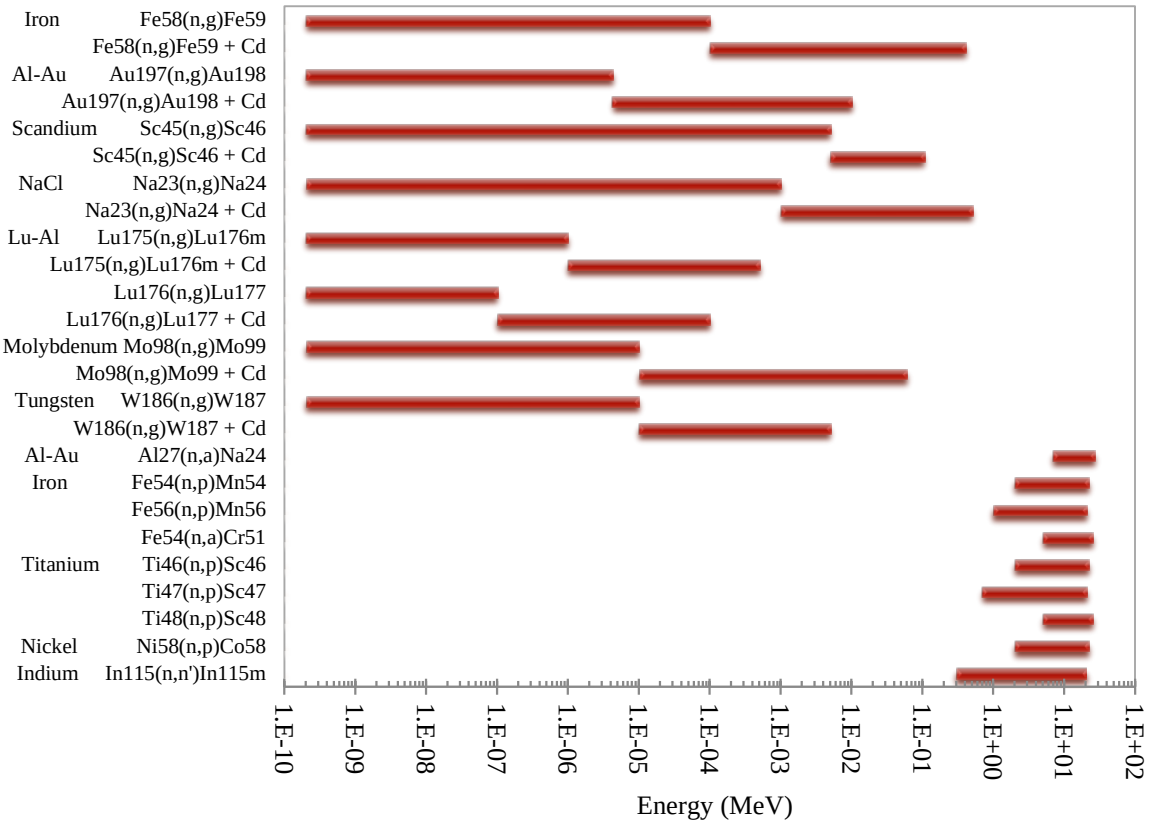

Three sets of threshold foils and three sets of thermal/epithermal foils (bare and cadmium covered) were irradiated in each facility in order to adequately cover the full range of energies seen in each facility. Titanium, nickel, indium, iron and aluminum-gold were used in each facility because there was an abundance of said foils on-hand. The other foils were used to enable redundant experimental data to be collected within overlapping energy regions.

The foil samples were prepared in accordance with applicable OSTR operating procedures. For in-core irradiation facilities (ICIT, CLICIT, GRICIT), the foils were simply placed into a sealed aluminum TRIGA® tube (Figure 4–6). Cadmium-covered foils were placed inside cadmium covers, then wrapped in aluminum foil to preclude the possibility of the foils falling out of the otherwise unsealed covers. All of the foils are 0.5 inches in diameter (Figure 5–4), with varying thicknesses. All of the foils are quite thin, which minimized the effects of self-shielding. Small holes were drilled into the top of the

aluminum TRIGA® tube so that fishing line could be tied to the sample tube. This allowed the experimenter to rapidly remove samples from the core, which allowed for more accurate irradiation time collection.

Figure 5–4: Indium foil and cadmium cover

In the Lazy Susan, bare foils were placed inside 2-dram polyethylene vials then packed with Styrofoam to ensure that the foils remained at the bottom of the vial. Those foils requiring a cadmium cover were placed in their respective covers, wrapped in aluminum foil, placed inside 4-dram polyethylene vials then packed with Styrofoam. Lastly, the vials were heat-sealed and placed inside polyethylene TRIGA® tubes.

Foils intended for irradiation in the thermal column were placed inside polyethylene TRIGA® tubes in the same fashion as the in-core experiments. The TRIGA® tubes were filled with Styrofoam to ensure that the foils remained at the bottom of the tube.

Preparation of samples for irradiation in the Rabbit required the most significant care and diligence. Due to the relatively small physical size of the Rabbit sample receiver assembly and the Rabbit sample vials, sample encapsulations are limited to 2-dram vials. This is adequate for bare foil irradiations, which were prepared in the same way as the

Lazy Susan samples. Encapsulation of bare wire samples was not significantly cumbersome; however cadmium-covered samples must be placed perpendicular to the axial length of the 2-dram vials.

The foils were all individually irradiated for varying times (Table 5-2) determined from flux estimates in each facility and reactor availability, with the intended goal of producing an appreciable amount of activity while not receiving excessive detector dead-time upon counting. All foils were irradiated at an integral reactor power of 1 MW_{th}.

Table 5-2: Foil irradiation times (in seconds) for each facility

Foil	CLICIT	GRICIT-C	GRICIT-I	ICIT	LS	Rabbit	TC
Fe (bare)	600	600	600	300	3600	60	19800
Fe (covered)	N/A	1200	1200	600	3600	60	25200
Al-Au (bare)	60	60	60	60	265	60	19800
Al-Au (covered)	N/A	120	120	120	258	60	25200
Sc (bare)	N/A	60	N/A	N/A	600	N/A	19800
Sc (covered)	N/A	600	N/A	N/A	598	N/A	25200
Lu-Al (bare)	N/A	N/A	120	N/A	N/A	N/A	N/A
Lu-Al (covered)	N/A	N/A	120	N/A	N/A	N/A	N/A
Mo (bare)	N/A	N/A	N/A	N/A	N/A	60	N/A
Mo (covered)	N/A	N/A	N/A	N/A	N/A	60	N/A
W (bare)	N/A	N/A	N/A	60	N/A	N/A	N/A
W (covered)	N/A	N/A	N/A	120	N/A	N/A	N/A
NaCl	60	N/A	N/A	N/A	N/A	N/A	N/A
Ti	120	300	300	120	283	60	N/A
Ni	120	300	300	120	290	60	N/A
In	60	60	60	60	273	6	19800

All of the in-core irradiations were relatively short (e.g. approximately five minutes). A stopwatch was used in order to maximize the time accuracy of the irradiations. The counted irradiation time started at the instance the sample reached the bottom of the in-core tubes; irradiation time ended at the instance the sample was removed from the core region. Immediately following irradiation, samples were removed via fishing line and stored approximately 10 feet above the reactor core to allow for short-lived isotopes to decay (especially the activated aluminum TRIGA® cans).

The thermal column cannot be easily accessed during/after operations; for this reason irradiation times were fixed depending on the reactor schedule (thus the 19800 second time for the bare/fast foils and the 25200 second time for the cadmium-covered foils).

The design of the Lazy Susan prevents simultaneously loading of samples; it is for this reason that a select number of samples have non-standard irradiation times (e.g. aluminum-gold, scandium and threshold foils). Samples are loaded one at a time into the Lazy Susan and a hand crank must be rotated in order to index from one sample position to the next. The difference in time between samples loaded in one position versus that of the next was diligently logged and subtracted from the total irradiation time with the use of an alternate stopwatch. At the end of the desired irradiation period, the reactor was scrammed (control rods immediately inserted) for the most accurate irradiation time.

After irradiation, samples were transferred to clean 2-dram vials and were counted on an HPGe detector. Counts were collected for various reactions of interest as identified in

Table 5-3. These reactions were chosen because the daughter products emit well-defined gammas that allow for good statistical counting. The respective gamma energies and branching ratios (percentage of gammas emitted per 100 emissions) were obtained from the National Nuclear Data Center [41]. The resulting counts were then tabulated in a spreadsheet to calculate sigma-phi reaction rate values (discussed in Section 3.3) for STAY'SL input decks.

Table 5-3: Summary of reactions of interest

Foil	Reaction	Gamma Energy (MeV)	Branching Ratio
Fe	Fe-58(n,g)Fe-59	1099.3	56.50%
		1291.6	43.20%
	Fe-54(n,p)Mn-54	834.8	99.98%
	Fe-56(n,p)Mn-56	846.8	98.85%
		1811.2	26.90%
		2112.6	14.20%
	Fe-54(n,a)Cr-51	320.1	9.91%
Al-Au	Al-27(n,a)Na-24	1368.6	99.99%
		2754.0	99.86%
	Au-197(n,g)Au-198	411.8	95.62%
Sc	Sc-45(n,g)Sc-46	889.3	99.98%
		1120.5	99.99%
Lu-Al	Al-27(n,a)Na-24	1368.6	99.99%
		2754.0	99.86%
	Lu-175(n,g)Lu-176m	88.4	8.90%
	Lu-176(n,g)Lu-177	112.9	6.17%
		208.4	10.36%
Mo	Mo-98(n,g)Mo-99	181.1	6.14%
		739.5	12.26%
W	W-186(n,g)W-187	685.8	33.20%
		479.5	26.60%
		772.9	5.02%
		618.4	7.57%
		551.6	6.14%
		134.2	10.36%
		720.0	13.55%
NaCl	Na-23(n,g)Na-24	1368.6	99.99%
		2754.0	99.86%
In	In-115(n,n')In-115	336.3	45.80%
Ni	Ni-58(n,p)Co-58	810.8	99.45%
Ti	Ti-46(n,p)Sc-46	889.3	99.98%
		1120.5	99.99%
	Ti-47(n,p)Sc-47	159.4	68.30%
	Ti-48(n,p)Sc-48	983.5	100.10%
		1312.1	100.10%
		1037.5	97.60%

5.3 Spectrum Unfolding (STAY'SL)

The STAY'SL program was employed to adjust the theoretical MCNP flux output using the experimental activities obtained from the foil irradiations. Input decks were created for each irradiation facility using the data obtained from Section 5.2: sigma-phi reaction rates and their associated errors (described below), and MCNP flux values for each of the 100 energy bins. Input deck structure is described in Appendix A.

The sigma-phi reaction rate error was calculated using the error propagation formula [42] in equation (17).

$$\varepsilon_A = \sqrt{\varepsilon_m{}^2 + \varepsilon_C{}^2 + \varepsilon_\varepsilon{}^2 + \varepsilon_t{}^2} \tag{17}$$

The error of the activity ε_A is the sum of the squares of the errors of the foil masses (ε_m), counts (ε_C), detector efficiency (ε_ε) and counting time (ε_t). The mass error was simply ±.00005 g (the limits of the scale used to weigh the foils). The other errors were determined by the Gammavision software.

In this study, the 100 energy bins of flux output from MCNP are compared to the sigma-phi reaction rates obtained from the activation foils. The MCNP flux outputs are turned into theoretical sigma-phi reaction rates by STAY'SL by multiplying each flux value by each activation reaction's cross section value at each energy level, which are then summed to obtain a total sigma-phi value for each theoretical reaction. These theoretical sigma-phi values are then compared to the experimental sigma-phi values to determine each reaction's chi-squared (χ^2).

Initial STAY'SL runs were performed using all measured reactions. After each initial deck run, outliers were selectively removed (explained further in Chapter 6) to optimize the value of chi-squared. Once an optimized value of chi-squared was obtained, the adjusted LEU spectra were then compared to the HEU spectra (Sections 6.3 and 6.4).

5.4 Axial Flux Determination in the Central Thimble

Two aluminum-gold wire samples (0.12 mass percent of gold) were irradiated in the central thimble; one bare, one cadmium-covered. In order to determine the flux profile of the full axial length of the core, 48 inch long wires were irradiated, covering the axial length from the safety plate to the top of the upper grid plate (Figure 5–5). The wires were encapsulated in 48 inch long, 0.25 inch OD aluminum 6061 pipe that was tapped and sealed with aluminum screws and vacuum grease. The wires were each irradiated separately at 10 kW for 30 minutes. The core was changed to the NORMAL configuration to attempt to make the flux as symmetric as possible in the center of the core.

The average control rod height during the irradiation was 43.75% withdrawn from the core, which is approximately 6.5 inches above the bottom of the fueled region of the core. The control rod heights affect the axial profile as control rods are neutron absorbers; control rods tend to depress the natural cosine shape of flux, pushing the axial peak flux position below the centerline of the fuel. This will be discussed in Section 6.5.

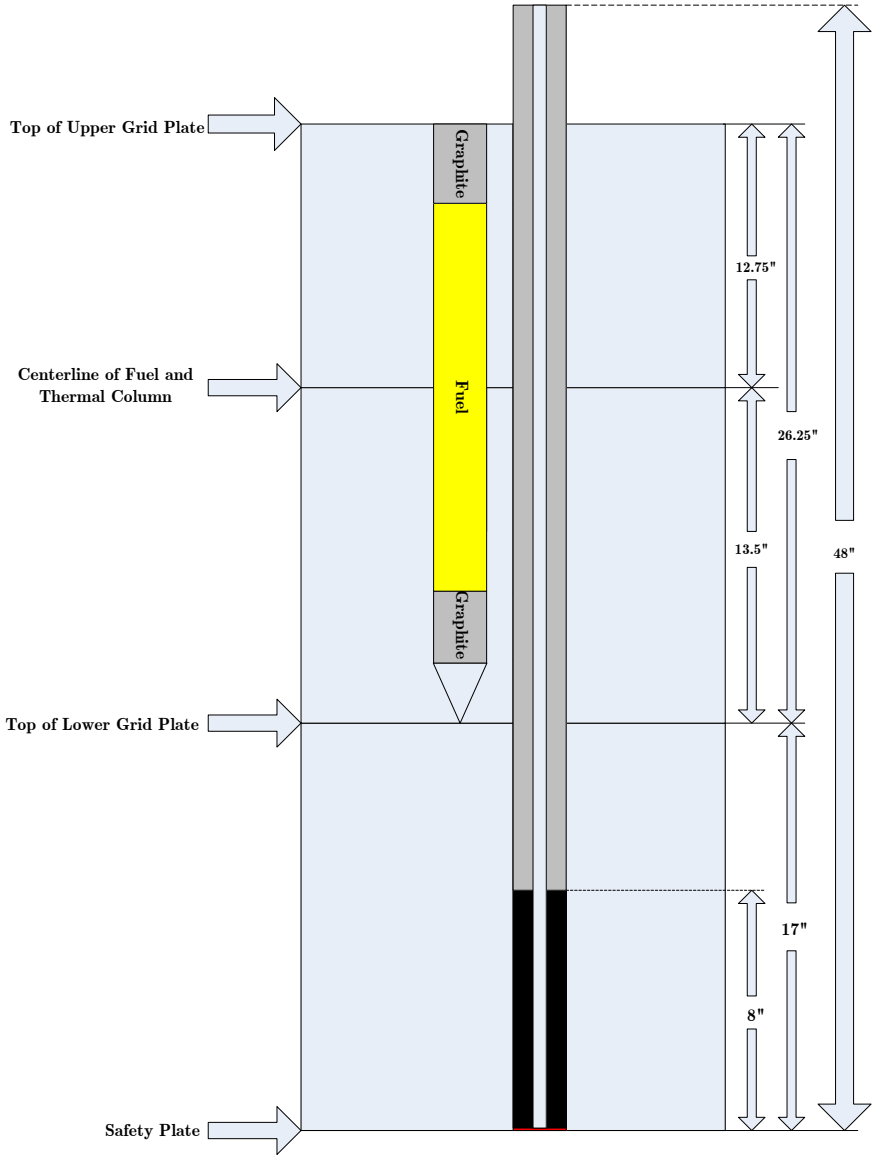

Figure 5–5: Central thimble wire irradiation

The wires were removed from the core after a suitable amount of decay time and taken to a lab to be prepared for counting. Counting preparation involved cutting the wire into small pieces and weighing each individual piece to determine the mass of activated gold in each sample.

The 48 inch long wires were not appreciably activated during the irradiation. Portions of the wires that were not in the core did not activate at all. The 48 inch long wires were reduced to approximately 40 inches; the lower 8 inches of each wire were discarded as they weren't activated enough to produce significant counts above background (due to

being located well below the reactor core). The remaining 40 inch wires were then cut into 50 total pieces each (as seen in Figure 5–6): the top 6 inches and bottom 9 inches were cut into ten 1.5 inch pieces (represented by the blue regions of the central thimble), then the next top and bottom 5 inches were cut into ten 1 inch pieces (represented by the gray regions), and the remaining center of the wire was cut into thirty 0.5 inch pieces (represented by the red region). This provided a more resolved axial flux determination for the fueled region of the reactor core as seen in the central thimble.

The samples were then placed into 0.4 mL polyethylene microcentrifuge tubes and counted on an automated HPGe detector. Fluxes were then calculated in Excel using equation (14). The epithermal flux was determined from the cadmium-covered wire and the total flux was determined from the bare wire.

The thermal flux was determined by first irradiating the cadmium-covered wire and determining the epithermal flux profile using a 6^{th}-order polynomial fit in Excel. Once a profile was determined, a bare wire was irradiated and a total flux profile was determined. The 6^{th}-order polynomial was then used to determine the theoretical epithermal flux at each midpoint of each snippet of the bare wire, which then allowed the theoretical epithermal activity to be subtracted from the total bare wire activity to obtain the thermal flux profile. Thus the thermal flux calculations are dependent upon the epithermal flux calculations.

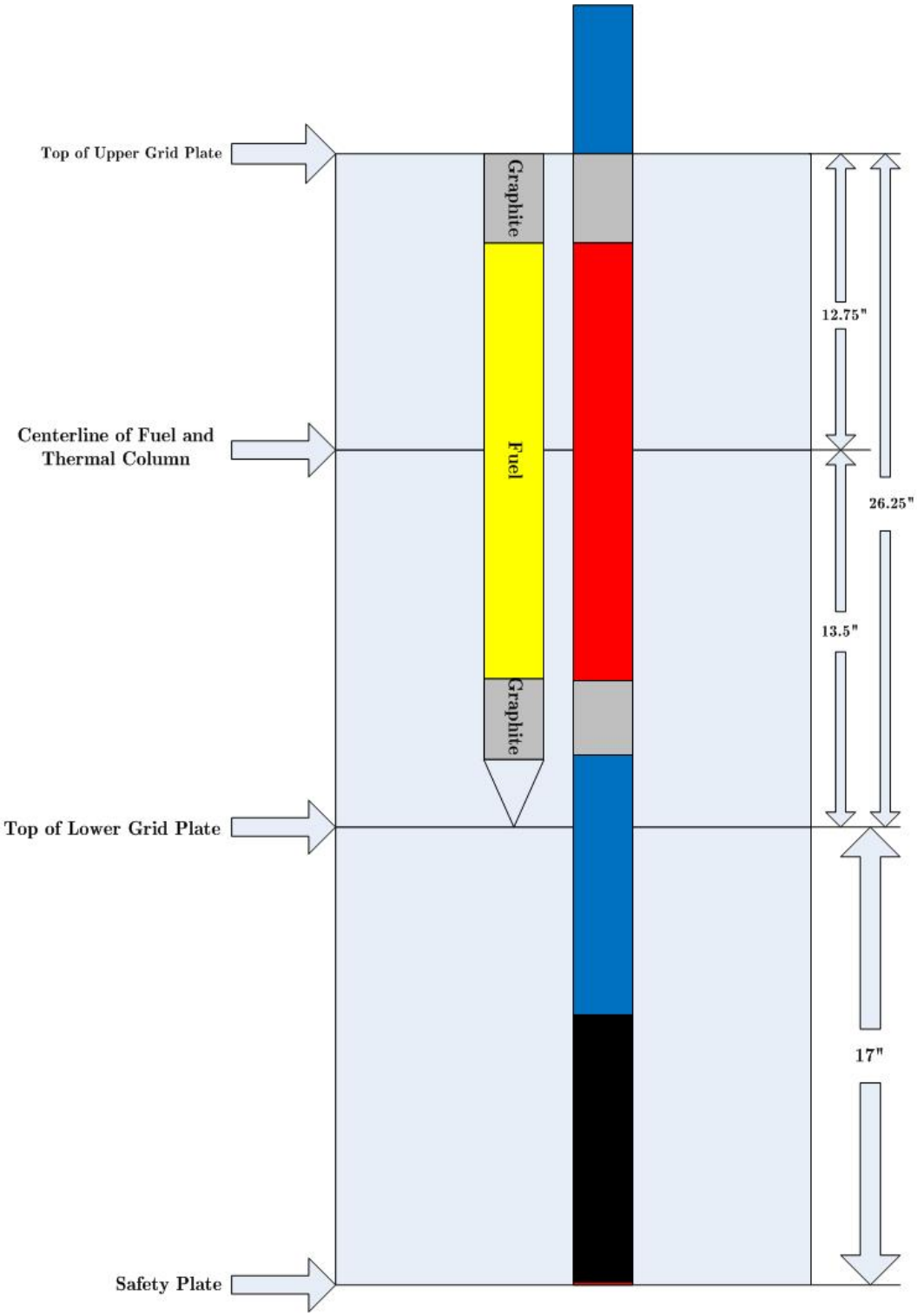

Figure 5–6: Central thimble wire lengths

6. RESULTS AND DISCUSSION

6.1 MCNP Model Comparisons

In this section a presentation and discussion of the HEU and LEU MCNP results are provided for the Lazy Susa, ICIT, CLICIT and Rabbit facilities. In addition, the GRICIT MCNP results are compared between the ICIT and CLICIT core configurations. The thermal column is omitted in this section as it has already been discussed in Chapter 5. It is important to note that the information presented in this section are direct resultants of the MCNP models and do not include any post-simulation analysis from the STAY'SL code. The error was obtained from the MCNP output files (note: error data was unavailable for the HEU Lazy Susan MCNP flux data).

6.1.1 Lazy Susan

Figure 6–1 presents the local neutron spectra in the bottom of the Lazy Susan. The volume over which the neutron spectra were tabulated is one cubic centimeter. The flux has been averaged over all 40 positions since it is assumed that the Lazy Susan rotates around the core during normal operations in order to yield an equal flux in all positions.

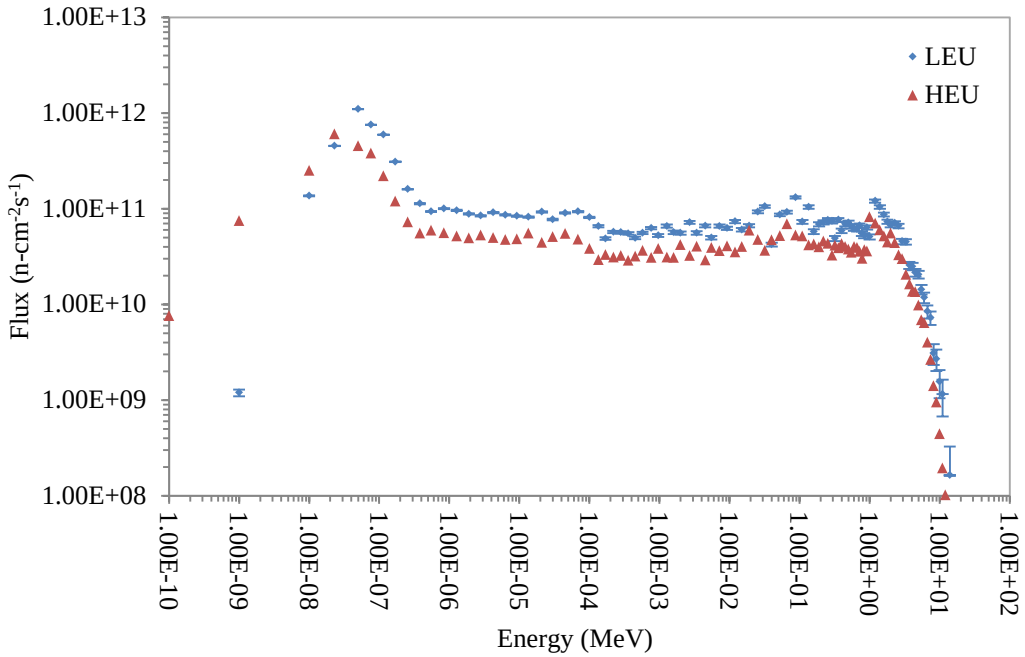

Figure 6–1: Lazy Susan MCNP spectrum in HEU and LEU cores

In Figure 6–1, the HEU core appears to dominate the thermal flux region and the LEU dominates the epithermal and fast flux regions. The HEU core was not as symmetric as the LEU core as can be seen when comparing Figure 5–1 to Figure 4–2, with a significant amount of fuel residing in the G-ring on the west side of the core, and empty water holes on the east side of the core. It is possible that the effects of the empty G-ring water holes would cause more thermalization and epithermal/fast flux depression than the epithermal/fast flux increase caused by adjacent G-ring fuel elements in the HEU model. This would explain why the thermal flux is higher in the HEU model and why the epithermal/fast fluxes are lower compared to the LEU model.

6.1.2 ICIT

Figure 6–2 presents the neutron flux in the irradiation facility which yields the highest flux for a prescribed power within the OSTR.

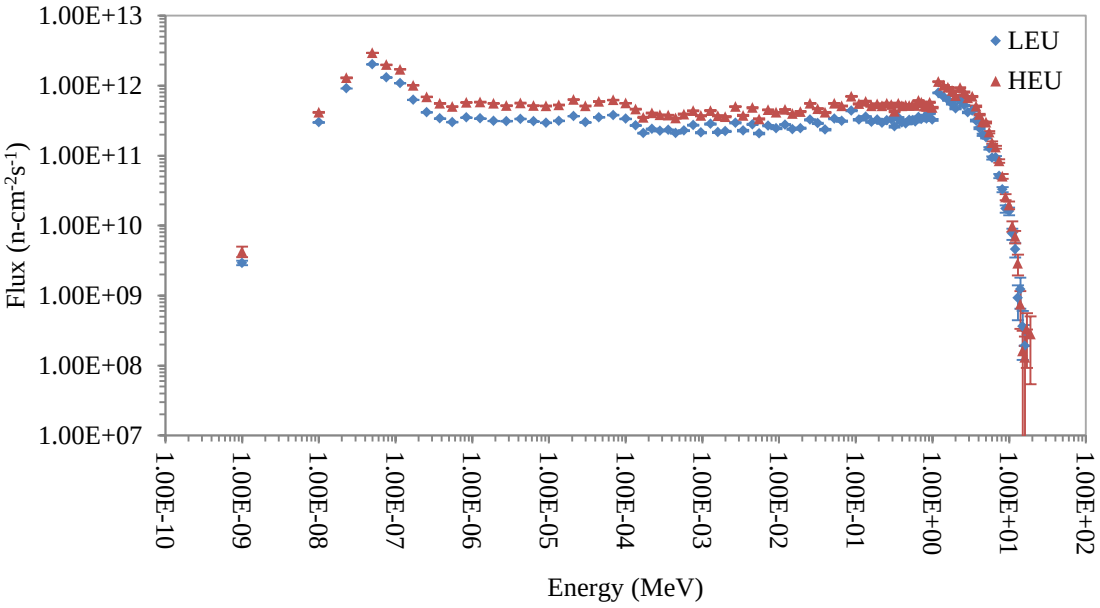

Figure 6–2: ICIT MCNP spectrum in HEU and LEU cores

Both core configurations have a similar spectral shape. From Figure 6–2 the fast spectrum appears to be similar in both core configurations; however the LEU flux values are, in general, consistently lower throughout the entire spectrum. This is likely due to the increase in ^{238}U loading in the LEU core. ^{238}U has a higher affinity for neutron resonance

absorption; therefore as neutrons are moderated in the LEU core, more neutrons will be absorbed in the fuel region with an increase in ^{238}U, causing epithermal flux to decrease.

6.1.3 CLICIT

Figure 6–3 displays the neutron flux within the CLICIT facility for both cores.

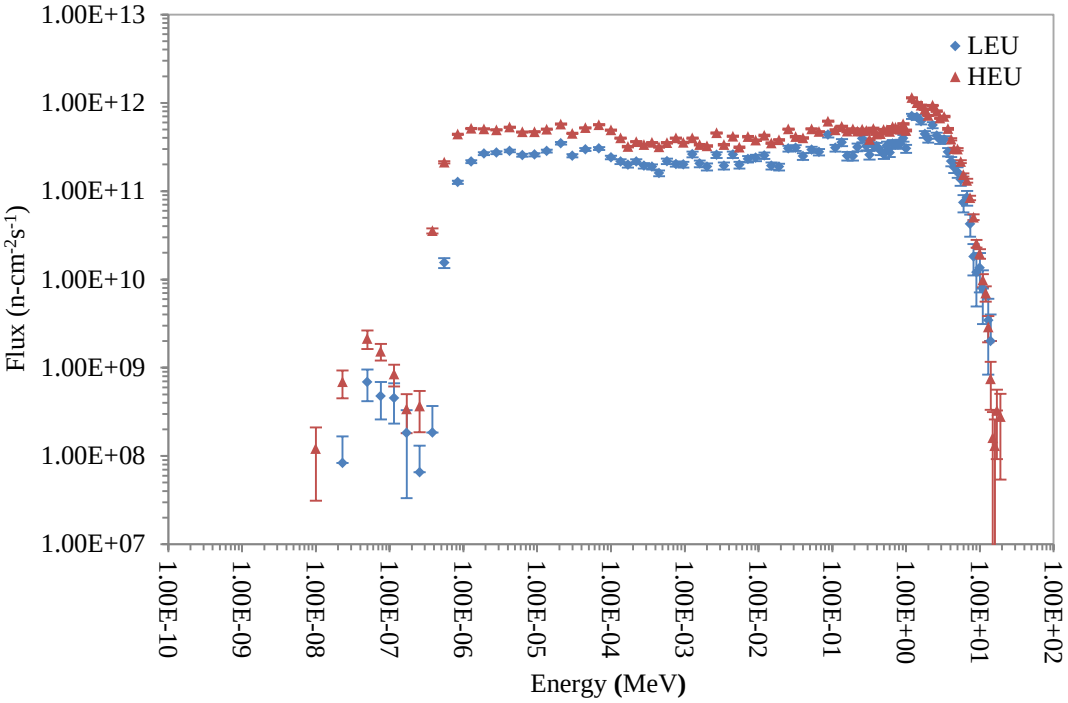

Figure 6–3: CLICIT MCNP spectrum in HEU and LEU cores

The CLICIT experiences reduced flux in the LEU core, for similar reasons as the ICIT model (increased loading of resonance absorbent ^{238}U). The epithermal and fast flux values are very similar to the ICIT, which is consistent with their identical core position; however the cadmium cutoff is evident as the flux decreases by orders of magnitude below 1E-6 MeV. There is still a Maxwellian distribution of thermal neutrons present in the CLICIT, but at many orders of magnitude below the unlined ICIT.

6.1.4 Rabbit

Figure 6–4 presents the neutron flux within the Rabbit irradiation facility for both cores.

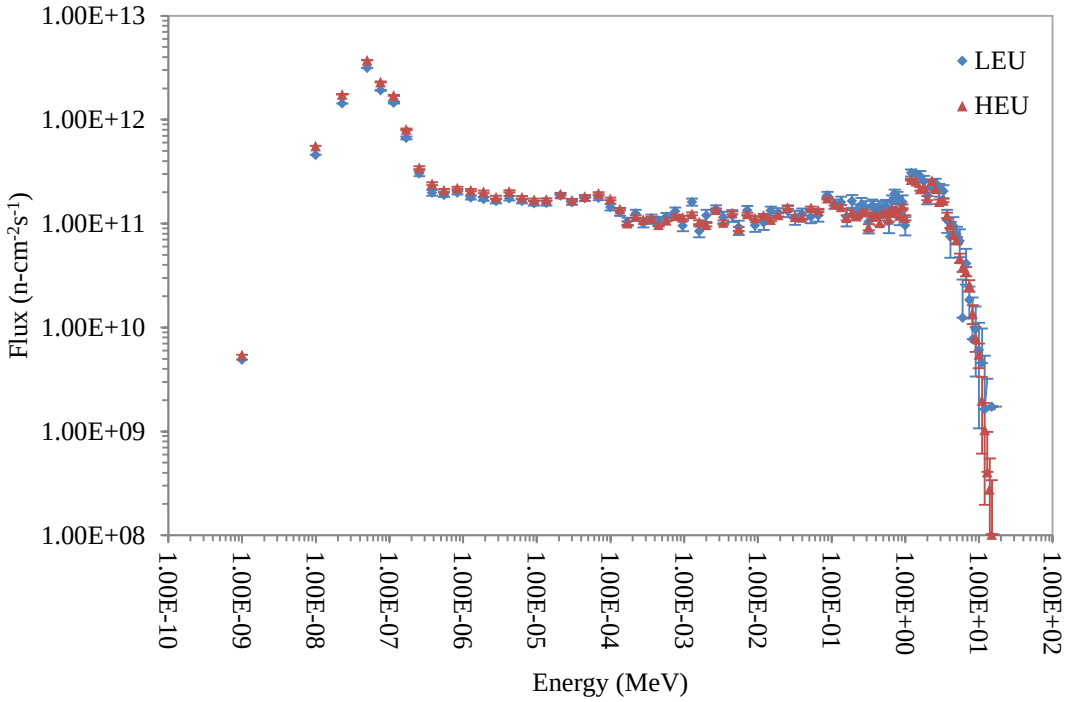

Figure 6–4: Rabbit MCNP spectrum in HEU and LEU cores

From Figure 6–4, the fluxes in both core configurations appear to be nearly identical. Although the increased loading of ^{238}U should decrease the epithermal flux in the Rabbit due to resonance absorptions in the ^{238}U, another change in the model may counterbalance this effect. In the 2005 model, the G1 and G3 core positions on either side of the Rabbit were modeled as graphite. The current core configuration incorporates water-filled voids in these positions. It is possible that the thermalizing effects of the surrounding water holes may have countered the flux depression due to the increased ^{238}U loading.

The thermal flux in the Rabbit is much higher than the epithermal and fast flux. This is due to its location at the core periphery. Fast flux is highest at the center of a fuel element and is highest at the center of the core. Neutrons at the edge of the core have traveled

through moderator as well as fuel and become more thermalized through scattering interactions. The core is also surrounded by a graphite reflector, the purpose of which is to improve neutron efficiency by reflecting neutrons back into the core, which increases thermal flux on the core periphery.

6.1.5 GRICIT

The GRICIT facility was not available during the previous characterization study. Since this facility has never been characterized, it was desirable to see if the core configuration affected the spectra in the GRICIT. The MCNP model was compared between the ICIT and CLICIT core configurations in the peak axial flux position in the GRICIT as seen in Figure 6–5.

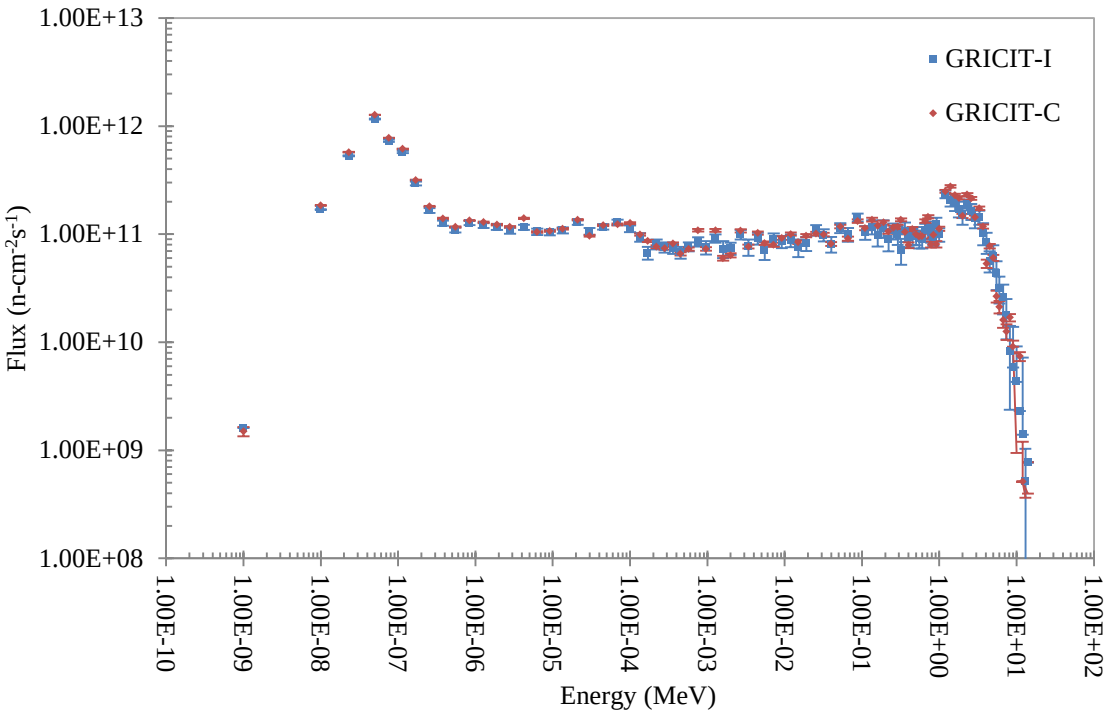

Figure 6–5: GRICIT MCNP spectrum compared between core configurations

6.2 Chi-Squared Optimization (Chauvenet's Criterion)

This section displays all of the sigma-phi reaction rates (and their respective errors) that were input into STAY'SL decks, as well as the final optimized chi-squared values for the reactions used to adjust the spectra.

For each irradiation facility, all reactions were input into STAY'SL decks and initial runs were performed to determine the initial reduced chi-squared value of all reactions. After each initial STAY'SL run, the chi-squared was then optimized by removing outlier reactions and re-running the deck in order to obtain a minimized reduced chi-squared value between 0.3 and 2.0 (as explained in Section 3.4). Individual reactions were determined to be outlier reactions using Chauvenet's criterion for down-selection [43]. The criterion specifies that all points that fall within a band around the mean value should be retained. First, the mean and the standard deviation S of all values are calculated. Then the maximum deviation d_{max} (maximum value from the mean) is calculated. The ratio of d_{max}/S is then multiplied by the value in Table 6-1 corresponding to the number of values (in this case, individual chi-squared values). For the sake of conservatism, the ratio for n equal to 15 readings was used for all facilities, despite most facilities' characterization studies having utilized less than 15 reactions.

Table 6-1: Chauvenet's criterion for down-selection

Number of Readings, *n*	Ratio of maximum acceptable deviation to standard deviation, d_{max}/σ
3	1.38
4	1.54
5	1.65
6	1.73
7	1.80
10	1.96
15	2.13
25	2.33
50	2.57
100	2.81

If an individual reaction's chi-squared value is above the Chauvenet criterion, it is then eligible to be removed. Ideally no reactions would be removed, but in this study, foils have to be removed in order to reduce the chi-squared value to between 0.3 and 2.0. In the event that a reaction is deemed an outlier and is removed, it was ensured that the remaining foils were still able to adequately cover the full energy spectrum.

The first column of data displayed in the following chi-squared tables (labeled "all reactions") is from the initial STAY'SL runs utilizing all available reactions, with an AK1 normalization value of 0.0 (for further explanation of what the AK1 value signifies, see Appendix A). Using an initial AK1 value of 0.0 forces STAY'SL to determine an AK1 normalization value for future optimization runs. In some cases, AK1 adjustment was not necessary.

It should be noted that all reactions were bare foil reactions unless denoted with "+ Cd" which indicates that the reaction involved a cadmium-covered foil.

6.2.1 Lazy Susan

Table 6-2 displays the sigma-phi values for each reaction, as well as their respective errors. Due to some miscalculations in the pre-irradiation activity calculations, the bare scandium foil was over-irradiated and had excessive dead time, contributing to its high error. The high error on the Fe-54(n,a) reaction is due to a low amount of counts obtained.

Table 6-2: Sigma-Phi and error calculations for Lazy Susan

Foil	Reaction	Sigma-Phi	Error
Fe	Fe-58(n,g)Fe-59	3.518E-12	15%
	Fe-58(n,g)Fe-59 + Cd	1.605E-13	16%
	Fe-54(n,p)Mn-54	2.898E-13	8%
	Fe-56(n,p)Mn-56	7.395E-14	7%
	Fe-54(n,a)Cr-51	1.075E-13	29%
Al-Au	Al-27(n,a)Na-24	5.067E-16	22%
	Au-197(n,g)Au-198	4.701E-10	21%
	Au-197(n,g)Au-198 + Cd	4.776E-11	10%
Sc	Sc-45(n,g)Sc-46	7.007E-11	74%
	Sc-45(n,g)Sc-46 + Cd	1.037E-12	3%
In	In-115(n,n')In-115	1.531E-13	14%
Ni	Ni-58(n,p)Co-58	7.301E-14	5%
Ti	Ti-46(n,p)Sc-46	8.573E-15	6%
	Ti-47(n,p)Sc-47	1.382E-14	2%
	Ti-48(n,p)Sc-48	1.729E-16	4%

Error! Not a valid bookmark self-reference. displays the chi-squared optimization from an initial value of 21.740 to a final value of 0.823. The Chauvenet value for the initial run was 7.276. Two reactions were determined to exceed this number and were removed. A second STAY'SL run was performed, producing the optimized chi-squared values.

Table 6-3: Chi-squared STAY'SL outputs for Lazy Susan (AK1 = 1.0)

Spectrum	Reaction	χ^2(all reactions)	χ^2(optimized)
Thermal	Fe-58(n,g)Fe-59	-0.695	0.051
	Au-197(n,g)Au-198	2.217	-1.545
	Sc-45(n,g)Sc-46	-0.104	0.030
Epithermal	Fe-58(n,g)Fe-59 + Cd	0.342	0.424
	Au-197(n,g)Au-198 + Cd	6.530	6.283
	Sc-45(n,g)Sc-46 + Cd	-0.967	-1.604
Fast	Fe-54(n,a)Cr-51	3.891	1.546
	Fe-54(n,p)Mn-54	87.722	
	Fe-56(n,p)Mn-56	200.244	
	Al-27(n,a)Na-24	0.262	0.489
	In-115(n,n')In-115	1.156	0.272
	Ni-58(n,p)Co-58	1.298	0.100
	Ti-46(n,p)Sc-46	5.988	-0.697
	Ti-47(n,p)Sc-47	-1.163	1.286
	Ti-48(n,p)Sc-48	-2.360	3.239
Chauvenet = 7.276	Normalized χ^2	21.740	0.823

6.2.2 ICIT

Table 6-4 displays the sigma-phi values for each reaction, as well as their respective errors. The tungsten was slightly over-irradiated, causing a relatively high dead time contribution to its error.

Table 6-4: Sigma-Phi and error calculations for ICIT

Foil	Reaction	Sigma-Phi	Error
Fe	Fe-58(n,g)Fe-59	1.245E-11	3%
	Fe-58(n,g)Fe-59 + Cd	2.184E-12	4%
	Fe-54(n,p)Mn-54	1.371E-12	3%
	Fe-54(n,a)Cr-51	1.857E-14	10%
Al-Au	Al-27(n,a)Na-24	1.059E-14	3%
	Au-197(n,g)Au-198	1.781E-09	2%
	Au-197(n,g)Au-198 + Cd	1.844E-09	17%
W	W-186(n,g)W-187	3.191E-10	26%
	W-186(n,g)W-187 + Cd	1.402E-10	28%
In	In-115(n,n')In-115	2.383E-12	2%
Ni	Ni-58(n,p)Co-58	1.201E-12	2%
Ti	Ti-46(n,p)Sc-46	1.877E-13	4%
	Ti-47(n,p)Sc-47	3.451E-13	3%
	Ti-48(n,p)Sc-48	4.977E-15	4%

Error! Not a valid bookmark self-reference. displays the chi-squared optimization from an initial value of 3.577 to a final value of 1.834. The Chauvenet value for the initial run was 6.760. One reaction was determined to exceed this number and was removed. A second STAY'SL run was performed, producing the optimized chi-squared values.

Table 6-5: Chi-squared STAY'SL outputs for ICIT (AK1 = 2.35)

Spectrum	Reaction	χ^2 (all reactions)	χ^2 (optimized)
Thermal	Fe-58(n,g)Fe-59	2.227	-4.674
	Au-197(n,g)Au-198	6.209	16.248
	W-186(n,g)W-187	1.519	4.056
Epithermal	Fe-58(n,g)Fe-59 + Cd	0.788	0.216
	Au-197(n,g)Au-198 + Cd	2.091	-5.453
	W-186(n,g)W-187 + Cd	-0.114	-0.733
Fast	Al-27(n,a)Na-24	-3.016	6.044
	Fe-54(n,a)Cr-51	3.660	0.060
	Fe-54(n,p)Mn-54	19.568	
	In-115(n,n')In-115	-0.378	2.469
	Ni-58(n,p)Co-58	0.455	6.900
	Ti-46(n,p)Sc-46	3.472	-0.872
	Ti-47(n,p)Sc-47	6.139	-1.134
	Ti-48(n,p)Sc-48	3.880	-1.122
Chauvenet = 6.760	Normalized χ^2	3.577	1.834

6.2.3 CLICIT

Table 6-6 displays the sigma-phi values for each reaction, as well as their respective errors. The Fe-54(n,a) reaction exhibited very few counts, which caused its error to be relatively high. Otherwise, the error was very low for the rest of the CLICIT foils.

Table 6-6: Sigma-Phi and error calculations for CLICIT

Foil	Reaction	Sigma-Phi	Error
Fe	Fe-58(n,g)Fe-59	1.717E-12	5%
	Fe-54(n,p)Mn-54	1.251E-12	2%
	Fe-56(n,p)Mn-56	5.292E-14	3%
	Fe-54(n,a)Cr-51	1.587E-14	45%
Al-Au	Al-27(n,a)Na-24	1.066E-14	2%
	Au-197(n,g)Au-198	1.278E-09	2%
NaCl	Na-23(n,g)Na-24	4.233E-13	10%
In	In-115(n,n')In-115	2.275E-12	2%
Ni	Ni-58(n,p)Co-58	1.137E-12	2%
Ti	Ti-46(n,p)Sc-46	1.788E-13	8%
	Ti-47(n,p)Sc-47	3.196E-13	6%
	Ti-48(n,p)Sc-48	4.719E-15	6%

Table 6-7 displays the chi-squared optimization from an initial value of 39.374 to a final value of 1.573. The Chauvenet value for the initial run was 7.061. Two reactions were determined to exceed this number, but only one reaction (Mn-56) was removed as it is preferential to keep as many data points as possible. A second STAY'SL run was performed, producing the optimized chi-squared values.

Table 6-7: Chi-squared STAY'SL outputs for CLICIT (AK1 = 2.0)

Spectrum	Reaction	χ^2 (all reactions)	χ^2 (optimized)
Thermal	none		
Epithermal	Fe-58(n,g)Fe-59	-0.195	0.429
	Au-197(n,g)Au-198	0.489	1.597
	Na-23(n,g)Na-24	6.041	-0.339
Fast	Fe-54(n,p)Mn-54	2.889	-6.357
	Fe-56(n,p)Mn-56	405.781	
	Fe-54(n,a)Cr-51	0.149	-0.270
	Al-27(n,a)Na-24	11.046	8.409
	In-115(n,n')In-115	-0.029	3.509
	Ni-58(n,p)Co-58	5.032	11.713
	Ti-46(n,p)Sc-46	-0.846	-1.215
	Ti-47(n,p)Sc-47	2.895	-0.949
	Ti-48(n,p)Sc-48	-0.139	-0.800
Chauvenet = 7.061	Normalized χ2	39.374	1.573

6.2.4 Rabbit

Table 6-8 displays the sigma-phi values for each reaction, as well as their respective errors. The Fe-54(n,a) reaction exhibited low counts, which contributed to its high error. Due to an error in pre-irradiation calculations, the molybdenum was over-irradiated, causing high amounts of dead time. After experimental data was collected, it was discovered that molybdenum is not a suitable foil for STAY'SL's purposes, as STAY'SL does not utilize molybdenum cross section information, so this foil was not used during the unfolding process.

Table 6-8: Sigma-Phi and error calculations for Rabbit

Foil	Reaction	Sigma-Phi	Error
Fe	Fe-58(n,g)Fe-59	1.386E-11	6%
	Fe-58(n,g)Fe-59 + Cd	6.369E-13	12%
	Fe-54(n,p)Mn-54	4.494E-13	6%
	Fe-56(n,p)Mn-56	4.982E-15	4%
	Fe-54(n,a)Cr-51	9.883E-15	32%
Al-Au	Al-27(n,a)Na-24	3.054E-15	14%
	Au-197(n,g)Au-198	1.345E-09	13%
	Au-197(n,g)Au-198 + Cd	6.111E-10	7%
Mo	Mo-98(n,g)Mo-99	4.020E-12	27%
	Mo-98(n,g)Mo-99 + Cd	2.917E-12	20%
In	In-115(n,n')In-115	7.668E-13	2%
Ni	Ni-58(n,p)Co-58	4.180E-13	6%
Ti	Ti-46(n,p)Sc-46	4.919E-14	5%
	Ti-47(n,p)Sc-47	8.680E-14	2%
	Ti-48(n,p)Sc-48	1.317E-15	2%

Table 6-9 displays the chi-squared optimization from an initial value of 1.812 to a final value of 1.047. The Chauvenet value for the initial run was 6.175. One reaction was determined to exceed this number (Mn-54) and was subsequently removed. A second STAY'SL run was performed, producing the optimized chi-squared values.

Table 6-9: Chi-squared STAY'SL outputs for Rabbit (AK1 = 0.0)

Spectrum	Reaction	χ^2(all reactions)	χ^2 (optimized)
Thermal	Fe-58(n,g)Fe-59	4.896	4.963
	Au-197(n,g)Au-198	1.678	1.593
Epithermal	Fe-58(n,g)Fe-59 + Cd	0.005	0.008
	Au-197(n,g)Au-198 + Cd	-1.349	-1.310
Fast	Fe-54(n,p)Mn-54	10.563	
	Fe-56(n,p)Mn-56	-0.064	-0.225
	Fe-54(n,a)Cr-51	3.586	3.652
	Al-27(n,a)Na-24	2.299	2.261
	In-115(n,n')In-115	-0.195	0.052
	Ni-58(n,p)Co-58	0.418	0.110
	Ti-46(n,p)Sc-46	0.022	-0.005
	Ti-47(n,p)Sc-47	-0.228	0.348
	Ti-48(n,p)Sc-48	0.114	0.068
Chauvenet = 6.175	Normalized χ2	1.812	1.047

6.2.5 GRICIT

Table 6-10 displays the sigma-phi values for each reaction, as well as their respective errors. The Fe-54(n,a) reaction exhibited low counts, which contributed to its relatively large error.

Table 6-10: Sigma-Phi and error calculations for GRICIT

Foil	Reaction	GRICIT-C		GRICIT-I	
		Sigma-Phi	Error	Sigma-Phi	Error
Fe	Fe-58(n,g)Fe-59	7.034E-12	13%	6.976E-12	5%
	Fe-58(n,g)Fe-59 + Cd	5.696E-13	11%	6.397E-13	7%
	Fe-54(n,p)Mn-54	8.339E-13	13%	4.207E-13	4%
	Fe-56(n,p)Mn-56	1.542E-13	13%	5.815E-15	5%
	Fe-54(n,a)Cr-51	1.598E-14	25%	4.719E-15	16%
Al-Au	Al-27(n,a)Na-24	3.510E-15	14%	3.803E-15	9%
	Au-197(n,g)Au-198	9.834E-10	14%	1.070E-09	9%
	Au-197(n,g)Au-198 + Cd	6.085E-10	18%	6.264E-10	9%
Lu-Al	Lu-175(n,g)Lu-176m			9.464E-12	2%
	Lu-176(n,g)Lu-177			5.339E-10	2%
	Lu-176(n,g)Lu-177 + Cd			4.397E-10	2%
Sc	Sc-45(n,g)Sc-46	1.010E-10	19%		
	Sc-45(n,g)Sc-46 + Cd	3.962E-12	9%		
In	In-115(n,n')In-115	1.090E-12	9%	9.920E-13	13%
Ni	Ni-58(n,p)Co-58	4.992E-13	21%	3.636E-13	2%
Ti	Ti-46(n,p)Sc-46	5.357E-14	6%	5.837E-14	7%
	Ti-47(n,p)Sc-47	9.476E-14	6%	9.998E-14	6%
	Ti-48(n,p)Sc-48	1.142E-15	6%	1.519E-15	6%

Table 6-11 displays the chi-squared optimization for each core configuration, from an initial value of 6.293 to a final value of 1.466 for the CLICIT configuration, and an initial value of 30.761 to a final value of 1.008 for the ICIT configuration. A Chauvenet value of 7.551 was calculated in the GRICIT-C and was used for conservatism (it was only 5.534 in the GRICIT-I). Three reactions were determined to exceed this number in the GRICIT-C, but only two reactions (Mn-54 and Mn-56) were removed. Seven reactions were determined to exceed this number in the GRICIT-I, but only three reactions (Lu-176m, Lu-177 and Mn-54) were removed. The skewed Lu reactions indicate that something was wrong with the bare lutetium foil. A second STAY'SL run was performed for each core configuration, producing the optimized chi-squared values.

Table 6-11: Chi-squared STAY'SL outputs for GRICIT (AK1 = 0.0)

Spectrum	Reaction	GRICIT-C		GRICIT-I	
		χ^2(all reactions)	χ^2 (optimized)	χ^2(all reactions)	χ^2 (optimized)
Thermal	Fe-58(n,g)Fe-59	4.600	4.708	147.545	1.479
	Au-197(n,g)Au-198	0.000	0.000	17.549	0.787
	Lu-175(n,g)Lu-176m			117.587	
	Lu-176(n,g)Lu-177			85.804	
	Sc-45(n,g)Sc-46	-0.600	-0.648		
Epithermal	Fe-58(n,g)Fe-59 + Cd	0.015	0.009	6.509	0.134
	Au-197(n,g)Au-198 + Cd	-0.217	-0.179	0.155	-0.205
	Lu-176(n,g)Lu-177 + Cd			52.327	-0.322
	Sc-45(n,g)Sc-46 + Cd	0.914	0.864	52.327	-0.322
Fast	Fe-54(n,p)Mn-54	16.191		24.234	
	Fe-56(n,p)Mn-56	55.524		2.815	-3.137
	Fe-54(n,a)Cr-51	9.348	9.505	0.979	-0.416
	Al-27(n,a)Na-24	-0.003	0.010	-1.089	6.459
	In-115(n,n')In-115	1.697	2.470	4.055	-0.055
	Ni-58(n,p)Co-58	-0.105	-0.034	-4.124	8.074
	Ti-46(n,p)Sc-46	-0.105	0.077	2.254	-1.052
	Ti-47(n,p)Sc-47	-0.432	-0.159	5.419	-0.750
	Ti-48(n,p)Sc-48	1.279	0.972	-0.604	1.098
Chauvenet = 7.551	Normalized χ^2	6.293	1.466	30.761	1.008

6.2.6 Thermal Column

Table 6-12 displays the sigma-phi values for each reaction, as well as their respective errors. The samples had fixed irradiation times because of the reactor's operation schedule, so the bare scandium foil (which was irradiated for 5.5 hours along with the bare iron, bare aluminum-gold and bare indium) was over-irradiated, causing a large amount of dead time on the detector and thus a large amount of total error.

Table 6-12: Sigma-Phi and error calculations for TC

Foil	Reaction	Sigma-Phi	Error
Fe	Fe-58(n,g)Fe-59	1.281E-13	16%
	Fe-58(n,g)Fe-59 + Cd	6.140E-16	11%
	Fe-54(n,p)Mn-54	6.761E-15	15%
	Fe-56(n,p)Mn-56	2.844E-15	15%
Al-Au	Al-27(n,a)Na-24	1.195E-18	10%
	Au-197(n,g)Au-198	6.474E-12	2%
	Au-197(n,g)Au-198 + Cd	5.002E-13	3%
Sc	Sc-45(n,g)Sc-46	2.051E-12	70%
	Sc-45(n,g)Sc-46 + Cd	5.758E-15	10%
In	In-115(n,n')In-115	1.445E-16	13%

Table 6-13 displays the chi-squared optimization from an initial value of 15.759 to a final value of 1.478. The Chauvenet value for the initial run was 3.994. Six reactions were determined to exceed this number, but only the two largest outliers (Mn-54 and Mn-56) were removed. A second STAY'SL run was performed, producing the optimized chi-squared values.

Table 6-13: Chi-squared STAY'SL outputs for TC (AK1 = 2.0)

Spectrum	Reaction	χ^2(all reactions)	χ^2 (optimized)
Thermal	Fe-58(n,g)Fe-59	7.526	-8.054
	Au-197(n,g)Au-198	0.104	14.356
	Sc-45(n,g)Sc-46	0.090	-0.650
Epi-Thermal	Fe-58(n,g)Fe-59 + Cd	1.769	-3.509
	Au-197(n,g)Au-198 + Cd	3.979	-2.576
	Sc-45(n,g)Sc-46 + Cd	15.374	8.502
Fast	In-115(n,n')In-115	13.591	0.140
	Fe-54(n,p)Mn-54	43.776	
	Fe-56(n,p)Mn-56	44.276	
	Al-27(n,a)Na-24	11.342	2.139
Chauvenet = 3.994	Normalized χ2	15.759	1.478

6.3 Comparison of Adjusted Spectra of LEU to HEU

This section contains comparisons of the HEU and LEU flux spectra outputs obtained after applying the MCNP models' spectral results into the STAY'SL unfolding code. The graphs of the full spectra in both the HEU and LEU cores are presented over the entire energy spectrum as well as within their prescribed energy region, so as to provide sufficient detail for future use ((a) denotes the full spectrum from 1E-10 MeV to 20 MeV, (b) denotes thermal spectrum, (c) denotes epithermal spectrum and (d) denotes the fast spectrum).

It should be noted that the MCNP plots in this section are different than the MCNP plots in Section 6.1. This is because the MCNP data in this section is from the STAY'SL output files, which have adjusted the MCNP data via AK1 normalization and Maxwellian adjustment (see Appendix A). Table 6-14 summarizes the differences in AK1 normalization between the HEU and LEU studies.

Table 6-14: Comparison of AK1 values between HEU and LEU studies

Irradiation Facility	AK1 (2005 study)	AK1 (current study)
Lazy Susan	0.689	1.0
ICIT	1.1047	2.35
CLICIT	0.986	2.0
Rabbit	0.871	1.0484

STAY'SL output decks produce differential fluxes for each energy bin. For the sake of comparison between the HEU and LEU studies, the differential fluxes were converted to energy-independent fluxes. Each facilities' LEU STAY'SL-adjusted energy-independent flux values are presented in tabular form in Appendix B. STAY'SL also produces results in units of flux per unit lethargy; these values have been reproduced in tabular form in Appendix C.

6.3.1 Lazy Susan

The full STAY'SL-adjusted spectrum can be seen in Figure 6–6a.The STAY'SL-adjusted thermal spectrum indicates that the LEU thermal flux is slightly lower than the HEU thermal flux below 1E-8 MeV (Figure 6–6b). This is likely due to the increased loading o ^{238}U, which hardens the thermal spectrum. Both the HEU and LEU MCNP models vastly over-estimated the epithermal flux and STAY'SL has adjusted both spectra accordingly. The STAY'SL-adjusted epithermal spectra above 1E-6 MeV and below 1E-3 MeV indicates that MCNP vastly over-estimated the epithermal flux but is accurate from 1E-3 MeV to approximately 1 MeV (Figure 6–6c). This is likely due to the assumption of fresh fuel in the MCNP model, when in actually both cores have experienced significant amounts of burnup which result in increased amounts of resonance absorbers. The STAY'SL-adjusted fast spectra indicate that the LEU MCNP model slightly over-estimated the fast flux (Figure 6–6d).

The AK1 value for the 2005 model was 0.689; meaning that the input fluxes were all multiplied by 0.689, which would lower the HEU MCNP data below the LEU MCNP data, despite the initial MCNP model indicating that fast flux was much higher in the HEU core. The activities and subsequent STAY'SL calculations indicate that the fast flux is actually slightly higher in the LEU core. This may be due to the ages of the different cores at the time of irradiation. The HEU study was performed approximately 30 years into its core life, whereas the LEU study was performed approximately 4 years into its core life. As fuel gets further into its core lifetime, ^{238}U is converted into ^{239}Pu, which causes the spectrum to shift (Figure 3–2). The HEU core likely had significantly more ^{239}Pu than the LEU core currently has.

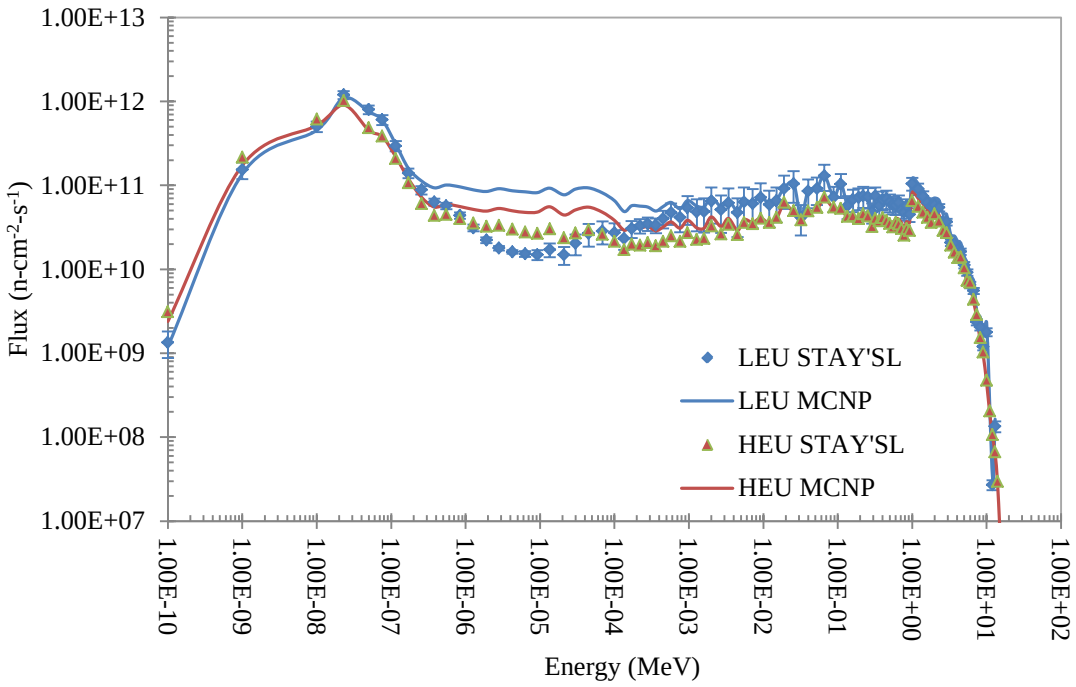
1.00E+13
1.00E+12
1.00E+11
1.00E+10
1.00E+09
1.00E+08
1.00E+07
Flux (n-cm-2-s-1)
1.00E-10
1.00E-09
1.00E-08
1.00E-07
1.00E-06
1.00E-05
1.00E-04
1.00E-03
1.00E-02
1.00E-01
1.00E+00
1.00E+01
1.00E+02
Energy (MeV)
LEU STAY'SL
LEU MCNP
HEU STAY'SL
HEU MCNP

(a)

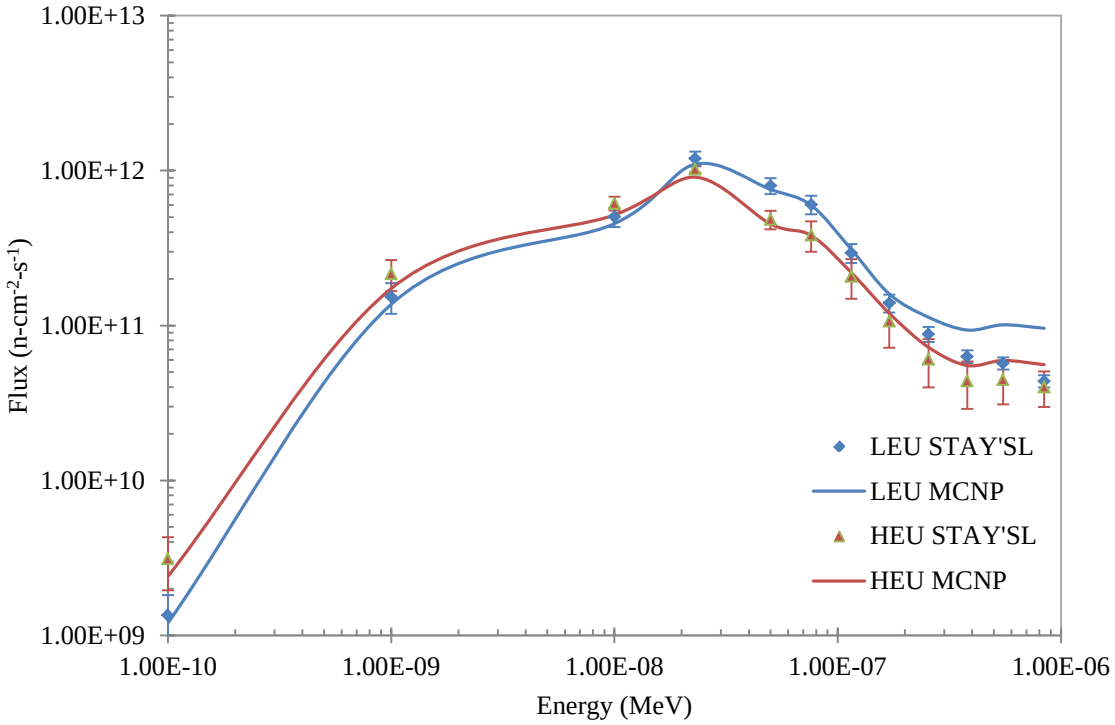
1.00E+13
1.00E+12
1.00E+11
1.00E+10
1.00E+09
Flux (n-cm-2-s-1)
1.00E-10
1.00E-09
1.00E-08
1.00E-07
1.00E-06
Energy (MeV)
LEU STAY'SL
LEU MCNP
HEU STAY'SL
HEU MCNP

(b)

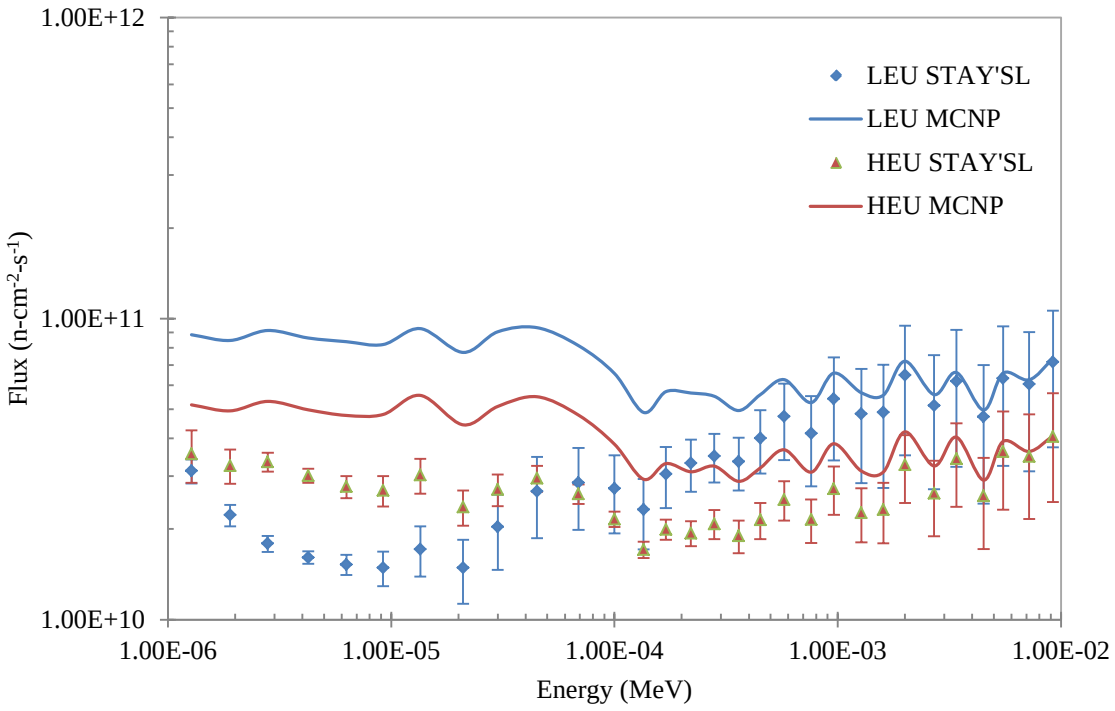

(c)

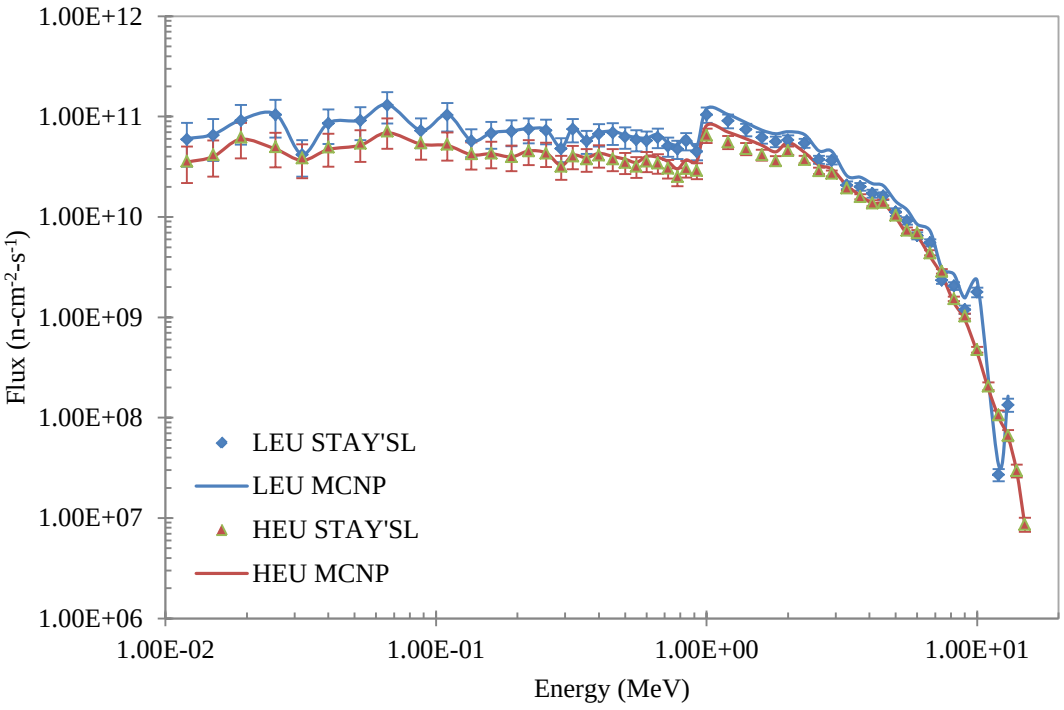

(d)

Figure 6–6 (a through d): Final Lazy Susan Adjusted Flux Spectra

6.3.2 ICIT

The full STAY'SL-adjusted spectrum can be seen in Figure 6–7a. The STAY'SL-adjusted thermal spectrum indicates that the LEU thermal flux is slightly lower than the HEU thermal flux below 1E-8 MeV (Figure 6–7b), similar to the Lazy Susan. The STAY'SL-adjusted epithermal spectra indicates that the LEU epithermal flux is lower than the HEU epithermal flux up to approximately 1E-4 MeV, at which point the LEU epithermal flux is higher than the HEU epithermal flux. MCNP vastly over-estimated the epithermal flux less than 1E-4 MeV but is accurate from 1E-4 MeV to approximately 1 MeV (Figure 6–7c). The STAY'SL-adjusted fast spectrum indicates that the LEU MCNP model slightly over-estimated the fast flux (Figure 6–7d).

In order to fit the LEU activation data to the MCNP modeled fluxes, an AK1 normalization factor of 2.35 was used, compared to the 1.1047 factor used in the HEU study. This is why the LEU MCNP data is higher than the HEU MCNP data (as opposed to the indicated predictions in Section 6.1.2).

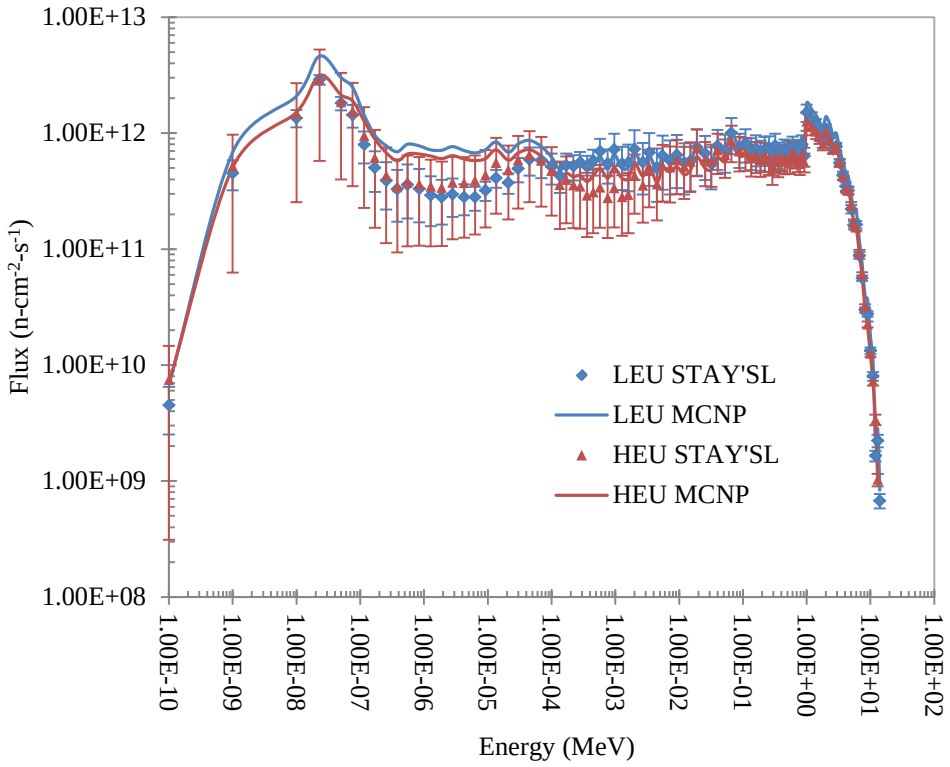
1.00E+13
1.00E+12
1.00E+11
1.00E+10
1.00E+09
1.00E+08
Flux (n-cm-2-s-1)
1.00E-10
1.00E-09
1.00E-08
1.00E-07
1.00E-06
1.00E-05
1.00E-04
1.00E-03
1.00E-02
1.00E-01
1.00E+00
1.00E+01
1.00E+02
Energy (MeV)
LEU STAY'SL
LEU MCNP
HEU STAY'SL
HEU MCNP

(a)

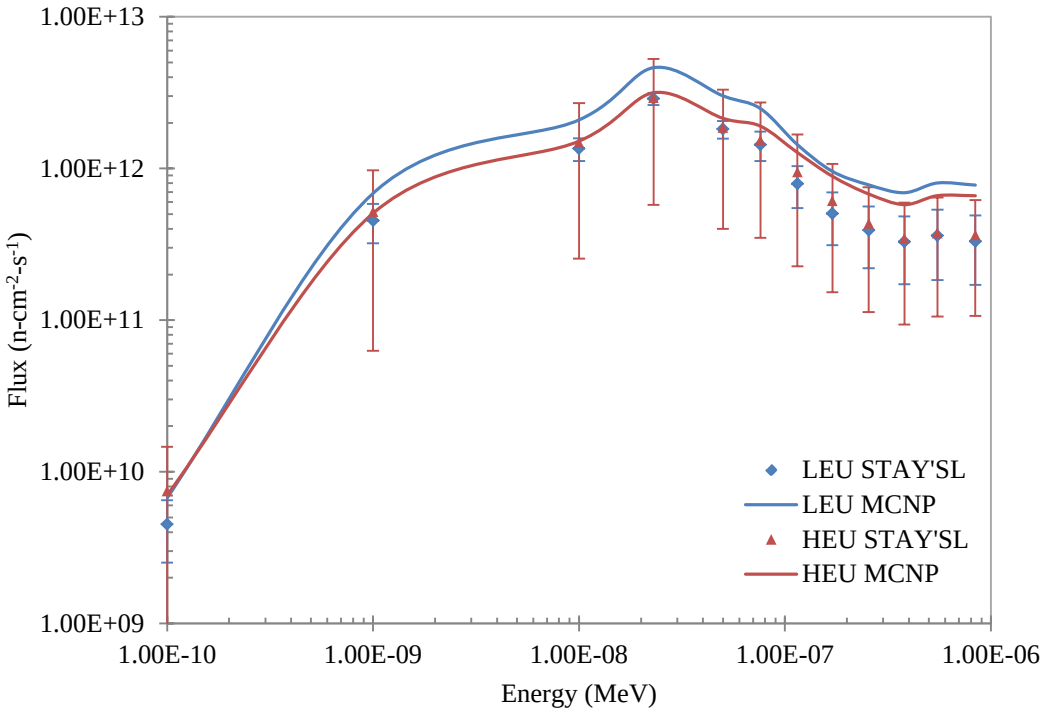
1.00E+13
1.00E+12
1.00E+11
1.00E+10
1.00E+09
Flux (n-cm-2-s-1)
1.00E-10
1.00E-09
1.00E-08
1.00E-07
1.00E-06
Energy (MeV)
LEU STAY'SL
LEU MCNP
HEU STAY'SL
HEU MCNP

(b)

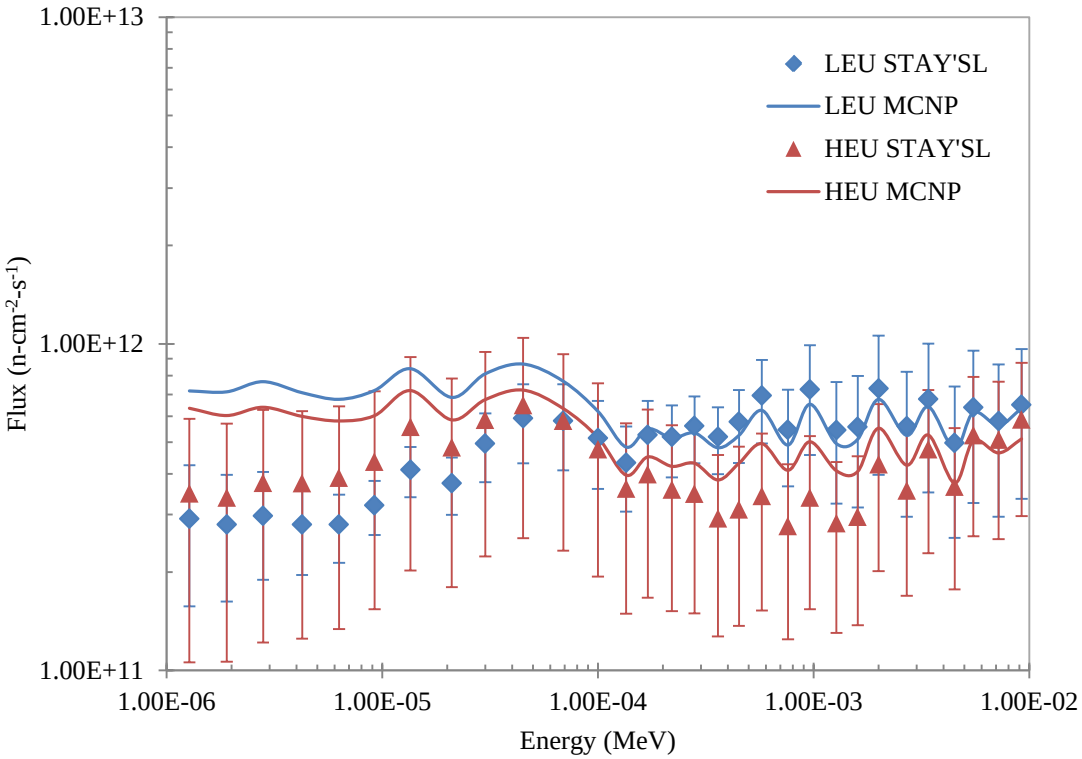

(c)

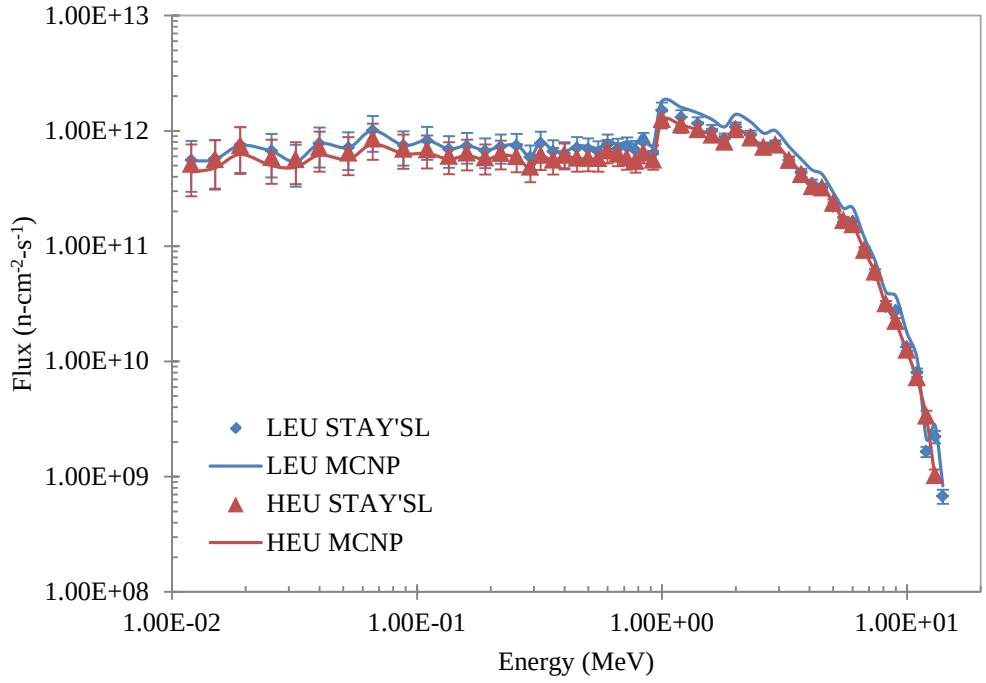

(d)

Figure 6–7 (a through d): Final ICIT Adjusted Flux Spectra

6.3.3 CLICIT

The full STAY'SL-adjusted spectrum can be seen in Figure 6–8a. The STAY'SL-adjusted thermal spectrum indicates that the LEU thermal flux is on par with the HEU thermal flux below 1E-7 (Figure 6–8b). The LEU spectra appear to mimic the shape of the HEU spectra yet is shifted slightly to the right. This is likely due to the core age and erbium content. Due to the large amount of uranium loaded at the beginning of core life and the desired lifetime of the fuel, both HEU and LEU fuels were loaded with a percentage of erbium poison to increase the negative fuel temperature coefficient of the fuel. The LEU core is only 4 years old and should still have most of its erbium poison, whereas the HEU core was 30 years old and likely had less erbium poison remaining.

The STAY'SL-adjusted epithermal spectra indicates that the LEU epithermal flux is lower than the HEU epithermal flux up to approximately 1E-4 MeV, at which point the LEU epithermal flux is higher than the HEU epithermal flux. MCNP over-estimated the epithermal flux less than 1E-4 MeV but then over-estimated the epithermal flux from 1E-4 MeV to approximately 0.1 MeV (Figure 6–8c). The STAY'SL-adjusted fast spectrum indicates that the LEU MCNP model is accurate as the model falls within the STAY'SL error (Figure 6–8d).

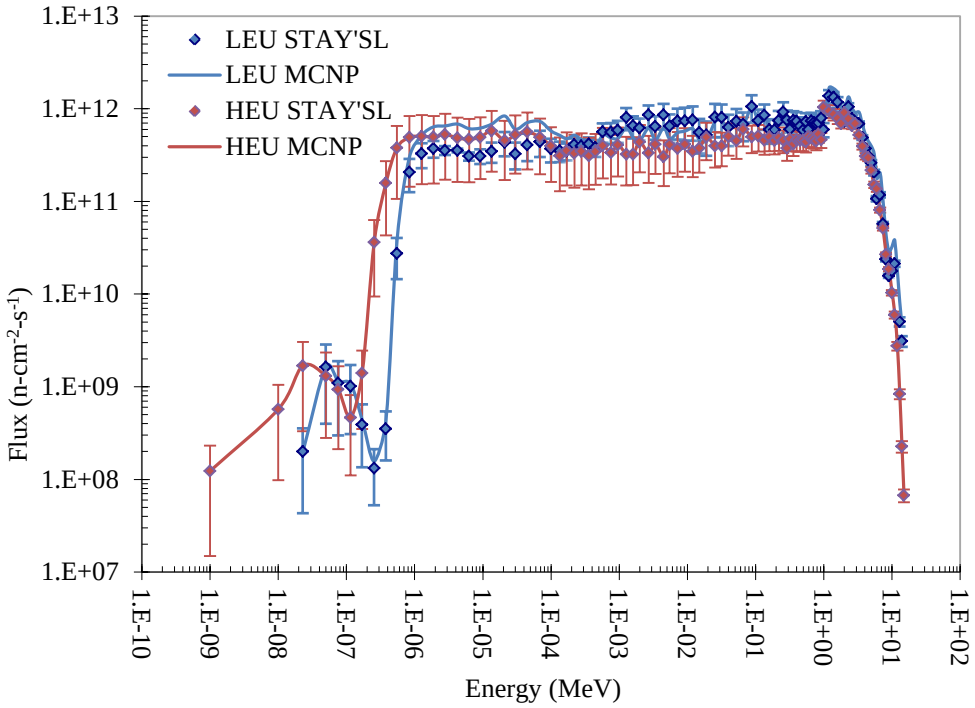
LEU STAY'SL
LEU MCNP
HEU STAY'SL
HEU MCNP
Flux (n-cm-2-s-1)
1.E+13
1.E+12
1.E+11
1.E+10
1.E+09
1.E+08
1.E+07
1.E-10
1.E-09
1.E-08
1.E-07
1.E-06
1.E-05
1.E-04
1.E-03
1.E-02
1.E-01
1.E+00
1.E+01
1.E+02
Energy (MeV)

(a)

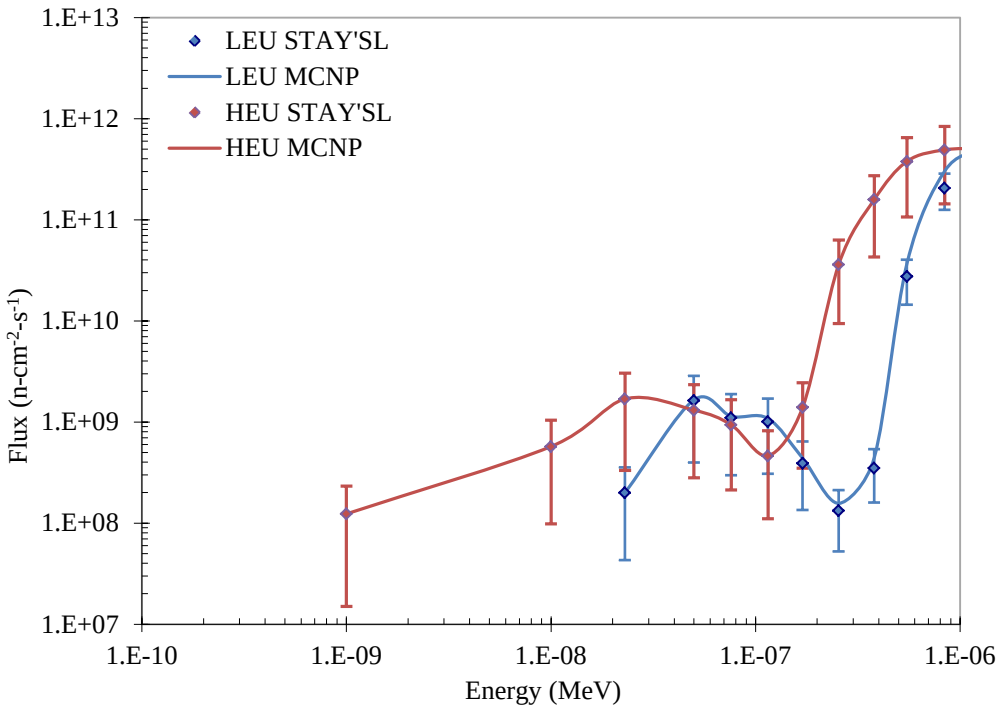
LEU STAY'SL
LEU MCNP
HEU STAY'SL
HEU MCNP
Flux (n-cm-2-s-1)
1.E+13
1.E+12
1.E+11
1.E+10
1.E+09
1.E+08
1.E+07
1.E-10
1.E-09
1.E-08
1.E-07
1.E-06
Energy (MeV)

(b)

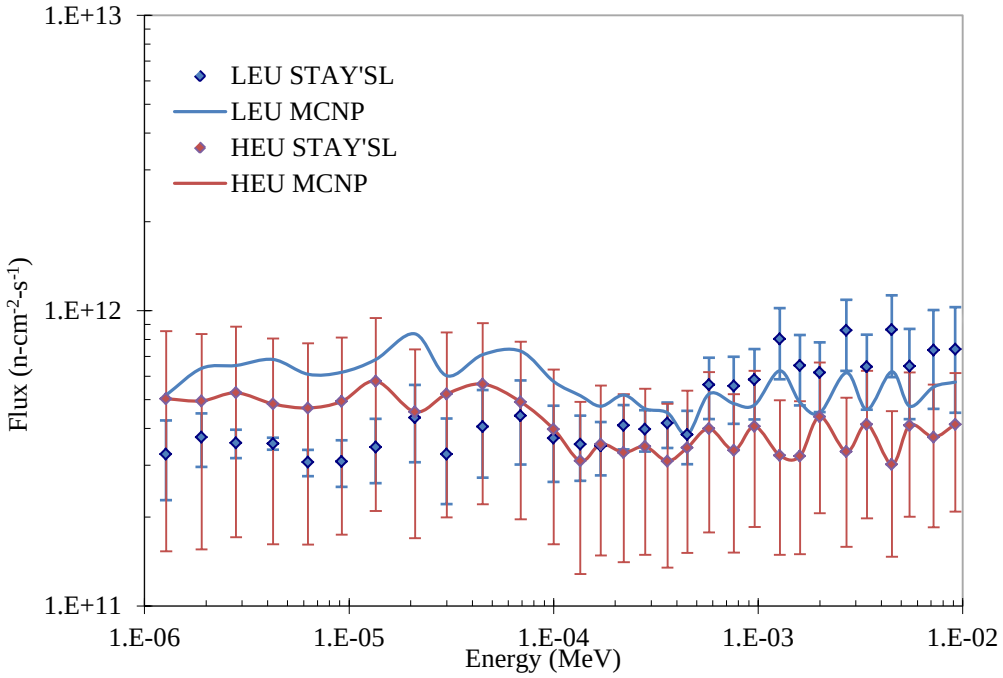

(c)

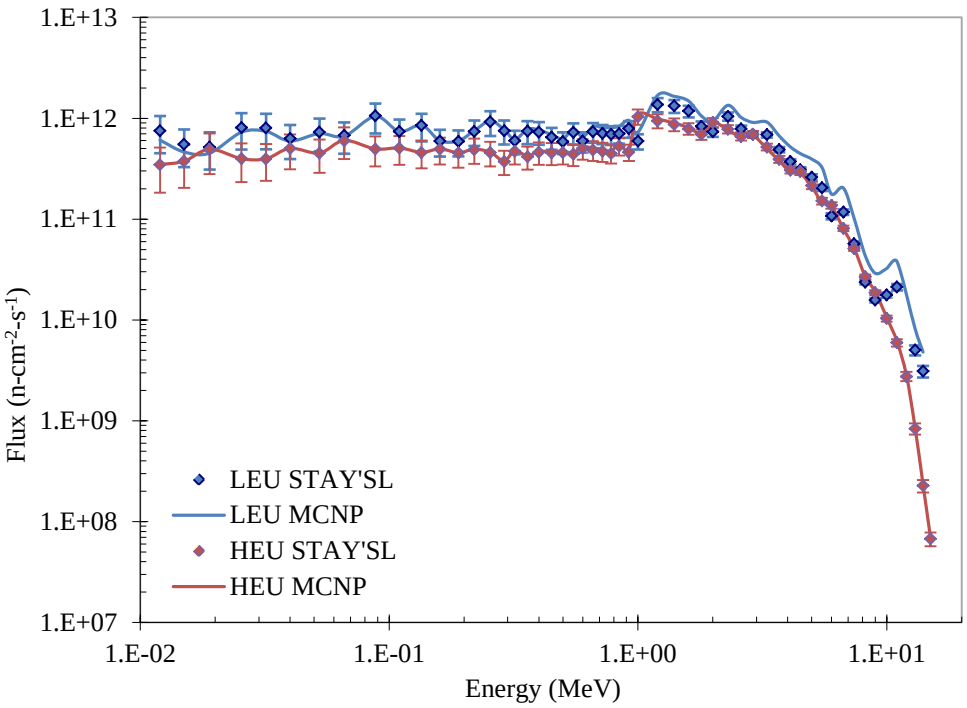

(d)

Figure 6–8 (a through d): Final CLICIT Adjusted Flux Spectra

6.3.4 Rabbit

The full STAY'SL-adjusted spectrum can be seen in Figure 6–9a. The STAY'SL-adjusted thermal spectrum indicates that the LEU thermal flux is less than the HEU thermal flux below 3E-8 MeV (Figure 6–9b) with a slightly higher peak flux, which is indicative of spectrum hardening. The LEU MCNP thermal flux appears to within STAY'SL error. The STAY'SL-adjusted epithermal HEU and LEU spectra begin to lie on top of each other at 1E-6 MeV and the LEU spectra begins to overtake the HEU spectra at approximately 1E-4 MeV (Figure 6–9c). The STAY'SL-adjusted fast spectrum indicates that the LEU MCNP model is accurate as the model falls within STAY'SL error (Figure 6–9d).

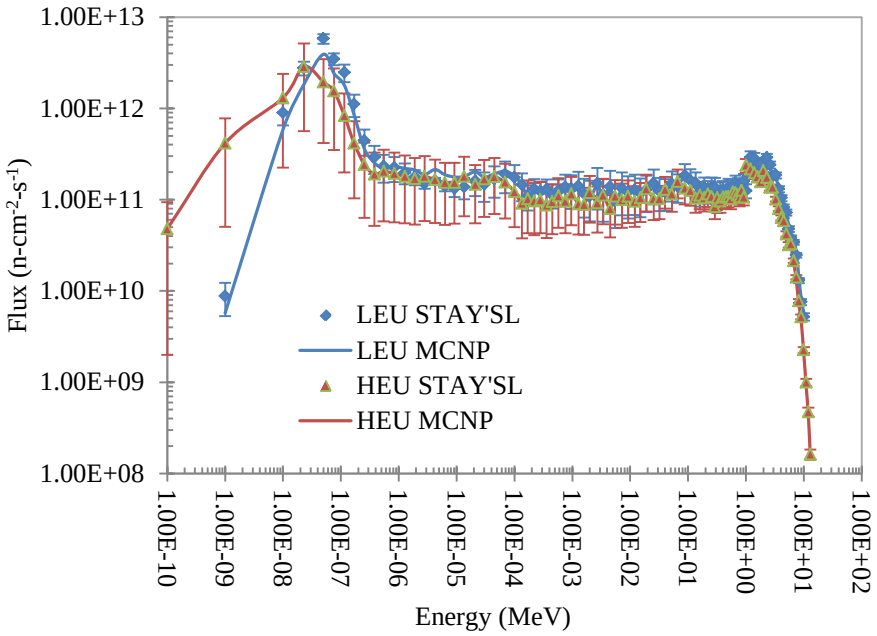
1.00E+13
1.00E+12
1.00E+11
1.00E+10
1.00E+09
1.00E+08
Flux (n-cm-2-s-1)
LEU STAY'SL
LEU MCNP
HEU STAY'SL
HEU MCNP
1.00E-10
1.00E-09
1.00E-08
1.00E-07
1.00E-06
1.00E-05
1.00E-04
1.00E-03
1.00E-02
1.00E-01
1.00E+00
1.00E+01
1.00E+02
Energy (MeV)

(a)

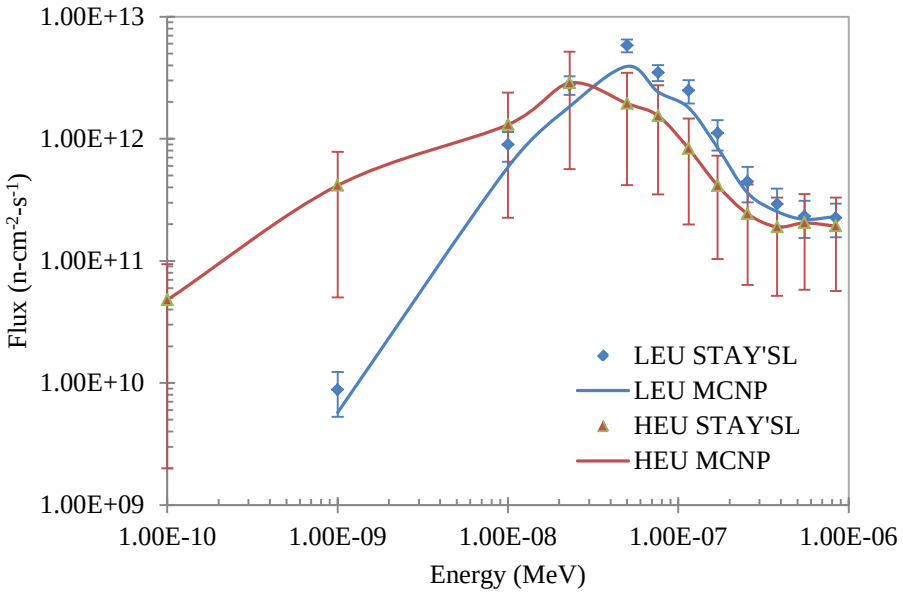
1.00E+13
1.00E+12
1.00E+11
1.00E+10
1.00E+09
Flux (n-cm-2-s-1)
LEU STAY'SL
LEU MCNP
HEU STAY'SL
HEU MCNP
1.00E-10
1.00E-09
1.00E-08
1.00E-07
1.00E-06
Energy (MeV)

(b)

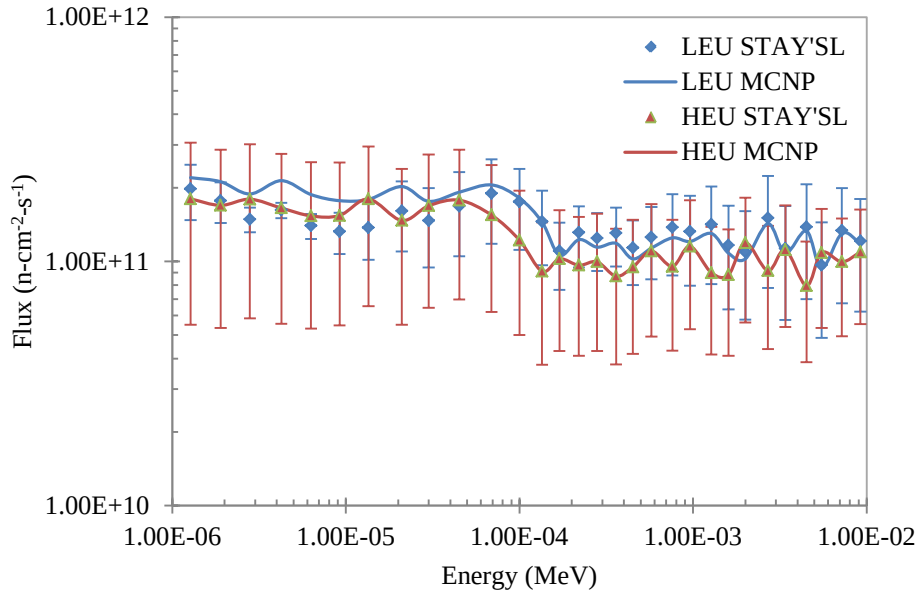

(c)

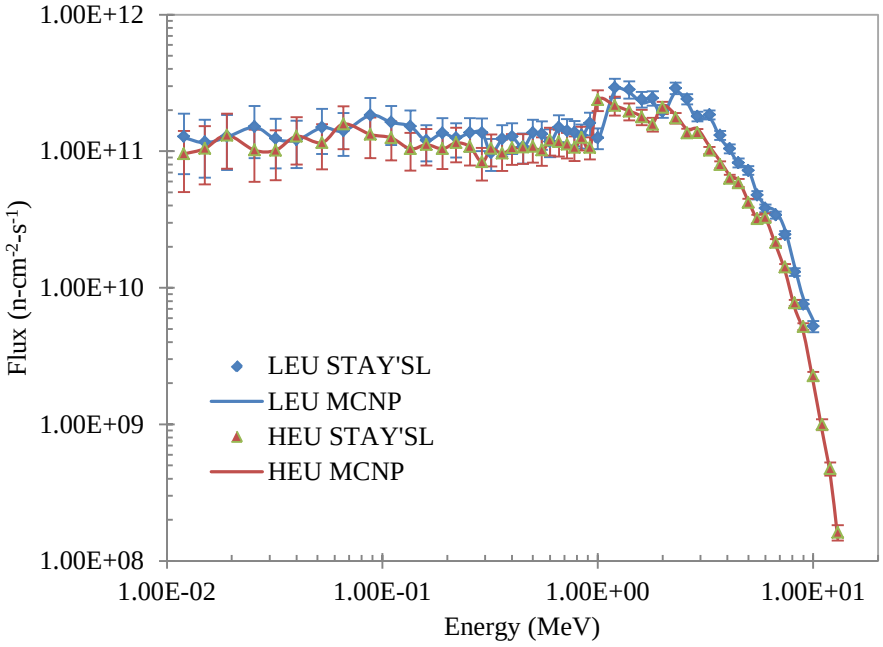

(d)

Figure 6–9 (a through d): Final Rabbit Adjusted Flux Spectra

6.4 LEU Adjusted Spectra

This section contains the adjusted spectra of the GRICIT (newly characterized in this study) and the thermal column.

6.4.1 GRICIT

The GRICIT-C and GRICIT-I adjusted spectra are plotted together. The full STAY'SL-adjusted spectrum can be seen in Figure 6–10a. The STAY'SL-adjusted thermal spectrum indicates that the thermal flux is slightly higher than the MCNP prediction (Figure 6–10b) but appears to be within error. Similar to the previous facilities, the STAY'SL-adjusted epithermal spectra are very slightly overestimated by MCNP between approximately 2E-6 and 2E-5 MeV (Figure 6–10c). This is likely due to the incorrect assumption of fresh fiel in the MCNP model. The MCNP model and STAY'SL-adjusted data appear to correlate above 2E-5 MeV (Figure 6–10d).

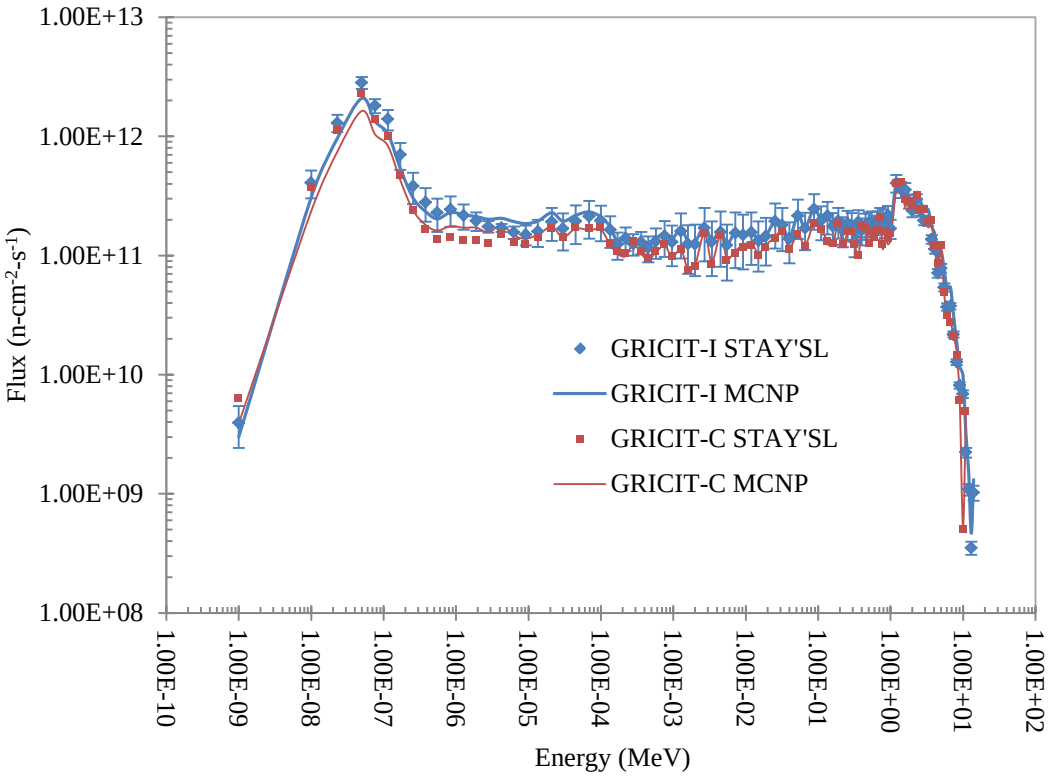
1.00E+13
1.00E+12
1.00E+11
1.00E+10
1.00E+09
1.00E+08
Flux (n-cm-2-s-1)
GRICIT-I STAY'SL
GRICIT-I MCNP
GRICIT-C STAY'SL
GRICIT-C MCNP
1.00E-10
1.00E-09
1.00E-08
1.00E-07
1.00E-06
1.00E-05
1.00E-04
1.00E-03
1.00E-02
1.00E-01
1.00E+00
1.00E+01
1.00E+02
Energy (MeV)

(a)

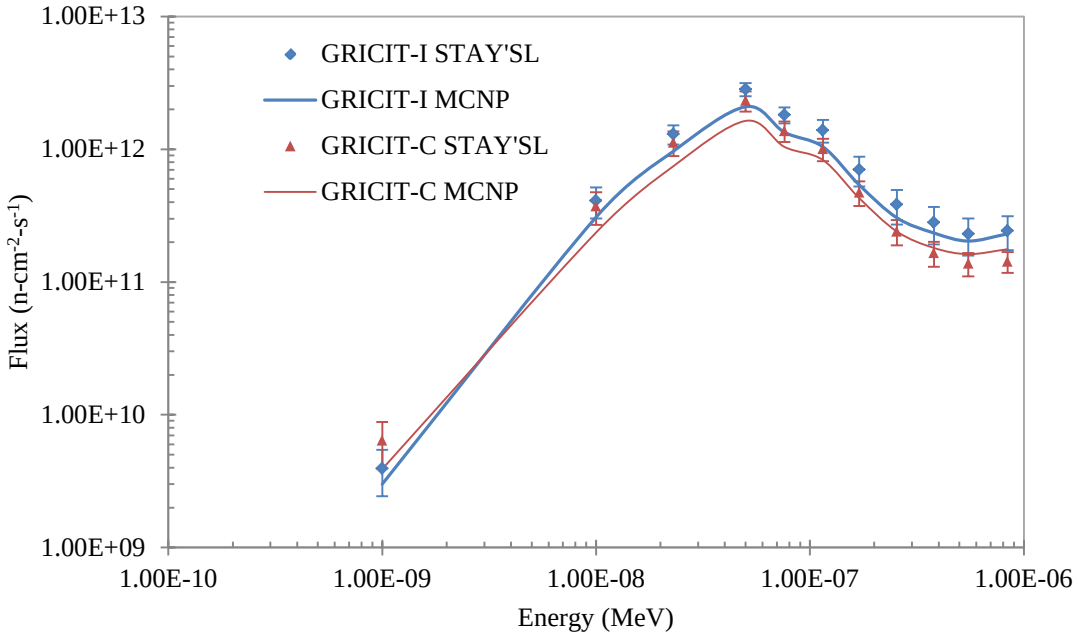
1.00E+13
1.00E+12
1.00E+11
1.00E+10
1.00E+09
Flux (n-cm-2-s-1)
GRICIT-I STAY'SL
GRICIT-I MCNP
GRICIT-C STAY'SL
GRICIT-C MCNP
1.00E-10
1.00E-09
1.00E-08
1.00E-07
1.00E-06
Energy (MeV)

(b)

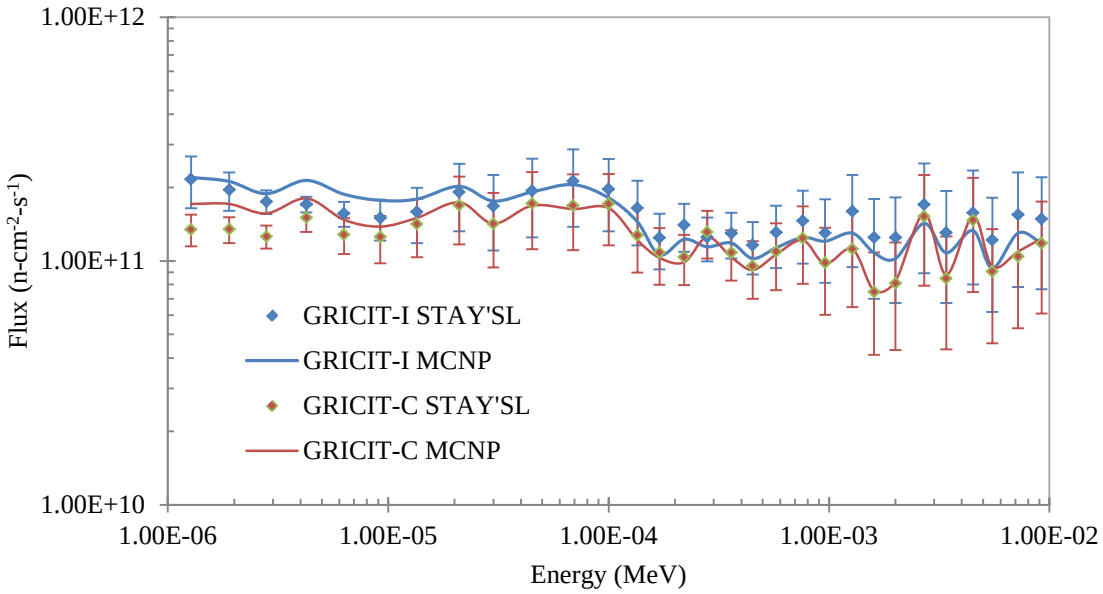

(c)

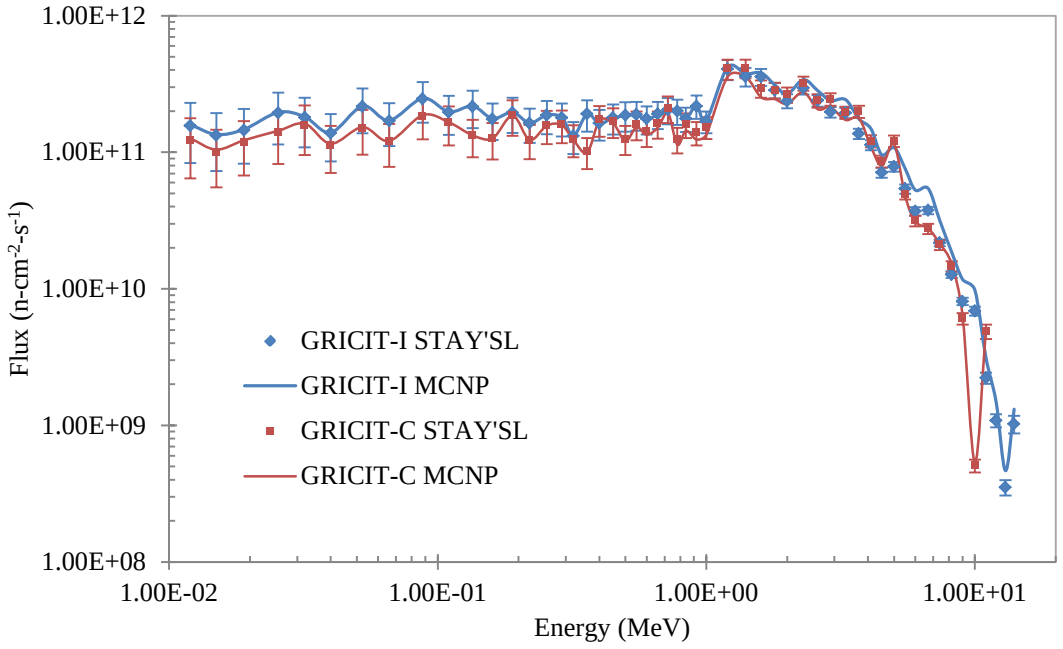

(d)

Figure 6–10 (a through d): Final GRICIT Adjusted Flux Spectra

6.4.2 Thermal Column

The full STAY'SL-adjusted spectrum can be seen in Figure 6–11a. The STAY'SL-adjusted thermal flux below 1E-08 MeV appears to be overestimated by MCNP (Figure 6–11b). This is likely due to the burnup of the assumed fresh fuel. Once again, MCNP appears to over-estimate the epithermal flux up to 1E-04 MeV (Figure 6–11c), which is likely due to the increased amount of resonance absorbers in the fuel compared to the assumed fresh fuel. MCNP and STAY'SL concur well into the fast spectrum, up to 10 MeV (Figure 6–11d).

There is a significant amount of noise in the thermal column epithermal and fast spectra. This is due to the relatively low amount of epithermal and fast neutrons seen in the thermal column due to its distance from the fueled region of the core. Most of the neutrons that reach the entrance to the thermal column will be thermal neutrons as all neutrons have to pass through a significant amount of reflector material to reach the thermal column entrance. There are a few outliers (specifically at 4.5E-3 MeV and 0.66 MeV). This may be due to the specific foils used and the error associated with these foils. The scandium foils were over-irradiated and there was a large amount of counting error because of this. Only one fast flux foil (indium) was used for this facility's characterization due to limitations on the reactor schedule. Perhaps less epithermal/fast fluctuations would've been observed if titanium and nickel foils were also used in the characterization, but this was deemed unnecessary and most (if not all) experimenters utilizing the thermal column are only interested in thermal neutrons.

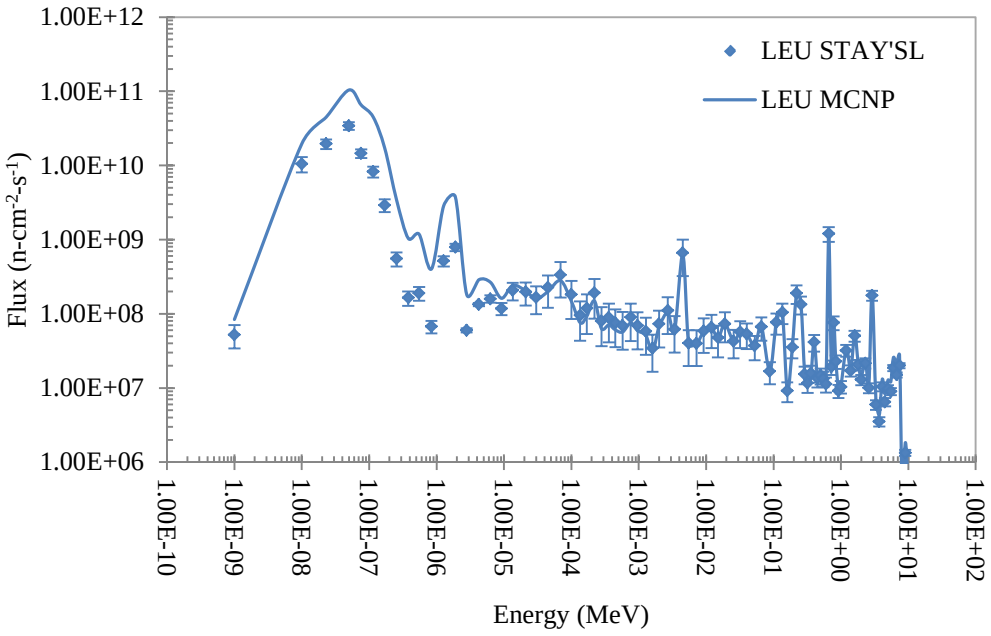
LEU STAY'SL
LEU MCNP
Flux (n-cm-2-s-1)
1.00E+12
1.00E+11
1.00E+10
1.00E+09
1.00E+08
1.00E+07
1.00E+06
1.00E-10
1.00E-09
1.00E-08
1.00E-07
1.00E-06
1.00E-05
1.00E-04
1.00E-03
1.00E-02
1.00E-01
1.00E+00
1.00E+01
1.00E+02
Energy (MeV)

(a)

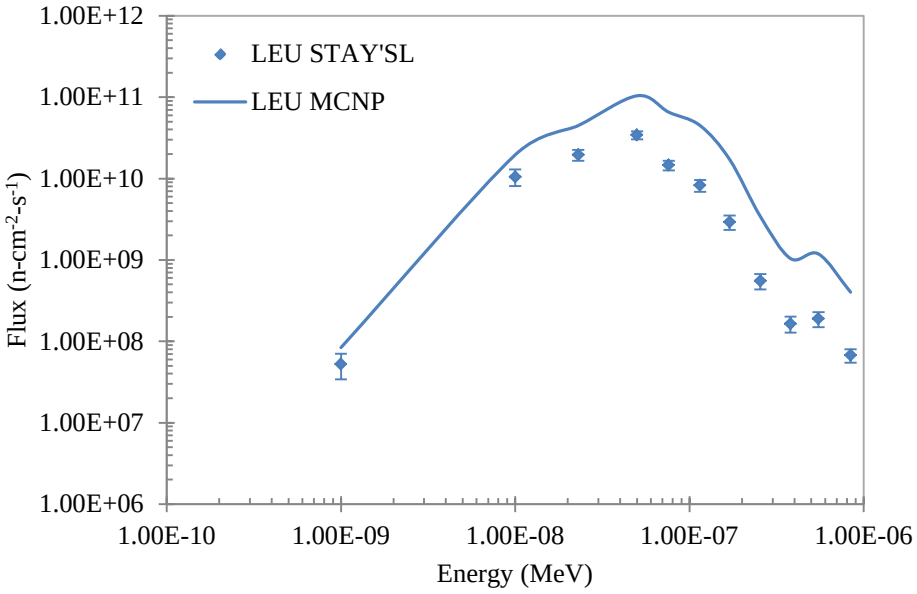
LEU STAY'SL
LEU MCNP
Flux (n-cm-2-s-1)
1.00E+12
1.00E+11
1.00E+10
1.00E+09
1.00E+08
1.00E+07
1.00E+06
1.00E-10
1.00E-09
1.00E-08
1.00E-07
1.00E-06
Energy (MeV)

(b)

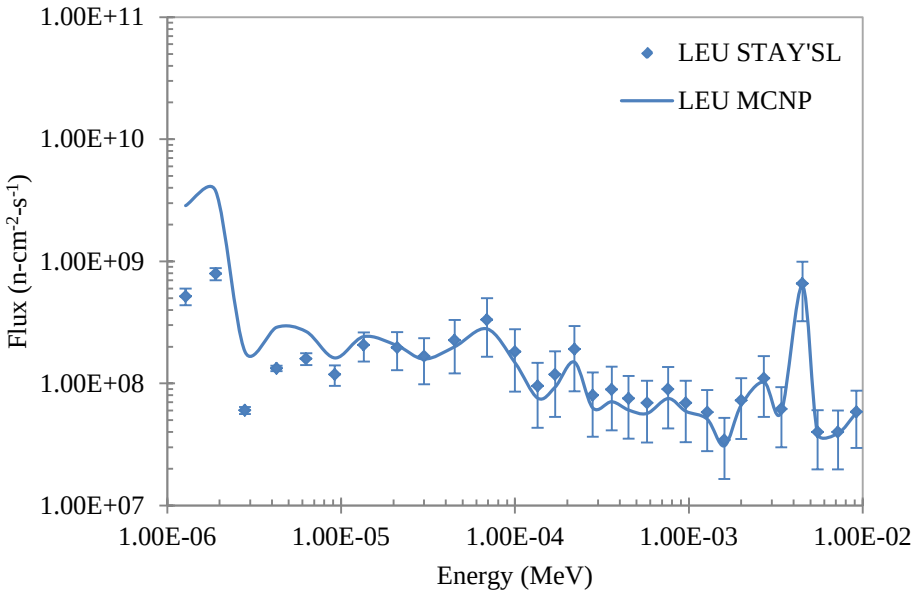

(c)

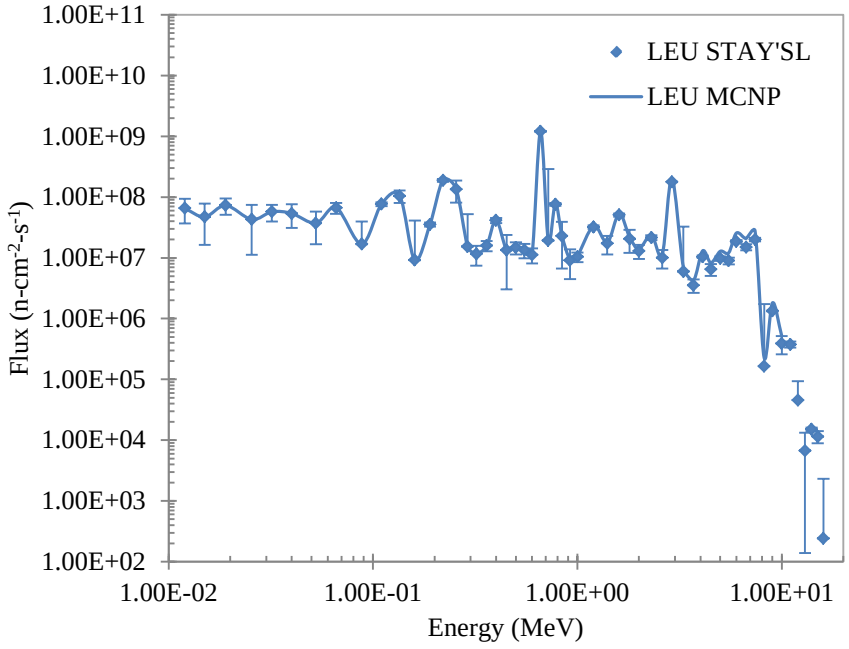

(d)

Figure 6–11 (a through d): Final Thermal Column Adjusted Flux Spectra

6.5 Axial Flux Determination in the Central Thimble

The total and epithermal flux in the central thimble is presented in Figure 6–12.

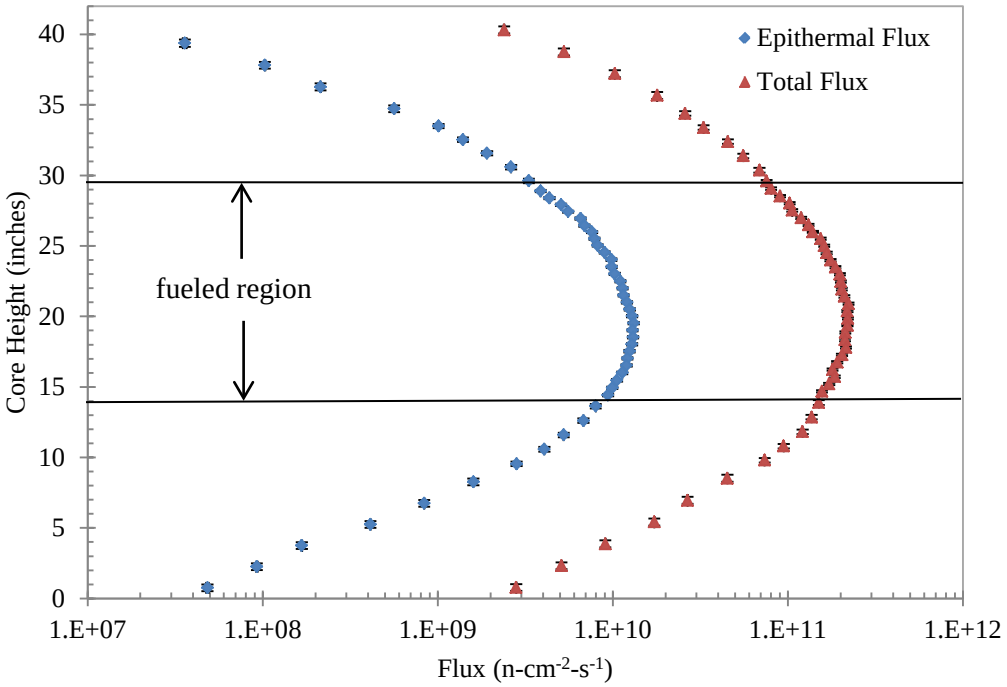

Figure 6–12: Total and epithermal flux in the central thimble

The average control rod height during irradiation was approximately 6.5 inches above the bottom of the fueled region, which would account for the shape of the axial fluxes. If no control rods were present, the flux would appear to have a cosine shape, but the presence of the control rods causes the flux to peak below the center of the fueled region.

Figure 6–13 displays the epithermal and thermal axial fluxes side-by-side.

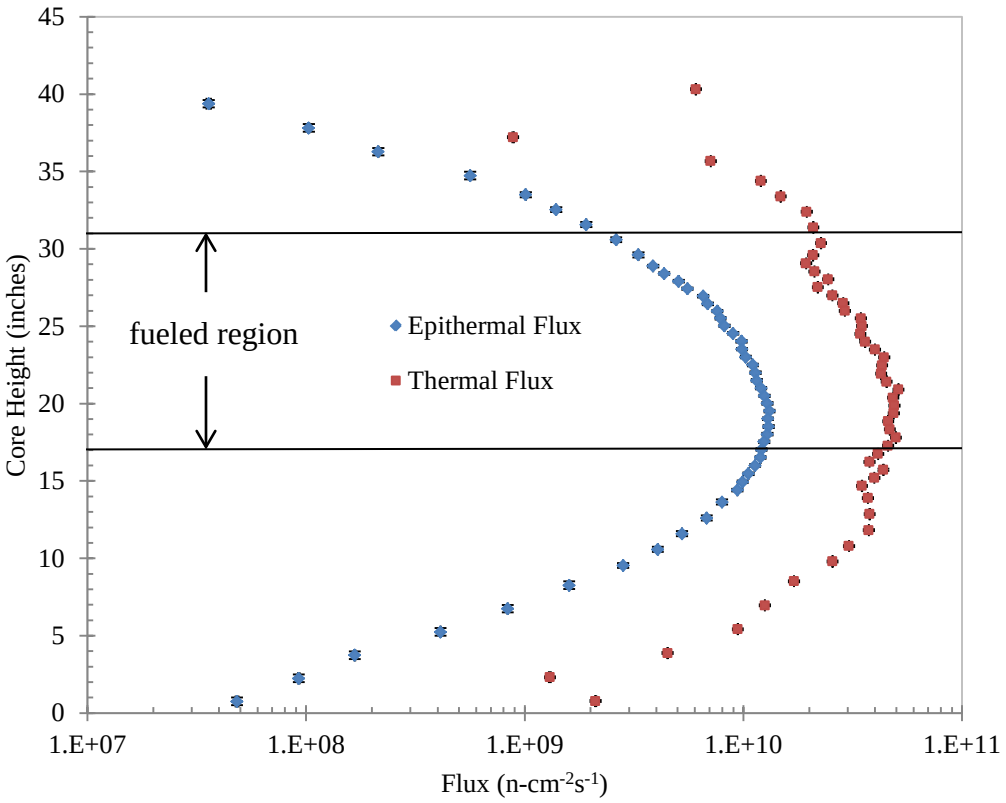

Figure 6–13: Epithermal and thermal axial flux in the central thimble

The thermal flux has the expected flux shape, with the peak flux located below the fuel centerline due to the placement of the control rods. The thermal flux shape differs from the epithermal shape at the axial edges of the fueled region. This is due to the albedo effect of the graphite slugs on the top and bottom of the LEU fuel. The graphite slugs reflect thermal neutrons back into the fueled region of the core, causing slight flux peaks at the edges of the fueled region as seen in the central thimble.

7. CONCLUSION

In summation, this study has characterized the neutron spectra in six of the OSTR's irradiation facilities: the (1) CLICIT, (2) ICIT, (3) Lazy Susan, (4) Rabbit, (5) GRICIT, and (6) Thermal Column. Furthermore a comparison of neutron spectra is given in the first four of these facilities between the HEU and LEU cores. Lastly, the axial flux distribution was quantified in the central thimble.

7.1 Observations

The HEU and LEU neutron spectra were compared for four of the irradiation facilities. It appears that the spectra exhibited relatively similar shapes between the two fuel types. A degree of spectrum hardening in the LEU core is apparent and is primarily due to the increased loading of ^{238}U fuel. The HEU core contained 30% ^{238}U at the beginning of core life, whereas the LEU core contains approximately 80% ^{238}U. The large amount of ^{238}U increases the amount of ^{239}Pu in the fuel which thereby increases the most probable fast neutron energy.

There is a "dip" in the epithermal spectrum above 1E-8 MeV that is consistent between most of the irradiation facilities. This is also consistent with the previous HEU characterization. A similar epithermal overestimation by MCNP was observed at the Belo Horizonte TRIGA® reactor in Brazil [44].

The activation foil data appears to matchup relatively well with the MCNP predictions with the exception of two reactions: Fe-54(n,p)Mn-54 and Fe-56(n,p)Mn-56. Since these two reactions consistently provided inaccurate results, it is assumed that something was wrong with these foils, or particularly, these isotopes within the foils.

7.2 Assumptions and Limitations

This study utilized some assumptions, such as negligible burnup in the fuel and direct comparison of facilities that were affected by fuel geometry. These assumptions caused limitations in the analysis and are described in this section.

7.2.1 Burnup

The MCNP overestimation in the lower epithermal regions is likely due to the assumption of fresh fuel used in the MCNP material cards. In reality, the fuel has built up a large amount of resonance-absorbing material from the transmutation of uranium to plutonium, which would lower the flux seen at the lower epithermal range.

7.2.2 Geometry

It is difficult to truly compare the HEU and LEU cores due to the vast differences in core geometry. Although the spectral shapes are very similar between the two cores, the magnitudes vary due to changes in the geometric locations of the facilities relative to the flux center of the core. Another factor in the core geometry differences is the control rod height differences at full power. In the HEU core, the transient rod was the most reactive rod due to being in the flux center of the core. Pulse limitations required that the transient rod could not be withdrawn more than approximately 50% from the core during normal operations. This differs greatly from the LEU core, where the transient rod can be approximately 70% withdrawn from the core as it is no longer the most reactive rod due to the more symmetric core loading.

7.3 Future Work

There are areas of improvement for this type of characterization. The MCNP models could be updated to include newer cross section data from ENDF-VII. The fuel could be more accurately modeled by improving the fuel element geometry, as the elements are currently modeled as cylinders, which ignores the shapes of the fluted tops and bottoms. Also, burnup calculations could be incorporated into the fuel material cards to improve the epithermal spectra predictions.

The standardization of foil usage would be preferable in future studies. Different foil materials were used in different facilities and although the full energy ranges were overlapped, material standardization would allow for more accurate comparisons between different facilities in the same core configuration. Fission foils could also be implemented as they offer different reactions than standard material foils.

There is a new version of STAY'SL that will be available in the fall of 2012. It has updated cross section data that could increase the precision of the spectral adjustments. It also has a sigma-phi calculator that improves the self-shielding calculations, which would reduce the output error.

The NSVA-3 code offers a new technique for performing spectral adjustments [45]. This code works in a similar fashion as STAY'SL but has the benefit of utilizing a graphical user interface. Future work could utilize this program to perform another spectra characterization; however, covariance matrices must be fully defined in order to use this program. Covariance matrices are very difficult to create. This study would have utilized NSVA-3; however it was decided that the creation of covariance matrices was beyond the scope of this study.

The OSTR reflector is tentatively scheduled to be replaced in the summer of 2013. A future characterization could be performed to determine the effects reflector replacement on current irradiation facilities.

8. BIBLIOGRAPHY

1. Keller, S.T. *Reactor Startup Report for the Oregon State TRIGA® Reactor Using Low Enrichment Uranium Fuel.* April 2009.

2. RERTR.ANL.GOV. *Reduced Enrichment for Research and Test Reactors.* [Online] [Cited: March 29, 2012.] www.rertr.anl.gov.

3. Tiyapun, K. *Epithermal Neutron Beam Deisgn at the Oregon State University TRIGA® Mark II Reactor (OSTR) Based on Monte Carlo Methods.* 1997.

4. Ashbaker, E. *Characterizing the Neutron Spectra in Various Irradiation Facilities within the Oregon State University TRIGA® Reactor.* 2005.

5. Khan, Rustam. *Neutronics Analysis of TRIGA® Mark II reactor and its Experimental Facilities.* 2010.

6. Howerton, R. J., Dye, R. E. and Perkins, S. T. *Evaluated Nuclear Data Library.* s.l. : Lawrence Livermore Laboratory, 1981.

7. Evaluated Nuclear Data File. [Online] http://www.nndc.bnl.gov/exfor/endf00.jsp.

8. McElroy, William Nordell. *Generalized Foil Activation Method of Determining Neutron Flux-Spectra For Radiation Effects Studies.* s.l. : Illinois Institue of Technology, 1965.

9. *Current Status of Neutron Spectrum Unfolding.* IAEA. Vienna, Austria : s.n., 1979.

10. *Review of unfolding methods used in the U.S. and their standardization for dosimetry.* Oster, C. A. Richland, WA : s.n., 1977.

11. Standard Guide for Application of Neutron Spectrum Adjustment Methods in Reactor Surveillance. s.l. : ASTM, 2008. E944-08.

12. Griffin, Patrick J., Kelly, J. G. and VanDenburg, Jason W. User's Manual for SNL-SAND-11 Code. Albuquerque, NM : s.n., 1994.

13. *Radiation Safety Information Computational Center.* [Online] August 2012. http://www-rsicc.ornl.gov/.

14. Zsolnay, E. M., Szondi, E. J. and Nolthenius, H. J. *The Neutron Metrology File NMF-90.* 1999.

15. Negoita, Cezar Ciprian. *Measurement of Neutron Flux Spectra in a Tungsten Benchmark by Neutron Foil Activation Method.* Der Technischen Universität Dresden : s.n., 2004.

16. Perey, F. G. *Least-Squares Dosimetry Unfolding: The Program STAY'SL.* Oak Ridge : Oak Ridge National Laboratory, 1977.

17. Szondi, E. J. and Zsolnay, E. M. *Documentation of the Code SANDBP.* Institute of Nuclear Technical University of Budapest : s.n., 1992.

18. *A comparison of neutron energy spectra in low-enriched and high-enriched uranium cores.* Iqbal, Masood, Ansari, Saleem A. and Zafar, M. S. 4, 1996, Journal of Neutron Research, Vol. 3, pp. 273-283.

19. *A comparative neutronic study of the standard HEU core and various potential LEU alternatives for a typical MNSR system.* Waqar, Sadaf, et al. 238, Islamabad : s.n., 2008, Nuclear Engineering and Design, pp. 2302-2307.

20. *Refining the Accuracy of Predicting Physics Parameters at Research Reactors due to the Limitations in the Energy Balance Method Using MCNP and the ENDF Evaluations.* Peters, N. J., et al. Columbia, MO : s.n., 2012, Nuclear Science and Engineering, Vol. 171, pp. 210-219.

21. Lewis, Elmer E. *Fundamentals of Nuclear Reactor Physics.* 2008.

22. Duderstadt, J.J., Hamilton, L.J. *Nuclear Reactor Analysis.* s.l. : John Wiley & Sons, Inc., 1976.

23. Lamarsh, John R. *Introduction to Nuclear Reactor Theory.* s.l. : Addison-Wesley Publishing Company, 1966.

24. Krane, Kenneth S. *Introductory Nuclear Physics.* s.l. : John Wiley and Sons, 1988.

25. Keller, S. Todd. Irradiation Request #09-188.

26. Team, X-5 Monte Carlo. *MCNP — A General Monte Carlo N-Particle Transport Code, Version 5.* s.l. : Los Alamos National Laboratory, 2008.

27. Bevington, Philip R. and Robinson, D. Keith. *Data Reduction and Error Analysis for the Physical Sciences.* Third. s.l. : McGraw-Hill, 2003.

28. Teller, Edward. *Memoirs: A Twentieth-Century Journey in Science and Politics.* s.l. : Perseus Publishing, 2001.

29. *Radiation Center.* [Online] http://radiationcenter.oregonstate.edu/.

30. Anderson, T. et. al. *OSTR Training Manual.* Corvallis : s.n., 1990.

31. Todreas, Neil E. and Kazimi, Mujid S. *Nuclear Systems I - Thermal Hydraulic Fundamentals.* s.l. : Taylor & Francis, 1993.

32. Josef Stefan Institute. [Online] [Cited: 6 1, 2012.] http://www.rcp.ijs.si/ric/index-a.htm.

33. Jamieson, et. al. Neutron Activation Analysis of Inca and Colonial Ceramics from Central Highland of Ecuador. *Archaeometry.* 2012.

34. Higley, K.A. and Bytwerk, D.P. Invariant scaling relationships and their possible application in predicting radionuclide uptake in plants. *Radioprotection.* 2009, Vol. 44, 5.

35. Lapka, et. al. Extraction of molybdenum and technetium with diamides of dipicolinic acid from nitric acid solutions. *Journal of Radioanalytical and Nuclear Chemistry.* 2009, Vol. 280, 2.

36. Madeira, Jose et. al. Volcano-stratigraphic and structural evolution of Brava Island (Cape Verde) based on 40Ar/39Ar, U–Th and field constraints. *Journal of Volcanology and Geothermal Research.* 2010, Vol. 196, 3-4.

37. *Cl-derived argon isotope production in the CLICIT facility of OSTR reactor and the effects of the Cl-correction in 40Ar/39Ar geochronology.* Renne, Paul R., Sharp, Zachary D. and Heizler, Matthew T. 3-4, 2008, Chemical Geology, Vol. 255, pp. 463-466.

38. Petersen, Nicholas. *Measuring Neutron Absorption Cross Sections of Natural Platinum via Neutron Activation Analysis.* Corvallis : s.n., 2012.

39. Beamud, Elisabet, et. al. Magnetostratigraphy and detrital apatite fission track thermochronology in syntectonic conglomerates: constraints on the exhumation of the South-Central Pyrenees. *Basin Research.* 2011, Vol. 23, 3.

40. Turrin, Brent D. et. al. 40Ar/39Ar ages from the rhyolite of Alder Creek, California: Age of the Cobb Mountain Normal-Polarity Subchron revisited. *Geology (Boulder).* 1994, Vol. 22, 3.

41. National Nuclear Data Center. [Online] http://www.nndc.bnl.gov/exfor/endf00.jsp.

42. Knoll, Glenn F. *Radiation Detection and Measurement.* Third. s.l. : Wiley, 2000.

43. Coleman, Hugh W. and Steele, W. Glenn. *Experimentation, Validation, and Uncertainty Analysis for Engineers.* Third. s.l. : John Wiley & Sons, Inc., 2009.

44. *INDC International Nuclear Data Committee - Second Research Coordination Meeting on Reference Database for Neutron Activation Analysis.* Kellett, Mark A. and Firestone, Richard B. Vienna, Austria : s.n., 2007.

45. *NSVA-3: A computer code for least-squares adjustment of neutron spectra and measured dosimeter responses.* Williams, J. G., Ribaric, A. P. and Schnauber, T. Akersloot, Netherlands : s.n., 2008. Reactor Dosimetry State of the Art 2008 (13th International Symposium).

46. Dorrell, Nick. *Retrospective thermal neutron fluence determination using lithium-ion mobile telephone batteries.* Corvallis : s.n., 2011.

47. *A Compton-suppressed phoswich detector for radioxenon measurements.* Farsoni, A. et. al. Corvallis : s.n., 2011. Nuclear Science Symposium and Medical Imaging Conference.

48. Keller, S.T. *Modeling the Oregon State University TRIGA® Reactor Using the Attila Three-Dimensional Deterministic Transport Code.* 2007.

9. NOMENCLATURE

Symbols

A(t)	time-dependent activity
C	counts detected
E	energy
M	atomic weight
N_A	Avogadro's number
N_0	number of atoms in irradiation foil sample
N(t)	daughter product build-up
R	number of activation reactions
S	standard deviation (used for Chauvenet's criterion)
T	temperature
d_{max}	maximum deviation from the mean
f(E)	fractional energy spectrum
f_{iso}	isotopic abundance
f_γ	branching ratio
k	Boltzmann constant
m	mass of foil
n'''	neutron density
t_0	irradiation time
t_1	time from end of bombardment to beginning of counts
t_2	time at end of counts
$\chi(E)$	Watt fission spectrum
χ^2	chi-squared
χ_m^2	minimized reduced chi-squared
Ω	geometric efficiency
ε	intrinsic efficiency
ε_A	error of sigma-phi reaction rate
ε_C	error of counts
ε_m	error of foil mass
ε_t	error of counting time
ε_ε	error of detector efficiency

ϕ	flux
λ	decay constant
σ_a	absorption cross section
σ_f	fission cross section
σ_n	elastic scattering cross section
$\sigma_{n'}$	inelastic scattering cross section
σ_s	scattering cross section
σ_T	total cross section
σ_{th}	thermal absorption cross section
σ_γ	capture cross section
$\bar{\sigma}$	average thermal neutron absorption cross section

APPENDICES

APPENDIX A – STAY'SL MANUAL

This appendix will explain the syntax of the STAY'SL program, using the ICIT input deck as an example (Figure A-1).

Line 1: Arbitrary title line

Line 2: 5 numbers are input: NGROUP, NFOIL, INPT, IACT, KQT

- NGROUP = number of energy groups (normally 100)
- NFOIL = number of activities measured (must be less than 40)
- IPNT = 1 to suppress output of cross section data, 2 to suppress output of covariance matrices, 3 to print sig-phi file, 4 to print cover factors
- IACT = 0 for spectral adjustment; 1 for activity run, 2 for cross section adjustment
- KQT = 0 for differential flux input, 1 for group flux input, 2 for flux/lethargy (E*PHI)

Line 3: This line offers the user an option to input a covariance matrix or to use a Gaussian formalism. For the purposes of this study, the standard Gaussian formalism was employed. Future versions of STAY'SL will incorporate covariance matrices for cross section data.

Line 4: 4 numbers are input: (AK1, NOR, ILOG, TIME)

- AK1 = set at 0.0 for an automated normalization of input flux prior to spectral adjustment, 1.0 for absolute fixed input flux (no normalization is performed), or x.x for renormalization to stated value x.x (i.e. all fluxes are multiplied by this factor)
- NOR = 0 for flux renormalization by chi-square (preferred), 1 for flux renormalization by standard deviation
- ILOG = 0 for logarithmic flux changes (large changes only), 1 for linear flux changes (caution - flux < 0 possible)
- TIME = Length of irradiation in seconds. This is used to compute fluence values only for ease of reporting. Caution-TIME is divided by ACNM when fluence values are calculated. This allows activities to be time-averaged, fluxes normalized to full power, and fluence values to consider both effects.

Lines 5-18: These are the activities from the irradiated foils.

Table A–1: Explanation of activity line of STAY'SL input deck

Columns	Input (from line 6)	Description
1-8	FE58G	Short name of reaction
9-18	1.245E-11	Sigma-phi value (atoms/atom-second)
19-24	0.04	Uncertainty of sigma-phi value
25-28	CADM	First four letters of cover material (Cd, B, Au, Gd or Hf)
31-34	ISTP	Isotropic (ISTP) or beam (BEAM) flux
35-40	20.	Cover thickness in mils
41-44	SFSH	This indicates self-shielding (must calculate using SHIELD program)
47-49	IFX	BFX, IFX, BWX or IWX (B = beam, I = isotropic, F = foil, W = wire)
51-56	5.	Thickness of foil or wire in mils
57-60	FENG	Arbitrary name that must match same reaction's designation in SHIELD self-shielding file

Line 19: Title line for input uncertainty

Line 20: INGP,TNORM (# groups, normalization factor)

Line 21: Energy cutoff values

Line 22: Variance of line 21's cutoff values. These values are the diagonal terms of the flux covariance matrix, with the off-diagonal terms calculated using the Gaussian formalism from line 3.

Line 23: Title line for Input Flux. The user has an option to put a number in from of the title. If the number is zero (or blank), then the TEMP and ETE are ignored in line 24. If the number is 1, then a Maxwellian adjustment is made to the flux for energies below the ETE value.

Line 24: INGP, TNORM, TEMP, ETE

- INGP = Number of energy groups
- TNORM = Normalization factor
- TEMP = Temperature of modeled facility (usually 20°C)
- ETE = 1/E joining energy

Lines 25-37: Input Flux values (from MCNP): The 100 group flux values calculated from MCNP are input here. The reason for 100 groups is that STAY'SL uses a

100 group energy structure, so the MCNP fluxes are measured at the corresponding STAY'SL energies.

```
 OSU TRIGA ICIT 7/14/12
00100   14    2 0000   1
 .005    9.0   0.03  20.0    0.03  .03   1.0
 3.0        0  0   3.60E+3
FE58G   1.245e-11 0.03                  SFSH  IFX 5.    FENG
FE58G   2.184e-12 0.04  CADM  ISTP 20.  SFSH  IFX 5.    FENG
FE54P   1.371e-12 0.03
FE54A   1.527E-14 0.08
TI46P   1.877e-13 0.04
TI47P   3.451e-13 0.03
TI48P   4.977e-15 0.04
AL27A   1.059e-14 0.10
AU197G  1.781E-09 0.02                  SFSH  IFX 5.    AUNG
AU197G  1.844E-09 0.17  CADM  ISTP 20.  SFSH  IFX 5.    AUNG
W186G   3.191E-10 0.26                  SFSH  IFX 5.    WUNG
W186G   1.402E-10 0.28  CADM  ISTP 20.  SFSH  IFX 5.    WUNG
IN115N  2.383e-12 0.02
NI58P   1.201e-12 0.02
 TRIGA INPUT UNCERTAINTY
4  1.0
0.99E-10  0.01  1.5  20.1
1.  0.5  0.2  0.2
1 INPUT FOR OSU TRIGA ICIT
 100 1.0 20. 5.00E-07
2.92E+09 2.98E+11 9.09E+11 2.01E+12 1.31E+12 1.08E+12 6.24E+11 4.16E+11
3.39E+11 3.01E+11 3.49E+11 3.38E+11 3.12E+11 3.10E+11 3.33E+11 3.08E+11
2.94E+11 3.13E+11 3.65E+11 2.98E+11 3.52E+11 3.77E+11 3.34E+11 2.70E+11
2.10E+11 2.39E+11 2.24E+11 2.32E+11 2.09E+11 2.28E+11 2.72E+11 2.13E+11
2.84E+11 2.15E+11 2.22E+11 2.94E+11 2.28E+11 2.79E+11 2.07E+11 2.68E+11
2.45E+11 2.76E+11 2.38E+11 2.46E+11 3.25E+11 2.89E+11 2.35E+11 3.37E+11
3.11E+11 4.38E+11 3.26E+11 3.59E+11 3.03E+11 3.24E+11 2.94E+11 3.20E+11
3.27E+11 2.61E+11 3.48E+11 2.95E+11 2.87E+11 3.22E+11 3.18E+11 3.05E+11
3.56E+11 3.33E+11 3.50E+11 3.34E+11 4.03E+11 3.24E+11 7.88E+11 6.95E+11
6.22E+11 5.46E+11 4.71E+11 6.05E+11 5.20E+11 4.15E+11 4.37E+11 3.17E+11
2.47E+11 1.99E+11 1.83E+11 1.27E+11 9.25E+10 9.38E+10 5.13E+10 3.27E+10
1.74E+10 1.60E+10 7.65E+09 4.57E+09 9.23E+08 1.22E+09 3.62E+08 0.00E+00
0.00E+00 0.00E+00 0.00E+00 0.00E+00
```

Figure A-1: STAY'SL input deck for ICIT facility

APPENDIX B – STAY'SL-ADJUSTED LEU FLUX

All values in this table are in units of neutrons per cm^2-s.

Energy (MeV)	CLICIT	GRICIT-C	GRICIT-I	ICIT	Lazy Susan	Rabbit	Thermal Column
1.00E-10	0	0	0	4.50E+09	1.35E+09	0	0
1.00E-09	0	6.40E+09	3.94E+09	4.53E+11	1.53E+11	8.79E+09	5.22E+07
1.00E-08	0	3.72E+11	4.08E+11	1.35E+12	5.04E+11	8.94E+11	1.05E+10
2.30E-08	2.00E+08	1.12E+12	1.30E+12	2.89E+12	1.20E+12	2.77E+12	1.95E+10
5.00E-08	1.63E+09	2.32E+12	2.83E+12	1.81E+12	8.01E+11	5.82E+12	3.42E+10
7.60E-08	1.10E+09	1.38E+12	1.81E+12	1.43E+12	6.05E+11	3.49E+12	1.46E+10
1.15E-07	1.01E+09	1.01E+12	1.39E+12	7.93E+11	2.95E+11	2.48E+12	8.24E+09
1.70E-07	3.91E+08	4.73E+11	7.01E+11	5.04E+11	1.40E+11	1.11E+12	2.92E+09
2.55E-07	1.33E+08	2.41E+11	3.82E+11	3.91E+11	8.81E+10	4.45E+11	5.53E+08
3.80E-07	3.51E+08	1.66E+11	2.80E+11	3.28E+11	6.32E+10	2.91E+11	1.65E+08
5.50E-07	2.75E+10	1.38E+11	2.29E+11	3.60E+11	5.71E+10	2.32E+11	1.89E+08
8.40E-07	2.07E+11	1.43E+11	2.43E+11	3.31E+11	4.38E+10	2.25E+11	6.73E+07
1.28E-06	3.27E+11	1.35E+11	2.16E+11	2.91E+11	3.12E+10	1.98E+11	5.16E+08
1.90E-06	3.73E+11	1.35E+11	1.96E+11	2.80E+11	2.22E+10	1.77E+11	7.90E+08
2.80E-06	3.56E+11	1.26E+11	1.75E+11	2.97E+11	1.79E+10	1.49E+11	6.01E+07
4.25E-06	3.55E+11	1.50E+11	1.71E+11	2.80E+11	1.61E+10	1.62E+11	1.33E+08
6.30E-06	3.07E+11	1.28E+11	1.56E+11	2.80E+11	1.52E+10	1.40E+11	1.59E+08
9.20E-06	3.09E+11	1.25E+11	1.50E+11	3.20E+11	1.49E+10	1.33E+11	1.18E+08
1.35E-05	3.45E+11	1.41E+11	1.59E+11	4.11E+11	1.72E+10	1.37E+11	2.06E+08
2.10E-05	4.34E+11	1.69E+11	1.92E+11	3.74E+11	1.49E+10	1.61E+11	1.96E+08
3.00E-05	3.27E+11	1.42E+11	1.68E+11	4.95E+11	2.03E+10	1.47E+11	1.67E+08
4.50E-05	4.06E+11	1.72E+11	1.94E+11	5.92E+11	2.67E+10	1.68E+11	2.26E+08
6.90E-05	4.41E+11	1.69E+11	2.13E+11	5.81E+11	2.85E+10	1.90E+11	3.32E+08
1.00E-04	3.70E+11	1.72E+11	1.97E+11	5.14E+11	2.73E+10	1.75E+11	1.82E+08
1.35E-04	3.54E+11	1.27E+11	1.65E+11	4.33E+11	2.32E+10	1.46E+11	9.52E+07
1.70E-04	3.49E+11	1.08E+11	1.24E+11	5.26E+11	3.05E+10	1.10E+11	1.19E+08
2.20E-04	4.09E+11	1.04E+11	1.40E+11	5.19E+11	3.31E+10	1.31E+11	1.91E+08
2.80E-04	3.97E+11	1.31E+11	1.25E+11	5.60E+11	3.50E+10	1.24E+11	8.00E+07
3.60E-04	4.16E+11	1.08E+11	1.30E+11	5.19E+11	3.35E+10	1.31E+11	8.91E+07
4.50E-04	3.80E+11	9.52E+10	1.16E+11	5.77E+11	4.01E+10	1.13E+11	7.52E+07
5.75E-04	5.61E+11	1.09E+11	1.31E+11	6.94E+11	4.73E+10	1.26E+11	6.92E+07
7.60E-04	5.57E+11	1.24E+11	1.46E+11	5.45E+11	4.15E+10	1.38E+11	8.97E+07
9.60E-04	5.85E+11	9.84E+10	1.30E+11	7.24E+11	5.41E+10	1.32E+11	6.91E+07
1.28E-03	8.03E+11	1.12E+11	1.60E+11	5.44E+11	4.82E+10	1.41E+11	5.82E+07
1.60E-03	6.53E+11	7.47E+10	1.25E+11	5.56E+11	4.88E+10	1.16E+11	3.44E+07
2.00E-03	6.18E+11	8.10E+10	1.25E+11	7.29E+11	6.49E+10	1.09E+11	7.27E+07

2.70E-03	8.58E+11	1.52E+11	1.70E+11	5.59E+11	5.14E+10	1.51E+11	1.10E+08
3.40E-03	6.46E+11	8.47E+10	1.30E+11	6.77E+11	6.20E+10	1.13E+11	6.15E+07
4.50E-03	8.62E+11	1.47E+11	1.57E+11	4.97E+11	4.72E+10	1.38E+11	6.59E+08
5.50E-03	6.48E+11	9.06E+10	1.22E+11	6.39E+11	6.33E+10	9.66E+10	4.00E+07
7.20E-03	7.36E+11	1.04E+11	1.54E+11	5.80E+11	6.07E+10	1.34E+11	3.99E+07
9.20E-03	7.40E+11	1.18E+11	1.48E+11	6.50E+11	7.18E+10	1.21E+11	5.84E+07
1.20E-02	7.54E+11	1.21E+11	1.57E+11	5.57E+11	5.92E+10	1.28E+11	6.54E+07
1.50E-02	5.53E+11	1.01E+11	1.33E+11	5.73E+11	6.54E+10	1.17E+11	4.74E+07
1.90E-02	5.19E+11	1.18E+11	1.45E+11	7.55E+11	9.17E+10	1.29E+11	7.29E+07
2.55E-02	8.09E+11	1.39E+11	1.94E+11	6.69E+11	1.05E+11	1.52E+11	4.28E+07
3.20E-02	8.02E+11	1.58E+11	1.80E+11	5.42E+11	4.17E+10	1.24E+11	5.71E+07
4.00E-02	6.29E+11	1.13E+11	1.38E+11	7.76E+11	8.56E+10	1.21E+11	5.36E+07
5.25E-02	7.32E+11	1.50E+11	2.16E+11	7.14E+11	9.13E+10	1.50E+11	3.71E+07
6.60E-02	6.80E+11	1.19E+11	1.70E+11	1.00E+12	1.31E+11	1.41E+11	6.65E+07
8.80E-02	1.06E+12	1.85E+11	2.46E+11	7.46E+11	7.24E+10	1.84E+11	1.68E+07
1.10E-01	7.42E+11	1.65E+11	1.96E+11	8.20E+11	1.04E+11	1.63E+11	7.63E+07
1.35E-01	8.53E+11	1.32E+11	2.16E+11	6.91E+11	5.71E+10	1.53E+11	1.04E+08
1.60E-01	5.96E+11	1.26E+11	1.76E+11	7.37E+11	6.82E+10	1.20E+11	9.15E+06
1.90E-01	5.91E+11	1.86E+11	1.95E+11	6.68E+11	7.13E+10	1.36E+11	3.53E+07
2.20E-01	7.42E+11	1.24E+11	1.63E+11	7.25E+11	7.51E+10	1.25E+11	1.89E+08
2.55E-01	9.23E+11	1.58E+11	1.87E+11	7.39E+11	7.30E+10	1.37E+11	1.34E+08
2.90E-01	7.54E+11	1.60E+11	1.79E+11	5.88E+11	4.81E+10	1.37E+11	1.53E+07
3.20E-01	5.98E+11	1.25E+11	1.32E+11	7.81E+11	7.50E+10	9.72E+10	1.16E+07
3.60E-01	7.48E+11	1.01E+11	1.91E+11	6.58E+11	5.74E+10	1.23E+11	1.58E+07
4.00E-01	7.33E+11	1.74E+11	1.63E+11	6.37E+11	6.72E+10	1.28E+11	4.15E+07
4.50E-01	6.48E+11	1.69E+11	1.79E+11	7.09E+11	6.92E+10	1.08E+11	1.35E+07
5.00E-01	5.85E+11	1.26E+11	1.87E+11	6.94E+11	6.30E+10	1.37E+11	1.47E+07
5.50E-01	7.24E+11	1.60E+11	1.89E+11	6.58E+11	5.91E+10	1.34E+11	1.34E+07
6.00E-01	5.93E+11	1.43E+11	1.76E+11	7.58E+11	5.78E+10	1.18E+11	1.12E+07
6.60E-01	7.37E+11	1.62E+11	1.91E+11	6.99E+11	6.22E+10	1.50E+11	1.20E+09
7.20E-01	7.07E+11	2.10E+11	2.05E+11	7.22E+11	5.08E+10	1.41E+11	1.92E+07
7.80E-01	6.92E+11	1.25E+11	2.01E+11	6.77E+11	4.78E+10	1.38E+11	7.60E+07
8.40E-01	7.02E+11	1.60E+11	1.76E+11	8.01E+11	5.72E+10	1.31E+11	2.28E+07
9.20E-01	7.90E+11	1.39E+11	2.18E+11	6.31E+11	4.50E+10	1.61E+11	9.14E+06
1.00E+00	5.95E+11	1.53E+11	1.69E+11	1.51E+12	1.05E+11	1.25E+11	1.04E+07
1.20E+00	1.37E+12	4.08E+11	4.06E+11	1.31E+12	9.08E+10	2.93E+11	3.21E+07
1.40E+00	1.33E+12	4.12E+11	3.58E+11	1.15E+12	7.43E+10	2.84E+11	1.72E+07
1.60E+00	1.18E+12	2.93E+11	3.56E+11	9.96E+11	6.20E+10	2.40E+11	5.05E+07
1.80E+00	8.35E+11	2.85E+11	2.85E+11	8.46E+11	5.65E+10	2.45E+11	2.06E+07
2.00E+00	7.35E+11	2.64E+11	2.38E+11	1.07E+12	5.87E+10	1.97E+11	1.29E+07

2.30E+00	1.05E+12	3.20E+11	2.96E+11	9.16E+11	5.45E+10	2.89E+11	2.16E+07
2.60E+00	7.88E+11	2.39E+11	2.39E+11	7.28E+11	3.73E+10	2.41E+11	1.00E+07
2.90E+00	6.94E+11	2.45E+11	1.97E+11	7.65E+11	3.66E+10	1.80E+11	1.77E+08
3.30E+00	6.88E+11	1.96E+11	1.94E+11	5.55E+11	2.08E+10	1.85E+11	5.96E+06
3.70E+00	4.90E+11	1.99E+11	1.37E+11	4.32E+11	2.00E+10	1.31E+11	3.53E+06
4.10E+00	3.72E+11	1.21E+11	1.13E+11	3.49E+11	1.71E+10	1.04E+11	1.04E+07
4.50E+00	3.08E+11	8.59E+10	7.11E+10	3.20E+11	1.62E+10	8.25E+10	6.48E+06
5.00E+00	2.61E+11	1.21E+11	7.84E+10	2.22E+11	1.12E+10	7.25E+10	9.72E+06
5.50E+00	2.05E+11	4.96E+10	5.40E+10	1.61E+11	9.16E+09	4.77E+10	8.98E+06
6.00E+00	1.07E+11	3.15E+10	3.70E+10	1.62E+11	6.51E+09	3.82E+10	1.86E+07
6.70E+00	1.18E+11	2.75E+10	3.76E+10	8.84E+10	5.55E+09	3.42E+10	1.50E+07
7.40E+00	5.69E+10	2.10E+10	2.18E+10	5.62E+10	2.35E+09	2.46E+10	2.00E+07
8.20E+00	2.38E+10	1.46E+10	1.27E+10	2.99E+10	2.05E+09	1.30E+10	1.65E+05
9.00E+00	1.58E+10	6.05E+09	8.11E+09	2.75E+10	1.20E+09	7.57E+09	1.33E+06
1.00E+01	1.77E+10	5.07E+08	6.87E+09	1.33E+10	1.78E+09	5.21E+09	3.87E+05
1.10E+01	2.13E+10	4.89E+09	2.23E+09	8.02E+09	0	0	3.76E+05
1.20E+01	0	0	1.09E+09	1.65E+09	2.70E+07	0	4.55E+04
1.30E+01	5.04E+09	0	3.52E+08	2.22E+09	1.34E+08	0	6.72E+03
1.40E+01	3.11E+09	0	1.02E+09	6.76E+08	0	0	1.51E+04
1.50E+01	0	0	0	0	0	0	1.15E+04
1.60E+01	0	0	0	0	0	0	2.42E+02

APPENDIX C – STAY'SL-ADJUSTED FLUX PER UNIT LETHARGY

All values in this table are in units of neutrons per cm^2-s.

Energy (MeV)	CLICIT	GRICIT-C	GRICIT-I	ICIT	Lazy Susan	Rabbit	Thermal Column
1.00E-10	0	0	0	4.104E+09	3.548E+08	0	0
1.00E-09	0	0	0	4.104E+09	3.548E+08	0	0
1.00E-09	0	2.38E+09	1.021E+09	4.189E+11	4.051E+10	3.499E+09	5.121E+07
1.00E-08	0	2.38E+09	1.021E+09	4.189E+11	4.051E+10	3.499E+09	5.121E+07
1.00E-08	0	2.99E+11	2.170E+11	2.654E+12	2.794E+11	7.453E+11	2.483E+10
2.30E-08	0	2.99E+11	2.170E+11	2.654E+12	2.794E+11	7.453E+11	2.483E+10
2.30E-08	2.699E+08	1.01E+12	7.259E+11	6.250E+12	7.194E+11	2.481E+12	6.056E+10
5.00E-08	2.699E+08	1.01E+12	7.259E+11	6.250E+12	7.194E+11	2.481E+12	6.056E+10
5.00E-08	4.007E+09	3.95E+12	2.811E+12	7.301E+12	8.863E+11	9.503E+12	2.520E+11
7.60E-08	4.007E+09	3.95E+12	2.811E+12	7.301E+12	8.863E+11	9.503E+12	2.520E+11
7.60E-08	2.786E+09	2.55E+12	1.824E+12	6.083E+12	7.073E+11	5.932E+12	1.601E+11
1.15E-07	2.786E+09	2.55E+12	1.824E+12	6.083E+12	7.073E+11	5.932E+12	1.601E+11
1.15E-07	2.804E+09	2.14E+12	1.500E+12	3.718E+12	3.886E+11	4.646E+12	1.161E+11
1.70E-07	2.804E+09	2.14E+12	1.500E+12	3.718E+12	3.886E+11	4.646E+12	1.161E+11
1.70E-07	1.092E+09	1.07E+12	7.475E+11	2.392E+12	1.935E+11	2.113E+12	4.285E+10
2.55E-07	1.092E+09	1.07E+12	7.475E+11	2.392E+12	1.935E+11	2.113E+12	4.285E+10
2.55E-07	3.981E+08	6.08E+11	4.293E+11	1.980E+12	1.389E+11	9.163E+11	8.687E+09
3.80E-07	3.981E+08	6.08E+11	4.293E+11	1.980E+12	1.389E+11	9.163E+11	8.687E+09
3.80E-07	1.208E+09	4.93E+11	3.556E+11	1.894E+12	1.237E+11	6.941E+11	2.845E+09
5.50E-07	1.208E+09	4.93E+11	3.556E+11	1.894E+12	1.237E+11	6.941E+11	2.845E+09
5.50E-07	8.915E+10	3.88E+11	2.708E+11	1.924E+12	1.171E+11	5.252E+11	2.838E+09
8.40E-07	8.915E+10	3.88E+11	2.708E+11	1.924E+12	1.171E+11	5.252E+11	2.838E+09
8.40E-07	7.351E+11	4.29E+11	3.112E+11	1.890E+12	1.129E+11	5.608E+11	9.773E+08
1.28E-06	7.351E+11	4.29E+11	3.112E+11	1.890E+12	1.129E+11	5.608E+11	9.773E+08
1.28E-06	1.317E+12	4.35E+11	3.099E+11	1.823E+12	1.086E+11	5.593E+11	7.264E+09
1.90E-06	1.317E+12	4.35E+11	3.099E+11	1.823E+12	1.086E+11	5.593E+11	7.264E+09
1.90E-06	1.667E+12	4.47E+11	3.081E+11	1.862E+12	1.069E+11	5.531E+11	9.818E+09
2.80E-06	1.667E+12	4.47E+11	3.081E+11	1.862E+12	1.069E+11	5.531E+11	9.818E+09
2.80E-06	1.587E+12	3.81E+11	2.723E+11	1.862E+12	1.074E+11	4.589E+11	4.424E+08
4.25E-06	1.587E+12	3.81E+11	2.723E+11	1.862E+12	1.074E+11	4.589E+11	4.424E+08
4.25E-06	1.760E+12	4.64E+11	2.933E+11	1.823E+12	1.073E+11	5.505E+11	7.411E+08
6.30E-06	1.760E+12	4.64E+11	2.933E+11	1.823E+12	1.073E+11	5.505E+11	7.411E+08
6.30E-06	1.629E+12	3.94E+11	2.859E+11	1.807E+12	1.083E+11	5.016E+11	7.109E+08
9.20E-06	1.629E+12	3.94E+11	2.859E+11	1.807E+12	1.083E+11	5.016E+11	7.109E+08
9.20E-06	1.634E+12	3.65E+11	2.719E+11	1.900E+12	1.047E+11	4.678E+11	4.271E+08
1.35E-05	1.634E+12	3.65E+11	2.719E+11	1.900E+12	1.047E+11	4.678E+11	4.271E+08

1.35E-05	1.573E+12	3.45E+11	2.484E+11	1.931E+12	1.030E+11	4.124E+11	5.566E+08
2.10E-05	1.573E+12	3.45E+11	2.484E+11	1.931E+12	1.030E+11	4.124E+11	5.566E+08
2.10E-05	2.366E+12	4.92E+11	3.598E+11	1.942E+12	1.058E+11	5.734E+11	5.780E+08
3.00E-05	2.366E+12	4.92E+11	3.598E+11	1.942E+12	1.058E+11	5.734E+11	5.780E+08
3.00E-05	1.506E+12	3.55E+11	2.700E+11	2.024E+12	1.093E+11	4.404E+11	3.960E+08
4.50E-05	1.506E+12	3.55E+11	2.700E+11	2.024E+12	1.093E+11	4.404E+11	3.960E+08
4.50E-05	1.687E+12	4.00E+11	2.874E+11	2.059E+12	1.072E+11	4.558E+11	4.745E+08
6.90E-05	1.687E+12	4.00E+11	2.874E+11	2.059E+12	1.072E+11	4.558E+11	4.745E+08
6.90E-05	1.989E+12	4.45E+11	3.516E+11	2.094E+12	1.072E+11	5.602E+11	7.632E+08
1.00E-04	1.989E+12	4.45E+11	3.516E+11	2.094E+12	1.072E+11	5.602E+11	7.632E+08
1.00E-04	1.934E+12	5.52E+11	3.928E+11	2.085E+12	1.067E+11	6.090E+11	4.969E+08
1.35E-04	1.934E+12	5.52E+11	3.928E+11	2.085E+12	1.067E+11	6.090E+11	4.969E+08
1.35E-04	2.248E+12	5.30E+11	4.196E+11	2.104E+12	1.029E+11	6.305E+11	3.303E+08
1.70E-04	2.248E+12	5.30E+11	4.196E+11	2.104E+12	1.029E+11	6.305E+11	3.303E+08
1.70E-04	1.853E+12	4.01E+11	2.812E+11	2.144E+12	1.079E+11	4.131E+11	3.635E+08
2.20E-04	1.853E+12	4.01E+11	2.812E+11	2.144E+12	1.079E+11	4.131E+11	3.635E+08
2.20E-04	2.160E+12	4.11E+11	3.383E+11	2.147E+12	1.141E+11	5.112E+11	6.225E+08
2.80E-04	2.160E+12	4.11E+11	3.383E+11	2.147E+12	1.141E+11	5.112E+11	6.225E+08
2.80E-04	1.862E+12	5.01E+11	2.904E+11	2.134E+12	1.068E+11	4.572E+11	2.520E+08
3.60E-04	1.862E+12	5.01E+11	2.904E+11	2.134E+12	1.068E+11	4.572E+11	2.520E+08
3.60E-04	2.030E+12	4.66E+11	3.402E+11	2.163E+12	1.078E+11	5.332E+11	3.186E+08
4.50E-04	2.030E+12	4.66E+11	3.402E+11	2.163E+12	1.078E+11	5.332E+11	3.186E+08
4.50E-04	1.565E+12	3.76E+11	2.784E+11	2.150E+12	1.109E+11	4.196E+11	2.485E+08
5.75E-04	1.565E+12	3.76E+11	2.784E+11	2.150E+12	1.109E+11	4.196E+11	2.485E+08
5.75E-04	1.888E+12	3.83E+11	2.775E+11	2.257E+12	1.095E+11	4.086E+11	2.049E+08
7.60E-04	1.888E+12	3.83E+11	2.775E+11	2.257E+12	1.095E+11	4.086E+11	2.049E+08
7.60E-04	2.085E+12	5.22E+11	3.685E+11	2.107E+12	1.094E+11	5.366E+11	3.234E+08
9.60E-04	2.085E+12	5.22E+11	3.685E+11	2.107E+12	1.094E+11	5.366E+11	3.234E+08
9.60E-04	1.703E+12	3.45E+11	2.710E+11	2.317E+12	1.131E+11	4.278E+11	2.100E+08
1.28E-03	1.703E+12	3.45E+11	2.710E+11	2.317E+12	1.131E+11	4.278E+11	2.100E+08
1.28E-03	2.771E+12	4.94E+11	4.140E+11	2.187E+12	1.213E+11	5.751E+11	2.256E+08
1.60E-03	2.771E+12	4.94E+11	4.140E+11	2.187E+12	1.213E+11	5.751E+11	2.256E+08
1.60E-03	2.203E+12	3.39E+11	3.276E+11	2.298E+12	1.213E+11	4.860E+11	1.386E+08
2.00E-03	2.203E+12	3.39E+11	3.276E+11	2.298E+12	1.213E+11	4.860E+11	1.386E+08
2.00E-03	1.515E+12	2.77E+11	2.427E+11	2.270E+12	1.173E+11	3.436E+11	2.229E+08
2.70E-03	1.515E+12	2.77E+11	2.427E+11	2.270E+12	1.173E+11	3.436E+11	2.229E+08
2.70E-03	2.687E+12	6.82E+11	4.274E+11	2.285E+12	1.178E+11	6.214E+11	4.470E+08
3.40E-03	2.687E+12	6.82E+11	4.274E+11	2.285E+12	1.178E+11	6.214E+11	4.470E+08
3.40E-03	1.663E+12	3.15E+11	2.690E+11	2.304E+12	1.150E+11	3.879E+11	2.090E+08
4.50E-03	1.663E+12	3.15E+11	2.690E+11	2.304E+12	1.150E+11	3.879E+11	2.090E+08

4.50E-03	3.108E+12	7.63E+11	4.495E+11	2.380E+12	1.202E+11	6.659E+11	3.160E+09
5.50E-03	3.108E+12	7.63E+11	4.495E+11	2.380E+12	1.202E+11	6.659E+11	3.160E+09
5.50E-03	1.775E+12	3.53E+11	2.589E+11	2.302E+12	1.191E+11	3.494E+11	1.449E+08
7.20E-03	1.775E+12	3.53E+11	2.589E+11	2.302E+12	1.191E+11	3.494E+11	1.449E+08
7.20E-03	2.263E+12	4.47E+11	3.592E+11	2.310E+12	1.242E+11	5.331E+11	1.599E+08
9.20E-03	2.263E+12	4.47E+11	3.592E+11	2.310E+12	1.242E+11	5.331E+11	1.599E+08
9.20E-03	2.171E+12	4.67E+11	3.180E+11	2.403E+12	1.348E+11	4.486E+11	2.181E+08
1.20E-02	2.171E+12	4.67E+11	3.180E+11	2.403E+12	1.348E+11	4.486E+11	2.181E+08
1.20E-02	2.732E+12	5.68E+11	3.983E+11	2.463E+12	1.315E+11	5.663E+11	2.916E+08
1.50E-02	2.732E+12	5.68E+11	3.983E+11	2.463E+12	1.315E+11	5.663E+11	2.916E+08
1.50E-02	1.969E+12	4.44E+11	3.188E+11	2.405E+12	1.365E+11	4.902E+11	2.006E+08
1.90E-02	1.969E+12	4.44E+11	3.188E+11	2.405E+12	1.365E+11	4.902E+11	2.006E+08
1.90E-02	1.544E+12	4.19E+11	2.797E+11	2.559E+12	1.540E+11	4.343E+11	2.492E+08
2.55E-02	1.544E+12	4.19E+11	2.797E+11	2.559E+12	1.540E+11	4.343E+11	2.492E+08
2.55E-02	3.216E+12	6.34E+11	4.821E+11	2.940E+12	2.268E+11	6.633E+11	1.893E+08
3.20E-02	3.216E+12	6.34E+11	4.821E+11	2.940E+12	2.268E+11	6.633E+11	1.893E+08
3.20E-02	3.337E+12	7.28E+11	4.545E+11	2.432E+12	9.188E+10	5.521E+11	2.574E+08
4.00E-02	3.337E+12	7.28E+11	4.545E+11	2.432E+12	9.188E+10	5.521E+11	2.574E+08
4.00E-02	2.202E+12	4.27E+11	2.868E+11	2.868E+12	1.548E+11	4.462E+11	1.991E+08
5.25E-02	2.202E+12	4.27E+11	2.868E+11	2.868E+12	1.548E+11	4.462E+11	1.991E+08
5.25E-02	3.097E+12	6.70E+11	5.311E+11	3.139E+12	1.960E+11	6.535E+11	1.633E+08
6.60E-02	3.097E+12	6.70E+11	5.311E+11	3.139E+12	1.960E+11	6.535E+11	1.633E+08
6.60E-02	2.327E+12	4.23E+11	3.328E+11	3.526E+12	2.235E+11	4.918E+11	2.338E+08
8.80E-02	2.327E+12	4.23E+11	3.328E+11	3.526E+12	2.235E+11	4.918E+11	2.338E+08
8.80E-02	4.698E+12	8.41E+11	6.210E+11	3.374E+12	1.591E+11	8.258E+11	7.596E+07
1.10E-01	4.698E+12	8.41E+11	6.210E+11	3.374E+12	1.591E+11	8.258E+11	7.596E+07
1.10E-01	3.622E+12	8.12E+11	5.390E+11	4.046E+12	2.489E+11	7.964E+11	3.763E+08
1.35E-01	3.622E+12	8.12E+11	5.390E+11	4.046E+12	2.489E+11	7.964E+11	3.763E+08
1.35E-01	5.041E+12	7.84E+11	7.139E+11	4.112E+12	1.647E+11	8.971E+11	6.207E+08
1.60E-01	5.041E+12	7.84E+11	7.139E+11	4.112E+12	1.647E+11	8.971E+11	6.207E+08
1.60E-01	3.500E+12	7.37E+11	5.728E+11	4.347E+12	1.947E+11	6.973E+11	5.378E+07
1.90E-01	3.500E+12	7.37E+11	5.728E+11	4.347E+12	1.947E+11	6.973E+11	5.378E+07
1.90E-01	4.084E+12	1.27E+12	7.448E+11	4.621E+12	2.387E+11	9.244E+11	2.433E+08
2.20E-01	4.084E+12	1.27E+12	7.448E+11	4.621E+12	2.387E+11	9.244E+11	2.433E+08
2.20E-01	5.114E+12	8.35E+11	6.182E+11	4.994E+12	2.498E+11	8.468E+11	1.293E+09
2.55E-01	5.114E+12	8.35E+11	6.182E+11	4.994E+12	2.498E+11	8.468E+11	1.293E+09
2.55E-01	7.325E+12	1.22E+12	8.097E+11	5.856E+12	2.791E+11	1.061E+12	1.056E+09
2.90E-01	7.325E+12	1.22E+12	8.097E+11	5.856E+12	2.791E+11	1.061E+12	1.056E+09
2.90E-01	7.857E+12	1.61E+12	1.014E+12	6.103E+12	2.405E+11	1.386E+12	1.576E+08
3.20E-01	7.857E+12	1.61E+12	1.014E+12	6.103E+12	2.405E+11	1.386E+12	1.576E+08

3.20E-01	5.243E+12	1.05E+12	6.222E+11	6.803E+12	3.146E+11	8.227E+11	9.962E+07
3.60E-01	5.243E+12	1.05E+12	6.222E+11	6.803E+12	3.146E+11	8.227E+11	9.962E+07
3.60E-01	7.387E+12	9.42E+11	1.007E+12	6.446E+12	2.703E+11	1.166E+12	1.520E+08
4.00E-01	7.387E+12	9.42E+11	1.007E+12	6.446E+12	2.703E+11	1.166E+12	1.520E+08
4.00E-01	6.528E+12	1.44E+12	7.684E+11	5.611E+12	2.842E+11	1.079E+12	3.570E+08
4.50E-01	6.528E+12	1.44E+12	7.684E+11	5.611E+12	2.842E+11	1.079E+12	3.570E+08
4.50E-01	6.521E+12	1.55E+12	9.414E+11	7.036E+12	3.286E+11	1.016E+12	1.296E+08
5.00E-01	6.521E+12	1.55E+12	9.414E+11	7.036E+12	3.286E+11	1.016E+12	1.296E+08
5.00E-01	6.577E+12	1.27E+12	1.081E+12	7.680E+12	3.327E+11	1.420E+12	1.564E+08
5.50E-01	6.577E+12	1.27E+12	1.081E+12	7.680E+12	3.327E+11	1.420E+12	1.564E+08
5.50E-01	9.053E+12	1.76E+12	1.196E+12	8.067E+12	3.450E+11	1.519E+12	1.566E+08
6.00E-01	9.053E+12	1.76E+12	1.196E+12	8.067E+12	3.450E+11	1.519E+12	1.566E+08
6.00E-01	6.880E+12	1.41E+12	1.016E+12	8.597E+12	3.109E+11	1.211E+12	1.199E+08
6.60E-01	6.880E+12	1.41E+12	1.016E+12	8.597E+12	3.109E+11	1.211E+12	1.199E+08
6.60E-01	9.522E+12	1.74E+12	1.208E+12	8.808E+12	3.705E+11	1.688E+12	1.410E+10
7.20E-01	9.522E+12	1.74E+12	1.208E+12	8.808E+12	3.705E+11	1.688E+12	1.410E+10
7.20E-01	1.011E+13	2.42E+12	1.413E+12	1.006E+13	3.332E+11	1.717E+12	2.453E+08
7.80E-01	1.011E+13	2.42E+12	1.413E+12	1.006E+13	3.332E+11	1.717E+12	2.453E+08
7.80E-01	1.089E+13	1.53E+12	1.498E+12	1.037E+13	3.429E+11	1.798E+12	1.050E+09
8.40E-01	1.089E+13	1.53E+12	1.498E+12	1.037E+13	3.429E+11	1.798E+12	1.050E+09
8.40E-01	9.161E+12	1.58E+12	1.079E+12	1.020E+13	3.395E+11	1.384E+12	2.574E+08
9.20E-01	9.161E+12	1.58E+12	1.079E+12	1.020E+13	3.395E+11	1.384E+12	2.574E+08
9.20E-01	1.143E+13	1.48E+12	1.464E+12	8.942E+12	2.955E+11	1.850E+12	1.130E+08
1.00E+00	1.143E+13	1.48E+12	1.464E+12	8.942E+12	2.955E+11	1.850E+12	1.130E+08
1.00E+00	4.000E+12	7.38E+11	5.258E+11	9.968E+12	3.193E+11	6.575E+11	5.896E+07
1.20E+00	4.000E+12	7.38E+11	5.258E+11	9.968E+12	3.193E+11	6.575E+11	5.896E+07
1.20E+00	1.097E+13	2.32E+12	1.515E+12	1.039E+13	3.302E+11	1.806E+12	2.171E+08
1.40E+00	1.097E+13	2.32E+12	1.515E+12	1.039E+13	3.302E+11	1.806E+12	2.171E+08
1.40E+00	1.237E+13	2.68E+12	1.567E+12	1.073E+13	3.153E+11	2.013E+12	1.348E+08
1.60E+00	1.237E+13	2.68E+12	1.567E+12	1.073E+13	3.153E+11	2.013E+12	1.348E+08
1.60E+00	1.259E+13	2.15E+12	1.802E+12	1.067E+13	3.014E+11	1.925E+12	4.539E+08
1.80E+00	1.259E+13	2.15E+12	1.802E+12	1.067E+13	3.014E+11	1.925E+12	4.539E+08
1.80E+00	1.003E+13	2.33E+12	1.643E+12	1.029E+13	3.102E+11	2.192E+12	2.090E+08
2.00E+00	1.003E+13	2.33E+12	1.643E+12	1.029E+13	3.102E+11	2.192E+12	2.090E+08
2.00E+00	6.708E+12	1.62E+12	1.061E+12	9.972E+12	2.451E+11	1.323E+12	1.006E+08
2.30E+00	6.708E+12	1.62E+12	1.061E+12	9.972E+12	2.451E+11	1.323E+12	1.006E+08
2.30E+00	1.098E+13	2.25E+12	1.544E+12	9.767E+12	2.616E+11	2.218E+12	1.944E+08
2.60E+00	1.098E+13	2.25E+12	1.544E+12	9.767E+12	2.616E+11	2.218E+12	1.944E+08
2.60E+00	9.350E+12	1.89E+12	1.439E+12	8.750E+12	2.022E+11	2.076E+12	1.034E+08
2.90E+00	9.350E+12	1.89E+12	1.439E+12	8.750E+12	2.022E+11	2.076E+12	1.034E+08

2.90E+00	7.049E+12	1.65E+12	1.031E+12	7.790E+12	1.691E+11	1.317E+12	1.581E+09
3.30E+00	7.049E+12	1.65E+12	1.031E+12	7.790E+12	1.691E+11	1.317E+12	1.581E+09
3.30E+00	8.022E+12	1.51E+12	1.181E+12	6.380E+12	1.088E+11	1.541E+12	6.160E+07
3.70E+00	8.022E+12	1.51E+12	1.181E+12	6.380E+12	1.088E+11	1.541E+12	6.160E+07
3.70E+00	6.505E+12	1.73E+12	9.506E+11	5.539E+12	1.175E+11	1.227E+12	4.173E+07
4.10E+00	6.505E+12	1.73E+12	9.506E+11	5.539E+12	1.175E+11	1.227E+12	4.173E+07
4.10E+00	5.599E+12	1.18E+12	8.901E+11	4.920E+12	1.118E+11	1.092E+12	1.402E+08
4.50E+00	5.599E+12	1.18E+12	8.901E+11	4.920E+12	1.118E+11	1.092E+12	1.402E+08
4.50E+00	4.241E+12	7.56E+11	5.064E+11	3.999E+12	9.422E+10	7.740E+11	7.904E+07
5.00E+00	4.241E+12	7.56E+11	5.064E+11	3.999E+12	9.422E+10	7.740E+11	7.904E+07
5.00E+00	4.133E+12	1.20E+12	6.310E+11	3.067E+12	7.264E+10	7.652E+11	1.346E+08
5.50E+00	4.133E+12	1.20E+12	6.310E+11	3.067E+12	7.264E+10	7.652E+11	1.346E+08
5.50E+00	3.726E+12	5.51E+11	4.853E+11	2.447E+12	6.565E+10	5.620E+11	1.394E+08
6.00E+00	3.726E+12	5.51E+11	4.853E+11	2.447E+12	6.565E+10	5.620E+11	1.394E+08
6.00E+00	1.609E+12	2.82E+11	2.667E+11	1.957E+12	3.713E+10	3.615E+11	2.322E+08
6.70E+00	1.609E+12	2.82E+11	2.667E+11	1.957E+12	3.713E+10	3.615E+11	2.322E+08
6.70E+00	2.047E+12	2.78E+11	3.042E+11	1.188E+12	3.533E+10	3.654E+11	2.095E+08
7.40E+00	2.047E+12	2.78E+11	3.042E+11	1.188E+12	3.533E+10	3.654E+11	2.095E+08
7.40E+00	9.898E+11	2.09E+11	1.716E+11	7.333E+11	1.453E+10	2.587E+11	2.711E+08
8.20E+00	9.898E+11	2.09E+11	1.716E+11	7.333E+11	1.453E+10	2.587E+11	2.711E+08
8.20E+00	4.670E+11	1.63E+11	1.107E+11	4.302E+11	1.399E+10	1.533E+11	2.451E+06
9.00E+00	4.670E+11	1.63E+11	1.107E+11	4.302E+11	1.399E+10	1.533E+11	2.451E+06
9.00E+00	2.759E+11	6.03E+10	6.184E+10	3.496E+11	7.170E+09	7.940E+10	1.723E+07
1.00E+01	2.759E+11	6.03E+10	6.184E+10	3.496E+11	7.170E+09	7.940E+10	1.723E+07
1.00E+01	3.402E+11	5.62E+09	5.712E+10	1.847E+11	5.842E+09	6.078E+10	5.418E+06
1.10E+01	3.402E+11	5.62E+09	5.712E+10	1.847E+11	5.842E+09	6.078E+10	5.418E+06
1.10E+01	2.183E+11	5.96E+10	1.990E+10	1.209E+11	0	0	5.612E+06
1.20E+01	2.183E+11	5.96E+10	1.990E+10	1.209E+11	0	0	5.612E+06
1.20E+01	0	0	1.030E+10	2.654E+10	2.038E+08	0	7.175E+05
1.30E+01	0	0	1.030E+10	2.654E+10	2.038E+08	0	7.175E+05
1.30E+01	1.111E+11	0	3.496E+09	3.788E+10	1.071E+09	0	1.110E+05
1.40E+01	1.111E+11	0	3.496E+09	3.788E+10	1.071E+09	0	1.110E+05
1.40E+01	6.960E+10	0	1.058E+10	1.207E+10	0	0	2.596E+05
1.50E+01	6.960E+10	0	1.058E+10	1.207E+10	0	0	2.596E+05
1.50E+01	0	0	0	0	0	0	2.046E+05
1.60E+01	0	0	0	0	0	0	2.046E+05
1.60E+01	0	0	0	0	0	0	4.488E+03
1.70E+01	0	0	0	0	0	0	4.488E+03